ZnO and MgZnO Nanostructures and Heterostructures

by

Muhammad Zakria

A thesis submitted in partial fulfilment of the requirements for the degree of
Doctor of Philosophy

in the

School of Mathematical & Physical Sciences
Faculty of Science

February 2021

Certificate of Original Authorship

I, Muhammad Zakria declare that this thesis with title "ZnO and MgZnO Nanostructures and Heterostructures" is submitted in the fulfilment of the requirement for the award of Doctor of Philosophy (PhD), in the School of Mathematical and Physical Sciences, Faculty of Science, at the University of Technology Sydney.

This thesis is wholly my own work unless otherwise reference or acknowledged. In addition, I certify that all information sources and literature used are indicated in the thesis. This document has not been submitted for qualifications at any other academic institution.

This research is supported by an Australian Government Research Training Programme.

Production Note:

Student Signature: Signature removed prior to publication.

Date: 19/02/2021

Acknowledgments

First, I would like to express my sincere thanks to my supervisor, Assoc. Prof. Cuong Ton-That for his support and encouragement during my PhD journey at UTS. His fruitful advice helped me in producing quality research, laboratory work, articles preparation and thesis writing. I would also like to express special gratefulness to my co-supervisor, Prof. Matthew R. Phillips for his valuable guidance and feedback on my work, especially during my presentations.

I would also like to thank Dr. David Rogers from Nanovation, France for his technical discussion, sample preparation and XRD characterisation. Additionally, I acknowledge the technical support of Dr. Bruce Cowie at the Australian Synchrotron, Melbourne for the NEXAFS measurements.

I extend my gratitude to Assoc. Prof. Dr F. C. Chung Ling in the Department of Physics, The University of Hong Kong for the fabrication of MQWs samples and the TEM and EDX analysis.

Here, I must acknowledge and thanks to Dr. Mandeep Singh and Prof. Vipul Bansal from RMIT University Melbourne for ZnO nanosheet preparation, along with XRD, Raman spectroscopy and photoluminescence characterisation.

I would like to thank the staff of Microstructural Analysis Unit (MAU), particularly to the lab manager Katie McBean, Geoff McCredie, Herbert Yuan, Mark Lockrey. I appreciate the technical help of Saskia Fiedler, Md. Azizar Rahman and Olivier Lee for their valuable tips and suggestions on the use of the CL and PL techniques.

I would like to acknowledge and thank the financial support from the UTS for my PhD study in Australia.

Finally, I would like to show my special thanks to my beloved family and parents for their moral support and sustaining inspiration. My dissertation and research work would never be possible without their love and affection.

Publications and Presentation

1. **M. Zakria**, T. T. Huynh, F. C. C. Ling, S. C. Su, M. R. Phillips, C. Ton-That. “Highly Luminescent MgZnO/ZnO Multiple Quantum Wells for Photonics Devices” ACS Applied Nano Materials, (2019), 2, 2574 – 2579.
2. **M. Zakria,** P. Bove, D. J. Rogers, F. H. Teherani, E. V. Sandana, M. R. Phillips, and C. Ton-That. “Chemical Structure and Optical Signatures of Nitrogen Acceptors in MgZnO” J. Mater. Chem. C, (2020),8, 6435-6441.
3. **M. Zakria**, Matthew Phillips, Cuong Ton-That. “Luminescence Enhancement of MgZnO/ZnO Multiple Quantum Wells by Hydrogen Plasma Treatment” ICONN 2020.
4. T. T. Huynh, Chikoidze, E., Curtis P. Irvine, **Muhammad Zakria**, Dumont, Y., Teherani, F.H., Sandana, V.E., Bove, P., Rogers, D.J., MR Phillips, C Ton-That “Red Luminescence in H-doped β-Ga2O3” Phys. Rev. Materials 4, 085201 (2020).

Table of Contents

Certificate of Original Authorship ii

Acknowledgments iii

Publications and Presentation v

Table of Contents vi

List of Figures ix

List of Tables xiii

List of Abbreviations xiv

Abstract xvi

1. Overview of the Research Project 18
   - 1.1. Background and Motivation 18
   - 1.2. Aims of the Project 20
   - 1.3. Thesis Layout 21

2. ZnO-based Materials and Heterostructures: Current Status and Potential 23
   - 2.1. ZnO Properties and Applications 24
   - 2.2. Optical Properties of ZnO 27
     - 2.2.1. Defects in ZnO 28
     - 2.2.2. Hydrogen in ZnO 33
   - 2.3. Acceptors in ZnO and MgZnO 36
   - 2.4. Band Gap Engineering of ZnO 39
     - 2.4.1. Mg-doped ZnO Alloy 40
   - 2.5. MgZnO/ZnO Heterostructures 42
     - 2.5.1. Two-Dimensional Electron Gas 43
   - 2.6. Two-dimensional (2D) Materials 46
     - 2.6.1. ZnO Nanostructures and 2D Nanosheets 48

3. Experimental Techniques 52
   - 3.1. Characterisation Techniques 52
     - 3.1.1. Atomic Force Microscopy 53
     - 3.1.2. Near-edge X-ray Absorption Fine Structure Spectroscopy 55

3.1.3. Scanning Electron Microscopy 57
3.1.4. Cathodoluminescence Spectroscopy 58
3.1.4.1. Cathodoluminescence Spectrum Correction and Calibration 61
3.1.4.2. CASINO Simulation of Electron Energy Loss in MgZnO/ZnO MQWs 64
3.1.5. Photoluminescence Spectroscopy 67
3.1.6. Depth-resolved CL 68
3.1.7. Temperature-resolved CL and PL 68
3.1.8. Power-dependent CL and PL 69
3.2. Synthesis and Fabrication of the Samples in this Thesis 70
4. Hydrogenation of MgZnO/ZnO Multiple Quantum Wells 73
4.1. Introduction 73
4.2. Morphological Properties 76
4.3. Cathodoluminescence Properties 79
4.3.1. Enhancement of MQWs Emission by Hydrogen Incorporation 79
4.3.2. Thermal Stability of RRPA MQWs Emission 84
4.3.3. Temperature- and Excitation-dependent CL 87
4.3.4. Depth-dependent CL Analysis 93
4.4. Conclusions 96
5. Nitrogen Acceptors in MgZnO 97
5.1. Introduction 97
5.2. Structural and Morphological Properties 100
5.3. Near-edge X-ray Absorption Fine Structure 102
5.4. Optical Band Gap Analysis 105
5.5. Photoluminescence Spectroscopy 107
5.5.1. Donor–acceptor-pair Emission 107
5.5.2. Temperature-dependent Photoluminescence 109
5.5.3. Excitation Power-dependent Photoluminescence 113
5.6. Conclusions 117
6. Two-dimensional ZnO Nanosheets 118
6.1. Introduction 118
6.2. Structural and Morphological Properties 120
6.2.1. Structural Properties 120
6.2.2. Morphological Properties 124
6.3. Optical Properties 129

6.3.1. Photoluminescence Spectroscopy Analysis 132
6.3.2. Cathodoluminescence Analysis of Single ZnO Nanosheet 133
6.3.2.1. Temperature-resolved Cathodoluminescence 139
6.4. Conclusions 142
7. Conclusions and Future Work 143
7.1. Conclusions 143
7.2. Future Work 145
References 147

List of Figures

Fig. 2.1: Historical view of research and applications for ZnO....................................25

Fig. 2.2: High-resolution PL spectrum of bulk ZnO..30

Fig. 2.3: Schematic representation of transition energy levels in ZnO 32

Fig. 2.4: Formation energy of intrinsic defects versus Fermi energy level 32

Fig. 2.5: Possible bonding configurations of H in a ZnO crystal structure 35

Fig. 2.6: PL results for as-grown and H-doped ZnO 36

Fig. 2.7: Schematic view of various acceptor energy levels in ZnO. 38

Fig. 2.8: Bandgap energy versus Mg mole fraction for an MgZnO alloy. 41

Fig. 2.9: Bandgap energy versus lattice parameter for (Al,In)GaN and (Mg,Cd)ZnO alloying. 41

Fig. 2.10: Schematic view of a LED heterostructure made of ZnO and N-doped MgZnO layer acting as a p–n bipolar junction 43

Fig. 2.11: MgZnO/ZnO heterostructure band diagram and its heterointerface H-band radiative recombination. 44

Fig. 2.12: A historical (2007–16) representation of mobility (μ) versus carrier concentration (n) for a MgZnO/ZnO 2DEG system. 46

Fig. 2.13: Highly explored materials of the 2D nanostructures....................................48

Fig. 2.14: Electron microscopy images of ZnO nanostructures. 51

Fig. 2.15: AFM image and PL spectra of different ZnO nanosheets.............................51

Fig. 3.1: Diagrammatical view of AFM system 54

Fig. 3.2: Park XE7 AFM system at UTS. 55

Fig. 3.3: Diagram for the basic principles of NEXAFS 56

Fig. 3.4: A schematic representation of the NEXAFS system using a soft X-ray source at the Australian Synchrotron, Melbourne. 57

Fig. 3.5: Schematic representation of incident electron beam with sample 58

Fig. 3.6: Schematic representation of different transition pathways 59

Fig. 3.7: CL spectroscopic system in a schematic form 61

Fig. 3.8: Method for conversion of pixel positions to wavelength scale. 63

Fig. 3.9: CASINO simulation of electron beam interaction in MgZnO/ZnO MQWs structure. 66

Fig. 4.1: TEM cross-sectional image of a MgZnO/ZnO MQWs. 77

Fig. 4.2: Energy-dispersive X-ray mapping of Mg, Al and Zn elements in a pristine MgZnO/ZnO MQWs. 77

Fig. 4.3: AFM images pristine MQWs and H-doped MQWs. 78

Fig. 4.4: Fitted CL spectra of pristine and H-doped MQWs. 81

Fig. 4.5: CL spectra of pristine and RRPA treated MgZnO/ZnO MQWs along with their enhancement factor. 82

Fig. 4.6: Thermal stability of RRPA-treated MQWs CL emission 85

Fig. 4.7: Power-resolved CL for pristine and RRPA MQWs. 86

Fig. 4.8: Log-log plots based on the power-law model. 87

Fig. 4.9: Temperature-resolved CL spectra along with Arrhenius plots. 91

Fig. 4.10: FWHM of the MQW emission as a function of temperature for pristine and RRPA-treated MQWs. 92

Fig. 4.11: CASINO-simulated electron energy loss profiles for the MQWs. 94

Fig. 4.12: Depth-resolved CL spectra of pristine MQWs and the enhancement factor as a function of acceleration voltage. 95

Fig. 5.1: AFM and SEM images of PLD based MgZnO:N, MgZnO:O and MgZnO:vac epilayers. 101

Fig. 5.2: NEXAFS spectra for MgZnO:N and MgZnO:O epilayers. 104

Fig. 5.3: Optical transmission spectra for three different MgZnO epilayers. 107

Fig. 5.4: PL spectra of the MgZnO/ZnO bilayers and the ZnO underlayer. 109

Fig. 5.5: Temperature-resolved PL spectra for the MgZnO:N sample. 111

Fig. 5.6: Peak and activation energies for the ZnO FX and MgZnO N-related DAP emissions in MgZnO:N epilayer. 112

Fig. 5.7: Power-resolved PL spectra of the MgZnO:N epilayer. 115

Fig. 5.8: DAP peak position versus excitation poser and log-log plot of the ZnO FX and MgZnO:N DAP emission. 116

Fig. 6.1: Schematic representation of atomic arrangements of Zn and O in a single monolayer ZnO 121

Fig. 6.2: XRD spectra and Raman spectra of ZnO nanosheets and microparticles...... 123

Fig. 6.3: SEM and TEM image of the parent faceted ZnO microparticles and ZnO 2D nanosheets. 125

Fig. 6.4: EDX spectrum and elemental maps of a ZnO nanosheet. 126

Fig. 6.5: TEM and AFM micro-images of a ZnO single nanosheet prepared from three different suspensions at centrifugation speeds of 500, 5,000 and 18,000 g. 128

Fig. 6.6: AFM images, extinction, absorption, scattering coefficient, and PL results for ZnO nanosheets at three different centrifugation (g)...131

Fig. 6.7: AFM images of a single thin nanosheet along with their thickness profile. ..134

Fig. 6.8: CL spectra acquired from individual exfoliated nanosheet and parent ZnO microparticle 135

Fig. 6.9: Fitted spectra of experimental CL data points with a Gaussian function for three nanosheets. 137

Fig. 6.10: FX photon energy and Huang–Rhys phonon coupling factor S as a function of nanosheet thickness. 138

Fig. 6.11: Temperature-resolved CL of ZnO exfoliated 2D nanosheets and their activation energy analysis. 141

Fig. 7.1: CL spectral results of three different bilayer homoepitaxial samples (MgZnO /ZnO /(A, B, and C) -plane ZnO substrate..146

List of Tables

Table 2.1: Comparative properties of ZnO and GaN 26

Table 2.2: ZnO free and bound exciton recombination lines. 28

Table 2.3: Deep-level defects and their corresponding features 33

Table 3.1: NIST atomic spectra database used for pixel conversion 63

Table 3.2: Summary of samples information. 72

Table 4.1: Summary of post-treated MQWs samples. 76

Table 4.2: All values of integral, peak intensity of pristine and RRPA-treated samples and their corresponding enhancement factor. 83

Table 5.1: Values for three MgZnO film thicknesses with their corresponding ambient conditions on ZnO buffer layer 100

Table 5.2: Lattice parameter, FWHM, RMS surface roughness and electrical resistivity (ρ) for the ZnO underlayer and MgZnO/ZnO bilayers. 102

Table 5.3: Peak position and their corresponding chemical signature, and relative intensity in percentage for each peak in the NEXAFS measurements. 105

Table 6.1: ZnO 2D exfoliated nanosheets with corresponding thickness ranges......... 132

List of Abbreviations

Abbreviation	Definition
AEs	Auger electrons
AFM	Atomic force microscopy
$A^{o}X$	Neutral acceptor bound exciton
BSE	Back scattered electrons
BSF	Basal stacking fault
CCD	Charge-coupled device
CL	Cathodoluminescence
DAP	Donor–acceptor pair
$D^{o}X$	Neutral donor-bound exciton
DX	Donor-bound exciton
EDX	Energy-dispersive X-ray
FX	Free exciton
FWHM	Full width at half maximum
GL	Green luminescence
h-BN	Hexagonal boron nitride
HEMT	High electron mobility transistor
LED	Light-emitting diode
LO	Longitudinal optical
MBE	Molecular beam epitaxy
MQW	Multiple quantum well
NBE	Near band edge
NEXAFS	Near-edge X-ray absorption fine structure
NIST	National Institute of Standard and Technology
PL	Photoluminescence
PLD	Pulsed laser deposition
RRPA	Rapid remote plasma annealing
RMS	Root mean square

RRS	Resonant Raman scattering
SE	Secondary electron
SEM	Scanning electron microscope
TEM	Transmission electron microscope
TEY	Total electron yield
TFY	Total fluorescence yield
TMD	Transition metal dichalcogenide
UV	Ultraviolet
VBM	Valence band maximum
XRD	X-ray diffraction

Abstract

ZnO-based heterostructures and nanostructures have attracted significant interest owing to their wide range of technological applications. The recent achievement of high electron mobility at the MgZnO/ZnO heterointerface has sparked great interest in a multitude of research fields. In order to exploit the extraordinary electron states at the MgZnO/ZnO interface, high quality films with bespoke optical and electronic properties must be achieved. Although the ZnO-based heterostructures have been widely explored for various applications, where the performance is often hindered by intrinsic and extrinsic defects. This work aims to elucidate the physics of defects and the properties of ZnO-based thin films, interfaces and 2D nanosheets.

Oxide-based multiple quantum wells (MQWs) were investigated using cathodoluminescence (CL) and high-resolution electron microscopy techniques. A rapid remote plasma annealing (RRPA) method was used to treat MgZnO/ZnO MQWs in order to modify their defect structure. Following the RRPA in hydrogen, the MQW optical emission increased by more than 10 times after a 40 seconds treatment, while the basal stacking faults (BSFs) and point defects emissions were completely quenched. Furthermore, the RRPA-treated MQWs were found to be highly stable up to a temperature of 400°C.

A major challenge in the development of ZnO-based devices is the lack of reliable p-type material. In this work, chemical and optical signatures of nitrogen in N-doped MgZnO were investigated using near-edge X-ray absorption fine structure (NEXAFS) and photoluminescence (PL). The MgZnO epilayer, grown under nitrogen ambient, exhibits higher resistivity compared with epilayers grown under oxygen or vacuum

atmospheres, and displays a dominant donor-acceptor-pair (DAP) peak located at 160 meV below its exciton emission. NEXAFS reveals that nitrogen in the N-doped MgZnO exists in multiple chemical states with molecular N_2 and substitutional N on O sites (N_O) being the dominant species. The PL emission peak at 3.45 eV in the N-doped MgZnO is attributed to a shallow donor to a deep acceptor recombination, where the compensating acceptor is most likely molecular N_2.

The last part of this thesis reports the luminescence and morphological properties of ZnO 2D nanosheets, fabricated by chemical exfoliation of ZnO microparticles. High-spatial-resolution CL was employed to acquire the optical properties of individual nanosheets. Combined CL and PL analysis shows strong thickness-dependent quantum confinement of excitons in few-atomic-layer thin nanosheets, which leads to substantial variations in the excitonic and phonon coupling properties. The superior excitonic properties of ZnO nanosheets could potentially lead to the development of efficient nano-optoelectronic devices.

Chapter 1

1. Overview of the Research Project

1.1. Background and Motivation

ZnO is a remarkable wide-band-gap semiconductor that offers a plethora of exciting applications in photonics and electronics. In the last two decades, ZnO-based semiconductors have been explored as an alternative and a strong competitor to GaN-based counterparts. Some exceptional advantages of ZnO over other semiconductors are briefly discussed here. ZnO is highly efficient light emitter at room temperature and above because it has a large exciton binding energy (~60 meV), which is much greater than that of GaN (~24 meV). ZnO has the highest recorded exciton binding energy among binary oxide materials. A ZnO-based technology is easily scalable and cost-effective because of the availability of native substrates for homo-epitaxial growth. ZnO is inexpensive, being naturally abundant and non-hazardous, thus manufacturing costs for ZnO-based devices could be far lower than those of GaN.[1] Finally, ZnO-based device fabrication can be easily processed using wet chemical etching techniques, unlike GaN-based devices.[2]

Despite these attractive properties, ZnO remains underexploited in bipolar junction device applications because of fundamental problems including intrinsic defects (acceptor killers) and a lack of reproducible and reliable p-type ZnO. To overcome these critical issues, MgZnO have recently been used for the fabrication of p-n MgZnO/ZnO heterojunctions and proved a most promising possible material for LEDs (light-emitting diode) devices.[3] The most common doping element for producing acceptors in ZnO is nitrogen (N), but this approach is limited by the low solubility of N. Interestingly, N

solubility is increased by replacing Zn with isovalent Mg.[4, 5] As a ternary alloy semiconductor, MgZnO has almost identical lattice constants to those of ZnO but a wider bandgap.[6] By changing the Mg concentration, the bandgap of a MgZnO alloy can be tuned in the range 3.3–4.2 eV,[6] which has been exploited for fabricating tuneable optical emitters.[7] These properties make MgZnO an ideal interface material for the fabrication of ZnO-based superlattices and heterostructures such as multiple quantum wells (MQWs) and p–n heterojunctions. Recent advances in atomistic modelling and synthesis of oxide heterostructures have provided fertile new ground for creating extraordinary states at oxide interfaces.[8, 9] In addition to providing a solution to p-type ZnO, the interface formed between ZnO and MgZnO possesses unique physical properties that arise from the strongly correlated d electrons.[10] The interplay among charge, degrees of freedom and spin produces symmetry breaking in MgZnO/ZnO heterostructures, leading to a wealth of emergent phenomena such as ferromagnetism, superconductivity and giant thermoelectric effects.[8, 11]

Another critical issue with ZnO-based heterostructures is the presence of defects, which degrade the optical and electrical properties. Hydrogen (H) is a shallow donor and can be easily incorporated into ZnO-based heterostructures, which can increases near-band-edge (NBE) emission intensity and decreases unwanted defect-related emission.[12] Further, because of the mismatch in spontaneous and piezoelectric polarisation of ZnO and MgZnO, electrons with extremely high mobility accumulate at the interface,[13] producing a layer of two-dimensional electron gas (2DEG). This 2DEG phenomenon has become a new frontier in electronic materials, where high-mobility electrons interact and are ordered in a unique way. Such oxide interfaces offer tremendous possibilities in designing a new generation of electronic and sensing devices that can operate at ultra-high frequencies.

Apart from ZnO thin films, nanomaterials and heterostructures, ultrathin ZnO 2D nanosheets open a new era in the world of 2D materials. Various 2D materials with small band gap (MoS_2, $MoSe_2$, WS_2 and InSe) [14, 15] and large band gap (hexagonal boron nitride [h-BN], ZnO and Ga_2O_3) [16, 17] have been recently reported. In anisotropic materials, the weak inter-layer interaction and strong in-plane bonding in ZnO make it easy and viable to fabricate ZnO 2D nanosheets.[14, 18] 2D materials offer unique characteristics such as exciton confinement and can be combined with other 2D nanolayer materials to form a 2D nano–heterostructures. These 2D nano–heterostructures offer tremendous new opportunities for 2D nano-electronics and nano-optoelectronics applications. The high specific surface area of 2D nanosheets also makes it highly suitable for applications in super-capacitors and catalysts.[19] In this project, ZnO nanosheets are shown to possess superb optical properties compared with their bulk counterpart.

1.2. Aims of the Project

The overall aim of the project is to fully elucidate the physics and chemistry of ZnO and MgZnO heterostructures and nanostructures. In particular, the specific goals are:

- ❖ To conduct materials development and characterisation studies of oxide multiple quantum wells (MQWs) and 2D nanomaterials.
- ❖ To investigate the effects of defects on the optical properties of MgZnO/ZnO MQWs by evaluating the use of remote plasma post-treatment to alter their defect structure.
- ❖ To understand the physics of low temperature MgZnO growth that allows the incorporation of nitrogen into MgZnO thin films at a high concentration as well as the chemical and optical signatures of nitrogen acceptors in MgZnO.

- ❖ To investigate the physical processes governing the optical and electronic structure of ZnO 2D nanosheets that are fabricated by a liquid exfoliation method.

1.3. Thesis Layout

The thesis includes seven chapters as follows.

Chapter 1: Overview of the research project

This chapter provides an overview of the PhD project, which involves ZnO- and MgZnO-based heterostructures and nanostructures. The background, motivation and objective of the project are briefly discussed.

Chapter 2: ZnO-based materials and heterostructures: current status and potential

In this chapter, a thorough and up-to-date review of intrinsic and extrinsic defects, impurities, doping in ZnO, heterostructures and nanostructures, their basic properties, applications and challenges are provided. The emphasis of this chapter is on luminescence centers and their characteristics in ZnO- and MgZnO-related materials.

Chapter 3: Experimental techniques

Chapter 3 provides detailed description of the experimental techniques used in this project.

Chapter 4: Hydrogenation of MgZnO/ZnO multiple quantum wells

Chapter 4 reports on the effects of hydrogenation on the optical properties of MgZnO/ZnO MQWs.

Chapter 5: Nitrogen acceptors in MgZnO

This chapter describes a detailed investigation of the optical signatures of N acceptors in MgZnO epilayer, along with its chemical identification.

Chapter 6: Two-dimensional ZnO nanosheets

In this chapter, the structural properties and exciton quantum confinement in ultrathin stable ZnO 2D nanosheets are reported. These nanosheets are fabricated by the soft-chemical exfoliation method.

Chapter 7: Conclusions and future work

The last chapter of the thesis contains a summary of key findings in the project and suggestion for future work.

.

Chapter 2

2. ZnO-based Materials and Heterostructures: Current Status and Potential

ZnO-based materials offer tremendous opportunities for potential applications in the field of photonics, spintronic and optoelectronics. The astonishing optical, electrical and magnetic characteristics of ZnO-based materials and their interfaces further open the doors for emerging research in areas such as the quantum Hall effect, strong electron–electron correlation effect and the 2DEG at the interface. MgZnO is an ideal ZnO-based alloy material for the development of ZnO-based heterostructures and p-type doping for optoelectronic applications. Among the various ZnO-based heterostructure materials systems, MgZnO/ZnO MQWs are of potential interest because fine-tuning of their optical emission can be achieved by adjusting their structural parameters. Various defects that limit the optical emission of MgZnO/ZnO MQWs could be passivated and controlled by H incorporation, which further enhances the optical emission. Furthermore, the important pathway to producing acceptors or holes in ZnO-based materials that leads to p-type conductivity is the doping approach. Among various dopants, nitrogen has become an attractive candidate material for producing acceptor concentration in ZnO and MgZnO. This chapter presents a detailed review of ZnO- and MgZnO-based materials, their heterostructures and nanostructures, that can make a significant contribution to optoelectronics applications. The chapter also focuses on a review of exciton confinement

in ZnO 2D nanostructures, which can offer a roadmap for nano-optoelectronics applications.

2.1. ZnO Properties and Applications

Among all semiconductors, ZnO is the most demanding, highly explored and globally research-oriented binary II-VI semiconductor. ZnO is widely used in optoelectronics, acoustics, and sensing-based applications. ZnO has been investigated as an alternative to GaN-based counterparts for optoelectronic applications.[20-22] ZnO is a strong competitor for GaN and each has its own merits and drawbacks. GaN-based device fabrication is mature technology, but ZnO requires further investigation to overcome the main challenge of a reliable and stable p-type material. The comparative properties of ZnO and GaN are summarized in table 2.1.[2, 23] Other important applications of ZnO are nanogenerators and transparent conducting oxide (TCO) electronics.[24, 25] The main remarkable features of ZnO are its high exciton binding energy (60 meV) at room temperature, wide direct bandgap and high piezoelectric and spontaneous polarisation; and the fact that it is non-toxic, highly pure and cost-effective.[26-28] The wide optical bandgap of 3.37 eV and 3.44 eV at room and low temperature, respectively, make it suitable for ultraviolet (UV) and blue wavelength range applications.[22] Besides the existing and explored characteristics of ZnO, its nanostructures further offer innovative and attractive features owing to their high surface-to-volume ratio. According to the literature, ZnO offers a wide range of nanostructures including nanowires, nanoparticles, nanobelts, nanotubes, nanonails and spiral nanoring structures. These flexible and wide-ranging structures and sizes make ZnO more viable for nanotechnology applications.[29-32] Fundamentally, ZnO has a non-inversion symmetrical wurtzite crystal structure with two polar surfaces of Zn and O. A hexagonal

wurtzite structure is more stable and common than a zinc blend structure under ambient conditions.[33, 34] A summary of the history of ZnO-based materials research, characteristics and their innovative applications is provided in figure 2.1.[28]

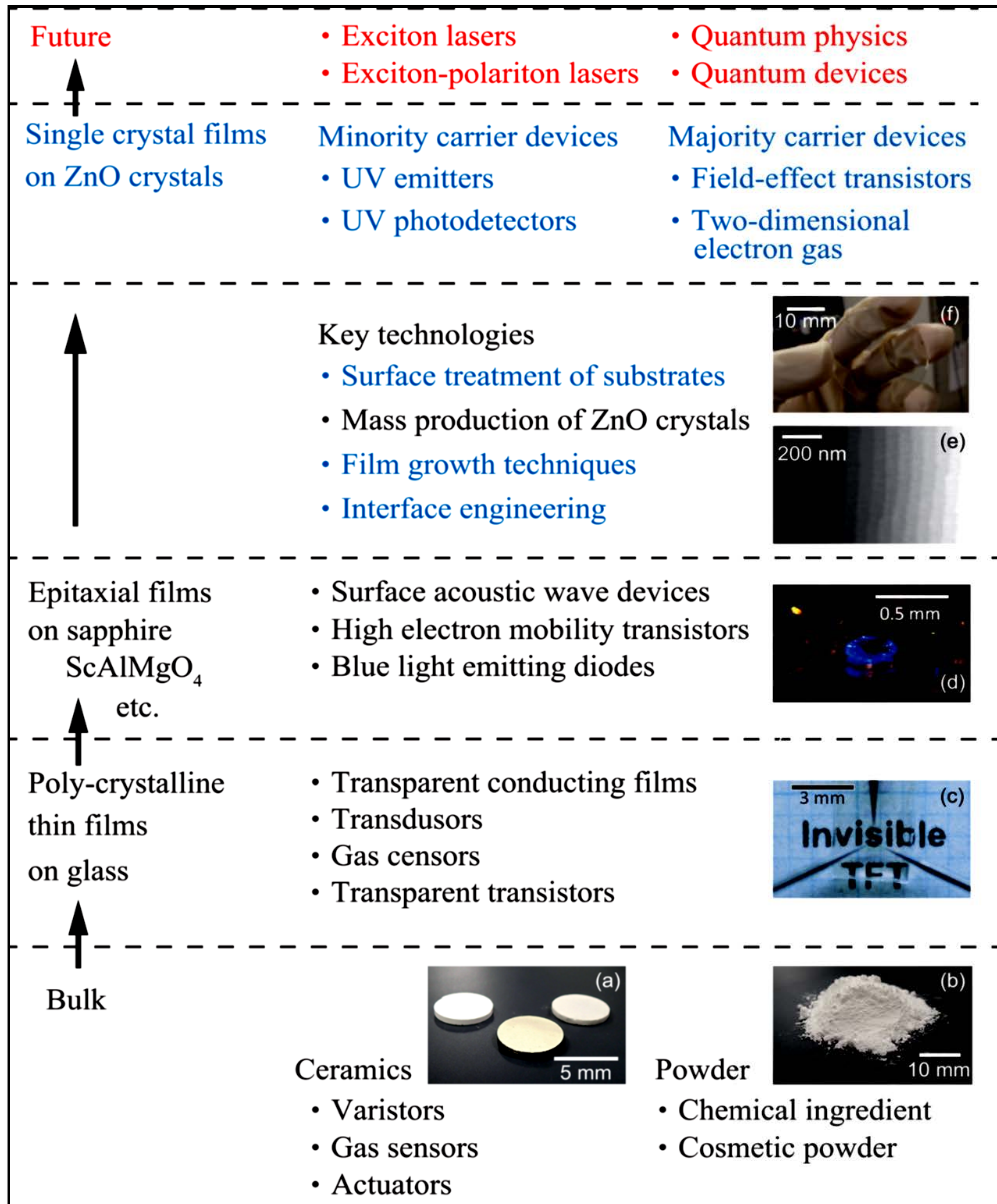

Fig. 2.1: ZnO historical view (bottom to top) regarding research and applications. The inset images are (a) sintered ceramics (b) ZnO powder (c) transistor fabricated on glass substrate (d) blue LED based on a ZnO p–n junction (e) AFM surface image of ZnO single crystal substrate and (f) 2-inch wafer of ZnO single crystal (source [28])

Table 2.1: Comparative properties of ZnO and GaN in a wurtzite crystal structure.(source [2])

Properties	ZnO	GaN
Energy bandgap (eV)	3.40	3.51
Exciton binding energy (meV)	60	24
Effective mass of electron	0.24	0.20
Effective mass of hole	0.59	0.8
Hall mobility of electrons at room temperature ($cm^2V^{-1}S^{-1}$)	200	~1,000
Hall mobility of holes at room temperature ($cm^2V^{-1}S^{-1}$)	⩽50	⩽200
Saturation velocity of electrons (10^7 cm^1S^{-1})	3.2	2-2.5
Lattice parameters: a (nm) c (nm)	 0.3249 0.5207	 0.3189 0.5185
Single crystal substrate availability	Yes	No
Wet chemical etching	Yes	No

2.2. Optical Properties of ZnO

The extrinsic and intrinsic/native point defect-related properties of ZnO or any other semiconductor materials can be analysed by optical characterisations. Intrinsic-type optical transitions occur between valence-band free holes and conduction-band free electrons, together with exciton-type emissions. The Coulombic force between electrons and holes with identical group velocity is responsible for excitonic emission. Actually, exciton is a couple of bound electron and hole and act like a single quasi-particle (such as hydrogen atom) with no net charge. This shows that an exciton is a particle, which transfer energy but no charge. Band gap energy is always higher than exciton energy. Excitons may be free or bound with quantised energy states. Free excitons can move freely within a crystal lattice as a neutral single entity, while bound excitons are self-trapped or localised. A bandgap emission mainly consists of free and donor/acceptor bound exciton emission with the possibility longitudinal optical (LO) phonon peaks. The appearance of LO phonons emission is depending on the crystalline quality of the material. High crystalline quality materials have prominent LO phonon peaks. Various recombination lines of free and bound exciton optical emission along with localization energy and their chemical identity are displayed in Table 2.2. Luminescence optical features provide qualitative information about native and extrinsic additive defects, impurities, crystal quality, dopants and electrical characteristics such as n or p-type conductivity. Emission or absorption optical features are influenced by doping elements, defects and impurity concentrations, which generate discrete energy states in the band gap region. [35-38]

Table 2.2: ZnO free and bound exciton recombination lines, peak transition and localisation energy relative to A_T line and their associated chemical nature. Here A_T (transverse) and A_L (longitudinal) are free A exciton emission lines (source [35, 39]).

Line name	Peak energy (eV)	Localisation energy (meV)	Chemical origin
$\mathbf{A_L}$	3.3772		
$\mathbf{A_T}$	3.3759		
I_0	3.3725	3.4	Al
I_1	3.3718	4.1	Ga
I_2	3.3674	8.5	In
I_3	3.3665	9.4	In
I_4	3.3628	13.1	H
I_5	3.3614	14.5	-
I_6	3.3608	15.1	Al
I_7	3.3600	15.9	-
I_8	3.3598	16.1	Ga
I_9	3.3567	19.2	In
I_{10}	3.3531	22.8	-
I_{11}	3.3484	27.5	-

2.2.1. Defects in ZnO

Imperfections and impurities in a perturbed crystal lattice structure of ZnO produce native or intrinsic-type defects. The study of defect control and their nature in ZnO has attracted significant attention because of its novel applications in various fields.[40] ZnO is simply composed of two elements (zinc and oxygen) but the chemistry

of their defects is very complex. [41] Luminescence is a highly valuable technique for detecting and investigating defects and dopants in all types of semiconductors.[42] A number of PL emission peaks can be observed in the visible and UV wavelength range for ZnO, which strongly depend on their dimensional nature, synthesis technique and morphological features.[43] A characteristic PL spectrum for ZnO with different excitonic and radiative recombination emission peaks is depicted in figure 2.2. This figure shows a dominant PL UV emission peak attributed to bound exciton emission along with LO phonon peaks. Another emission peak at 3.22 eV energy belongs to a donor–acceptor-pair (DAP) recombination of ZnO. The DAP emission peak is followed by LO phonon replicas (E_{LO}) with a common separation energy of 72 meV, which shows the crystalline quality of the material. Another broad luminescence peak around 2.45 eV within the green–blue wavelength range corresponds to native points defects or deep-level emission of ZnO.[35]

The origin of intrinsic-type defects is related to crystal structure deficiencies, which are composed of vacancies, interstitials or antisites in a material. In the current case, ZnO has a number of native defects with different ionisation energies, including zinc or oxygen vacancies (V_{Zn} or V_O), zinc or oxygen antisites (Zn_O or O_{Zn}), and oxygen and zinc interstitials (O_i or Zn_i).[34] These unwanted defects degrade the ZnO optical quality and produce energy states in the bandgap region. A schematic diagram of various intrinsic defects with their associated transition energy levels within the band gap region are depicted in figure 2.3. The optoelectronic characteristics of ZnO may be affected as long as the defects are electrically and optically active. Another important factor is the interaction of extrinsic impurities with native defects, which create donor or acceptor compensation in ZnO. Several reports of experimental and theoretical research on the control and formation of native defects in ZnO have been published.[34, 44, 45] However,

the origin and nature of native point defects are still unclear and controversial, and need further investigation to deliver ZnO into device applications. Table 2.3 provides a summary of intrinsic defects in the visible spectral region, along with the defect properties.[46]

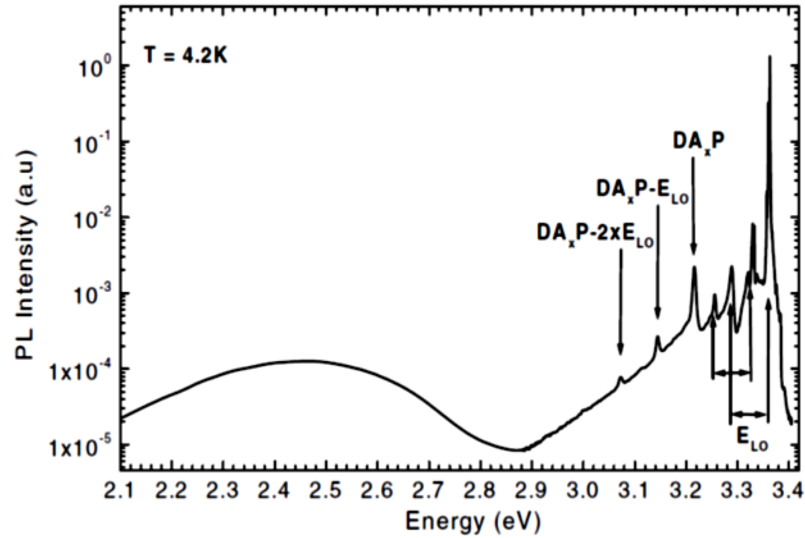

Fig. 2.2: High-resolution PL spectrum of bulk ZnO at low temperature with excitonic (3.3–3.4 eV) and non-excitonic PL emission peaks. DAP is the donor–acceptor-pair recombination peak, while E_{LO} is the LO phonon energy, which is equal to 72 meV in the case of ZnO.(source [35])

The concentration of native defects is strongly dependent on their formation energy. Jannoti et al., using density function theory, and found an exponential equation for concentration of intrinsic defects in ZnO as follows:

$$C = N_{sites}\ e^{-E_f/KT} \tag{2.1}$$

where c is the concentration of native defects, N_{sites} represents the site number incorporated by defects, E_f is the formation energy, K is the Boltzmann constant and T is the temperature.[47] Equation 2.1 shows that the defect concentration and formation

energy have an inverse exponential relationship, which implies that a high number of defects is associated with low formation energy, and it is not possible to form defects with high formation energy. [2] The formation energies for ZnO intrinsic defects are calculated by the local density approximation (LDA) method and plotted against Fermi energy level, as shown in figure 2.4. This figure shows that under zinc-rich conditions, oxygen vacancy (V_O) has lower formation energy than zinc interstitials (Zn_i), resulting in a higher concentration of V_O. [47] The native defects in ZnO can be donor-like types such as V_O, Zn_i or acceptor types such as V_{Zn}, O_{Zn}, and O_i.The ionisation energy for ZnO native defects varies from ~0.05 to 2.8 eV.[2, 48] Because of differences in ionisation energy, temperature strongly affects the relative concentration of different types of defects. Among all native defects, V_O and Zn_i are the main defects that have been attributed to n-type conductivity in undoped ZnO, but there is still controversy about which is the dominant native defect. Another important factor is experimental growth conditions and the amount of O_2 or Zn vapour contents in the chamber environment during growth. For example, Zn_i is the main native defect in zinc-rich conditions, while V_O may be the main defect under reducing growth conditions. Under reducing conditions and high temperatures, oxygen vacancies are expected to dominate because of its lowest formation energy as shown in figure 2.4 [40, 49]

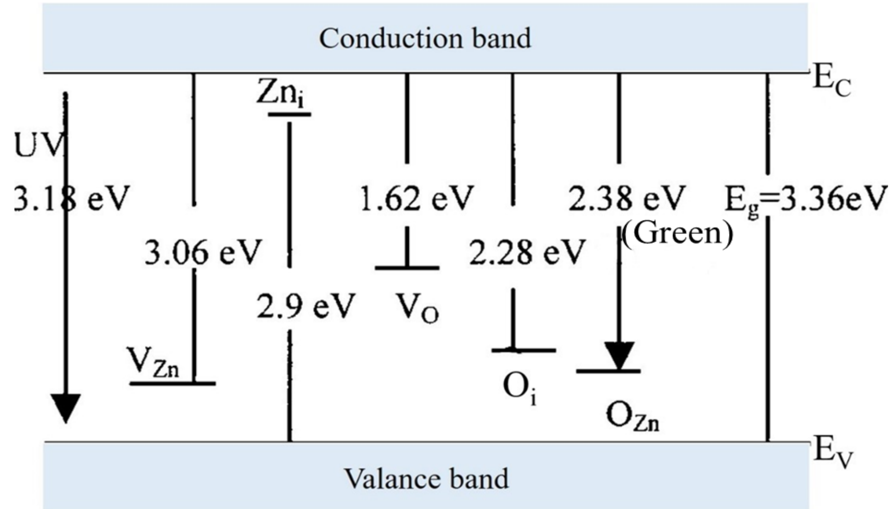

Fig. 2.3: Schematic representation of different transition energy levels due to intrinsic point defects in a ZnO film within the bandgap region, calculated by the full-potential linear muffin-tin orbital procedure. (source [50])

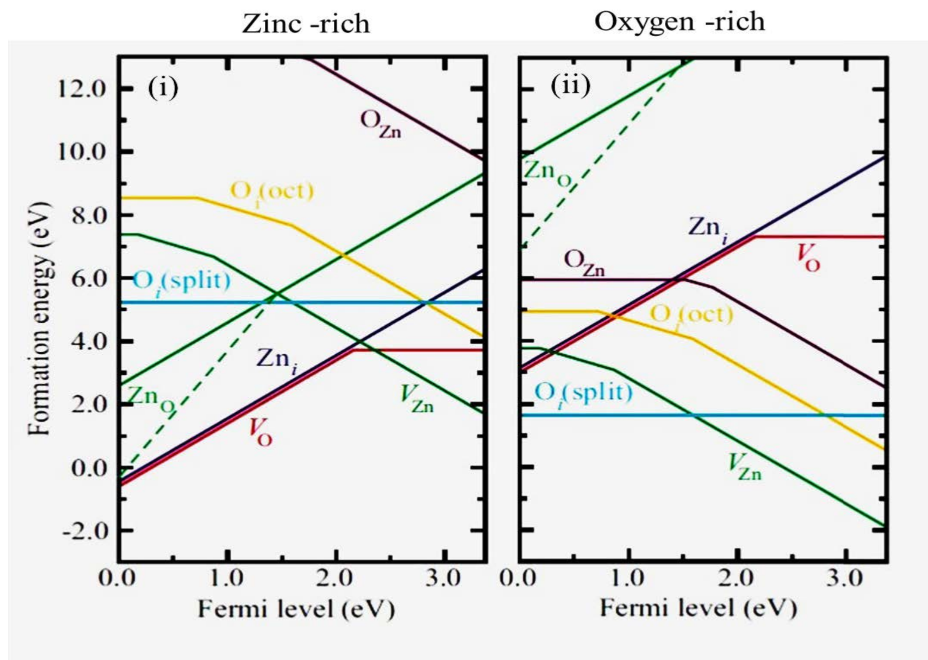

Fig. 2.4: Formation energy of intrinsic defects versus position of Fermi energy level for both (i) zinc-rich and (ii) oxygen-rich conditions of ZnO. Zero Fermi energy level shows the valence band maxima and the charge states of defects are shown by slope. Kinks in the curve represent transitions between defect charge states. (source [47])

Table 2.3: Deep-level defects and their corresponding features (source [46])

Defect origin	**Transition energy/luminescence peak energy (eV)**	**Colour**	**Defect type**
V_{Zn} (vacancy due to Zn)	2.3, 2.35, 2.53	Green luminescence	Acceptor
Li_{Zn} (Zn substitute by Li (lithium))	1.93, 2.07, 2.17	Yellow luminescence	Acceptor
V_O (vacancy due to oxygen)	2.35, 2.36, 2.45, 2.48, 2.50, 2.53	Green luminescence	Donor
O_i (Oxygen interstitial)	1.69, 1.79 1.95, 1.98, 2.03, 2.06, 2.10 2.26	Red luminescence Orange luminescence Green luminescence	Acceptor

2.2.2. Hydrogen in ZnO

The strong bonding interaction between H and oxygen usually lead to inadvertent incorporation of H in oxide-based materials. In this way, ZnO has a high probability of contamination by common H extrinsic impurities or defects, which improve their n-type electronic nature.[51, 52] Significantly, the presence of H in a ZnO crystal lattice alters its optical and electrical characteristics. The H impurity in ZnO can acts as a donor in two different structural state: (a) interstitial H and (b) substitution of H on oxygen site.[52] Because of its high mobility, H can be easily eliminated from ZnO by thermal

treatment.[53] In most semiconductors, H in its interstitial form has an amphoteric impurity nature. Hydrogen may incorporate as an acceptor in n-type materials and behaves like a donor in p-type materials. However, in ZnO, H solely introduces a positive charge state, which leads to its nature as a shallow donor or n-type promoter. This non-amphoteric nature of H in ZnO reflects that H increases n-type conductivity.[54] The most common type of extrinsic and unintentional impurity in ZnO is H, which strongly modifies n-type conductivity and acts as a donor.[47] H induces a shallow donor state because of the highly stable and favourable position of the Zn-O bond centre for H interstitial impurities, as reported by Van de Walle.[54] According to PL analysis, the H shallow donor state formed below near conduction band-edge at 40 meV energy difference.[55]

Annealing of ZnO in reducing ambient conditions such as H_2 gas may induces defects or ZnO evaporation. Therefore, H plasma is the best technique to finely produce H impurities in ZnO.[56] H can easily and rapidly diffuse in ZnO following exposure to plasma even at 100ºC. The thermal stability of diffused H in ZnO is higher following the ion implantation method than with plasma exposure owing to trapping by residual damaged. Because of the low thermal stability of diffused H in ZnO, H can be completely eliminated at ≥500ºC post-annealing temperature.[57] H plasma is known to be highly diffusive, with diffusivity rate of 0.2 cm^2/s, and can diffuse through ZnO at depths of several microns at 200ºC.[58] There are four possible bonding positions of H impurity in a ZnO lattice structure, as shown in figure 2.5. In ZnO structure lattice, all the H bonding locations, which have smallest formation energy, are produced donor sites [59, 60]

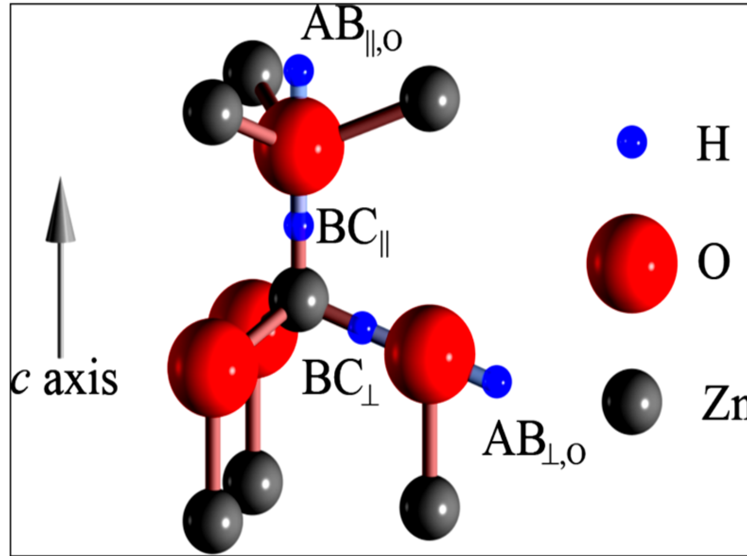

Fig. 2.5: Four possible bonding configurations of H in a ZnO crystal structure. Position of H in ZnO are shown in blue, while oxygen is red and Zn are blackish colour balls. (source [59])

Moreover, H incorporation strongly alters the optical properties of ZnO, such as NBE and deep-level emissions in PL/CL spectra. H incorporation in ZnO passivates the radiative recombination of deep-level states and enhances UV emission, but this depends strongly on the impurities and defects content of the material. For example, green emissions in PL/CL spectra due to zinc vacancies are suppressed by H doping and create O–H bonds in a ZnO lattice.[47] Figure 2.6 depicts PL spectra for ZnO; one is polycrystalline with high-defects/deep-level emissions and the other is a high-quality single crystal with low deep-level emissions. The comparative results show that deep-level or visible emissions are completely quenched by H plasma; NBE emissions are also enhanced more than 10 times. Conversely, there is no deep-level emission in the hydrothermal single crystal originally, so the increase in NBE emission is negligible. Therefore, H incorporation is highly dependent on the physical and chemical properties of the initial ZnO material. [55]

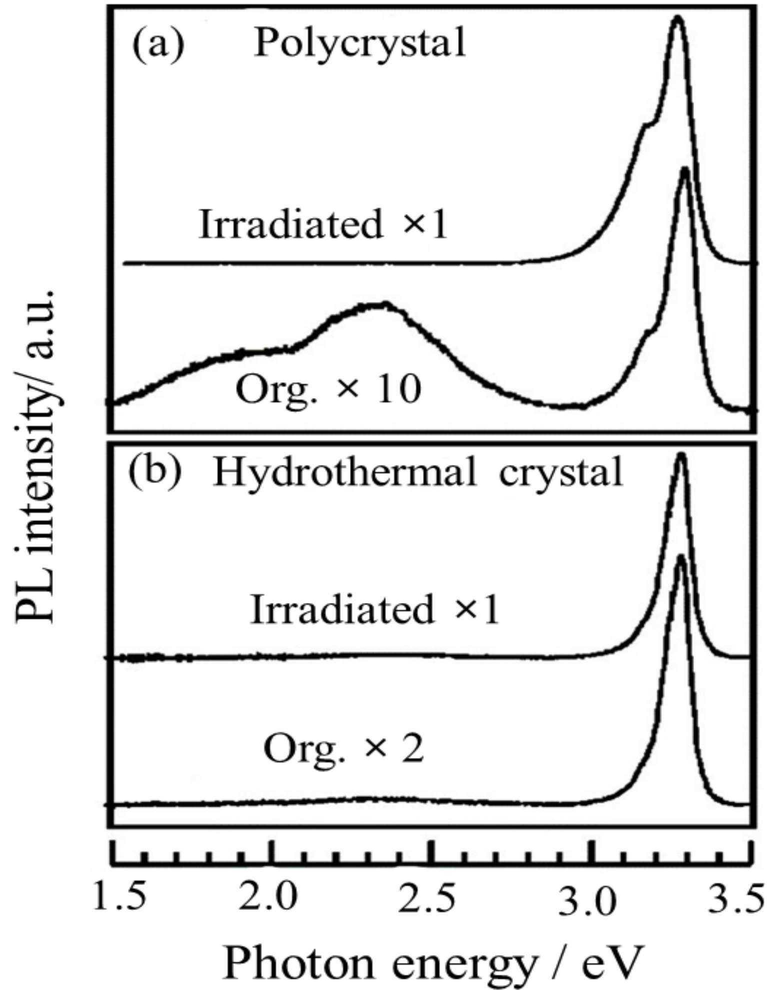

Fig. 2.6: PL spectra for two types of ZnO: (a) polycrystalline pellet and (b) single crystal. Both (a) and (b) show PL spectra for the as-grown and hydrogen plasma-treated samples for comparison. (source [55])

2.3. Acceptors in ZnO and MgZnO

P-type ZnO material is an essential component in the fabrication of bipolar optoelectronic devices. The p-type property is directly related to acceptor/hole concentration in a semiconductor, which can be investigated via optical or electrical characterisation. Intrinsic defects like V_O, Zn_i, or Zn_O and extrinsic H impurities are acceptor killers, which hinder production of p-type ZnO material. The formation energy of intrinsic defects is high owing to strong bonds in ZnO. Several studies have produced

p-type ZnO by varying intrinsic or extrinsic impurities, but it remains a challenge to produce reliable, reproducible and stable p-type ZnO material.[2, 61] An example of intrinsic p-type ZnO is the growth in oxygen-rich ambient conditions that produces p-type ZnO with hole carriers of ~10^{18}/cm^3 and acceptor-bound exciton optical emissions at 370.43 nm in PL spectra.[62]

Besides p-type ZnO fabrication by intrinsic defect variation, the acceptors/holes in ZnO can be produced by incorporating extrinsic impurities. Several efforts have been made in relation to extrinsic impurity doping in ZnO, involving group I elements such as K, Na and Li and the group V elements P, As, Sb and N. Theoretical calculation shows that the tendency of group I elements is to occupy an interstitial sites instead of Zn substitution are most likely to become a donors. Similarly, P, As and Sb have higher atomic radii than does oxygen, which most probably creates antisites leading to donor behaviour.[63, 64] Among all the extrinsic dopants, N is the most promising and highly explored impurity to produce acceptors/holes, overcome acceptor killers and induce effective acceptor-level optical and electrical features in ZnO, which may lead to p-type.[65, 66] S. H Wei computationally calculated various acceptor energy levels; a schematic representation of acceptor energy levels in ZnO is shown in figure 2.7. [67]

Some obstacles also limit the fabrication of p-type ZnO by adding extrinsic impurities or doping in ZnO. The lowest energy state above valence band maximum (VBM) is N_O (nitrogen on oxygen site) at energy 0.35 eV for group V elements; while for the acceptors on zinc sites due to group 1B elements, the lowest transition energy is at 0.4 eV above VBM, which are deep-level states. Conversely, the group 1A acceptors formed on zinc sites are of a shallow nature, which cannot lead to useful acceptors because of self-compensation.[67, 68] Up to now, the most attractive doping element for p-type ZnO is N, owing to its similar ionic radii; the well-matched bond length of Zn-O

(0.193 nm) and Zn-N (0.188 nm), and low ionisation energy.[64, 69] There are still some solubility issues with N doping. Solubility of N in ZnO is enhanced by using molecular N such as N_2, NO, NO_2 or N_2O. Solubility directly corresponds to the chemical potential of molecular N. NO and NO_2 are the most soluble doping sources, and they also limit the formation of donor compensator molecules.[67, 70] To further increase the solubility and the acceptor/hole concentration in ZnO, magnesium (Mg) doping is used. Mg replaces Zn to create a ternary $Mg_xZn_{1-x}O$ ($0 \leq x \leq 1$) semiconductor with higher band energy. Mg doping directly enhances acceptor/hole carriers in ZnO, and lowers the formation energy for N. By lowering the formation energy of the N doping source, solubility is increased, which leads to enhanced acceptor/hole carrier concentration.[4]

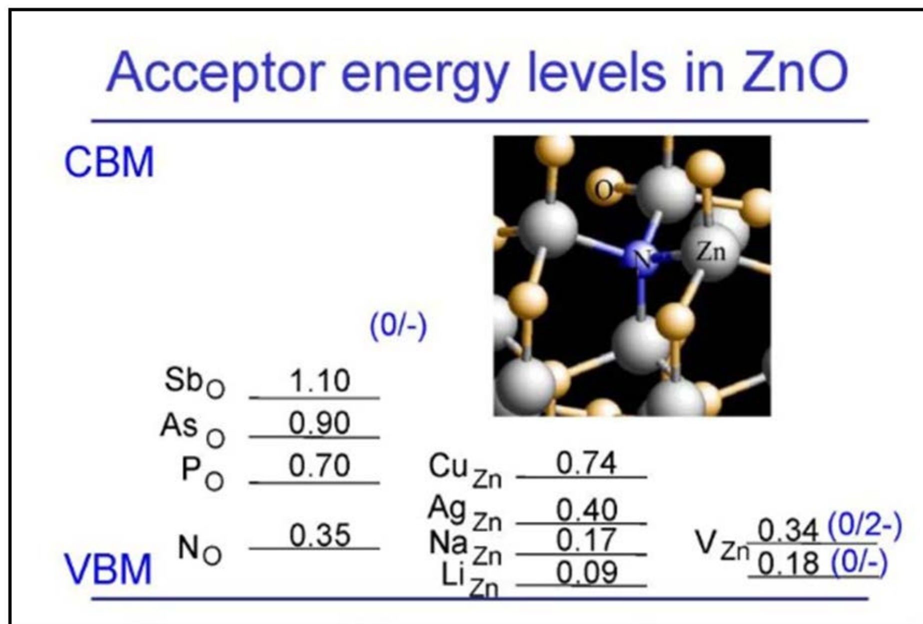

Fig. 2.7: Schematic figure showing various acceptor energy levels in ZnO by a range of extrinsic impurity doping. The inset figure shows nitrogen impurity placement in a ZnO lattice structure (source [67]).

2.4. Band Gap Engineering of ZnO

The tuning of ZnO band gap energy is a crucial factor for consideration in the fabrication of ZnO-based optoelectronic applications in the low- and high-energy optical spectral range. For fabrication of heterostructure, the selection of layer materials is dependent on their properties. Layer materials with similar properties such as crystal structure, constant lattice and electron affinity can easily produce a device heterostructure with the required properties.[1, 2, 22, 71] CdO (cadmium oxide), MgO (magnesium oxide) and BeO (beryllium oxide) are the more well-explored materials for bandgap engineering of ZnO-based heterostructure. The empirical relationship equation 2.2 is used for the determination of bandgap energy for a ternary $Zn_{1-x}A_x$O alloy semiconductor, where A denotes Cd, Be or Mg elements:[2, 72]

$$E_g(x) = (1\text{-}x)\, E_{ZnO} + xE_{AO} + \mathrm{b}x^2 - \mathrm{b}x \tag{2.2}$$

where b is the bowing parameter, x is the atomic fraction of AO-doped material, $E_g(x)$ is the bandgap energy of the ternary alloy ($Zn_{1-x}A_x$O) and E_{ZnO} and E_{AO} are the bandgap energies of ZnO- and AO-doped materials. MgO and BeO are used to increase the ZnO bandgap energy, while CdO is used to decrease the bandgap. Theoretically, the optical bandgap for $Zn_{1-x}A_x$O alloy semiconductors is in the range of 0.9 eV (CdO) to 10.6 eV (BeO) and is determined according to the amount of A (Cd, Mg or Be). Interestingly, BeZnO has wurtzite crystal structure for all ranges of Be doping, but there are toxicity concerns in the case of BeO alloying with ZnO. Conversely, Cd doping narrows the bandgap of ZnO towards the visible wavelength region, but CdO has a cubic crystal structure and can change the ZnO wurtzite structure with the addition of large amounts.[36, 73] In bandgap engineering of ZnO, MgO-ZnO alloy is the most highly

explored material for ZnO-based heterostructures such as in MQWs and 2DEG systems. Therefore, a detailed investigation of MgZnO ternary semiconductor is necessary.

2.4.1. Mg-doped ZnO Alloy

Mg-doped ZnO alloy (MgZnO) is an environmentally friendly alloy, exhibiting a direct band gap semiconductor with an optical wavelength range from ZnO (~375 nm) to MgO (~161 nm).[74] MgZnO can acts as a capping/barrier material in heterostructures owing to its higher bandgap and bond length similar to that of ZnO; the very similar ionic radius of Mg (0.057 nm) and Zn (0.060 nm); and their wurtzite crystal structure, which is maintained even up to 33% Mg content. The small ionic radius difference between Zn and Mg cannot lead to significant changes in the lattice parameters by replacing Zn by Mg within the solubility limit of 36 mol %. [75, 76] By incorporating Mg into a ZnO crystal lattice, the *a* lattice parameter increases, while the *c* lattice parameter decreases, but no significant change occurs in the cell volume up to the solubility limit. Figure 2.8 provides a graphical representation of bandgap energy as a function of Mg content in MgZnO alloy material deposited on a sapphire substrate using the pulsed laser deposition (PLD) method.[77, 78] Generally, the crystal structure and bandgap of an MgZnO alloy system depends on the growth techniques, substrate effects and growth conditions. The optical bandgap energy as a function of the lattice parameter for (Mg, Cd)/ZnO and (Al, In)/GaN alloy systems is shown in figure 2.9. As GaN materials are strong competitors with ZnO, both band gaps are shown here for comparison. For example, the GaN bandgap increases with aluminium (Al) doping, as does ZnO with Mg; and decreases with indium (In) doping, as does ZnO with Cd.

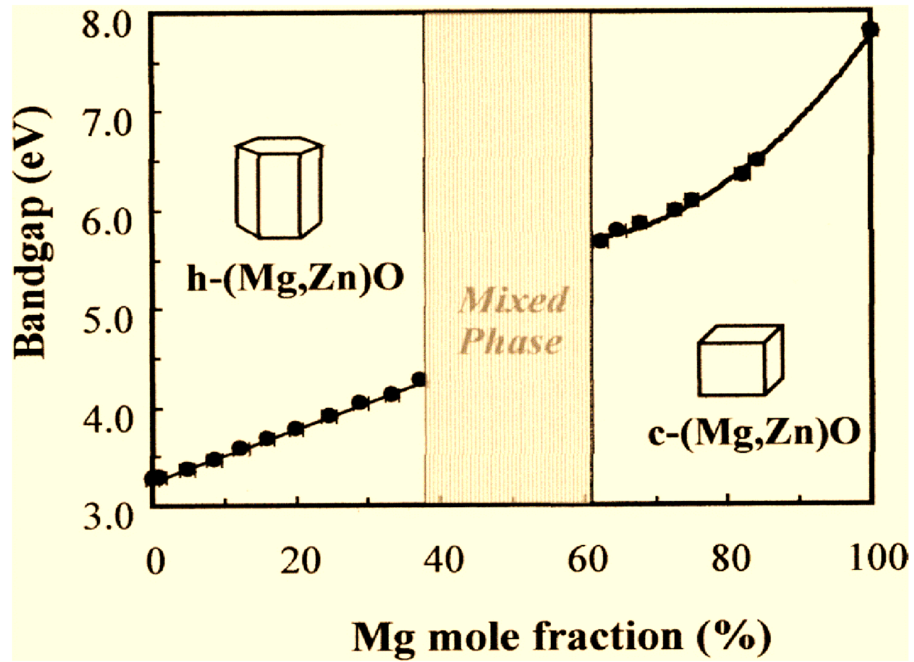

Fig. 2.8: Bandgap energy versus Mg mole fraction for an MgZnO alloy. This figure also demonstrates that the phase information region, hexagonal phase h-(Mg.Zn)O, mixed phase and cubic phase c-(Mg.Zn)O depend on the Mg concentration (source [78]).

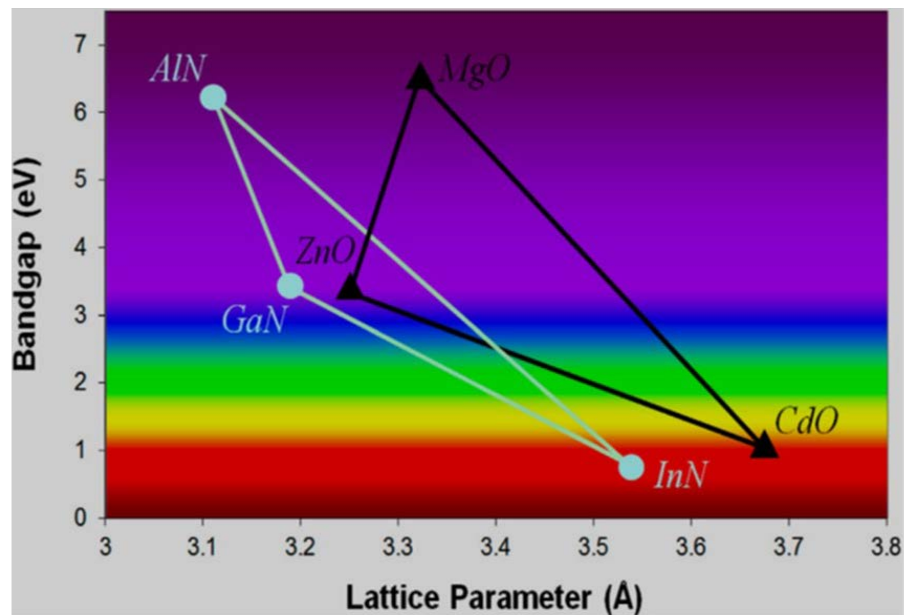

Fig. 2.9: Bandgap energy versus lattice parameter for (Al,In)GaN and (Mg,Cd)ZnO alloying. AlN and MgO are in the deep UV region, while InN and CdO are in the visible region (source [73]).

2.5. MgZnO/ZnO Heterostructures

Heterostructures are a potential component in most semiconductor-based devices and solid-state physics. For example, single heterostructures, double heterostructures, single and MQWs, nano-heterostructures, and superlattices are highly explored material structures for fundamental research and device applications in the semiconductor research community. The design and concept of heterostructures is basically used to control the properties of semiconductor materials and devices such as conductivity, mobility, carrier concentration and bandgaps. [79, 80] Currently, ZnO-based heterostructures are receiving much attention in fundamental physics research and novel device applications like strong-correlated electron, quantum Hall effect and 2DEG systems.[28, 81] The tuning of bandgap energy in ZnO-based heterostructure layers is highly significant in the fabrication of a well-matched barrier or capping layer. To achieve a quality heterostructure with novel functionalities, one needs to fabricate heterostructure layers with closely matched properties including lattice parameters, electron affinity and substrate selection, as well as the least impurities and disorders.[2, 28] Mg-doped ZnO alloy is a highly investigated material in the family of ZnO-based heterostructures. MgZnO is a high band gap material and acts as a barrier material because it has a similar bond length to ZnO, its bandgap offset is 0.6 eV, and its wurtzite crystal structure is maintained even up to moderate Mg addition. [76, 78] K. Nakahara et al. successfully fabricated a LED based on ZnO and MgZnO layers, as shown in figure 2.10. A ZnO single crystal substrate is used here to reduce extended defects, while N is used to make a p-type layer of MgZnO.

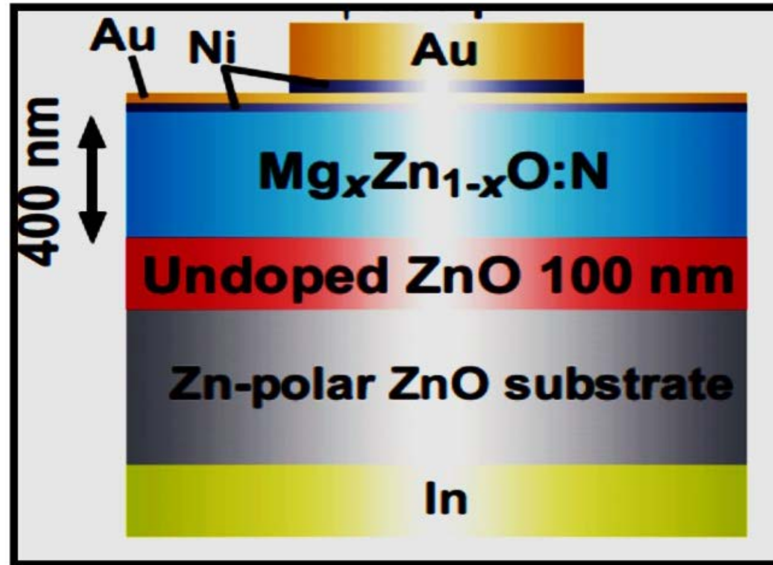

Fig. 2.10: Schematic view of a LED heterostructure made of ZnO and N-doped MgZnO layer acting as a p–n bipolar junction. The emission spectra are in the UV spectral energy range, at 3.26–3.10 eV (source [82]).

2.5.1. Two-Dimensional Electron Gas

ZnO-based heterostructures have been widely investigated for use in bipolar junction heterostructure devices. Besides the novel characteristics of ZnO material, the key obstacle is the stability and reproducibility of p-type doping in ZnO; conversely, GaN technology is mature in this regard.[2, 21, 28] To utilise ZnO for electronic applications, significant research has been undertaken on the control and confinement of electron carriers at the MgZnO/ZnO heterostructure interface. These confined carriers at the interface are called 2DEG and their luminescence or optical emission are called H-band emission, as shown in figure 2.11.[83, 84] 2DEG at the MgZnO/ZnO heterointerface offer remarkable opportunities in oxide electronics and quantum devices because of their higher electron mobility and carrier concentration. Various parameters affect the mobility and carrier density, including Mg concentration, film thickness, temperature, defects,

impurities, substrate and growth techniques.[28, 85] 2DEGs have a unique advantage over bulk electrons owing to the neglecting of scattering from ionised impurity, which results in an enormous increase in electron mobility. The main advantage is the control of electron/hole carrier kinetics and dynamics such as mobility, polarisation and density of states for optoelectronics applications.[28, 86, 87] Recently, the observation of the quantum Hall effect and high mobility (>10^6 cm^2/Vs) in MgZnO/ZnO-based 2DEG systems has prompted further exploration by the scientific community.[88, 89]

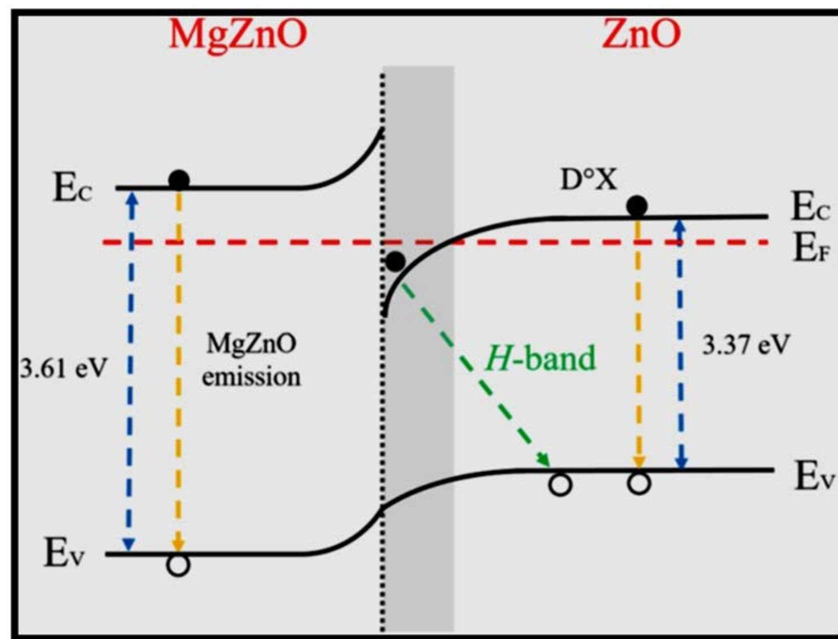

Fig. 2.11: MgZnO/ZnO heterostructure band diagram and its heterointerface H-band radiative recombination. The 2DEG or H-band emission is between the electrons in the triangular potential well and the holes at the ZnO valence band. E_C, E_V and E_F are conduction band minima, valence band maxima and Fermi energy level, respectively (source [84]).

2DEG is naturally created at the MgZnO/ZnO interface because of the polarisation mismatch and band offset between ZnO and MgZnO layers and no

requirement for impurity doping or an external field application. The very weak symmetric nature of the wurtzite crystal structure of ZnO creates spontaneous polarisation (P_{Sp}) along the polar access. The application of stress, lattice deformation produces separation of the centres of positive and negative charges, which is defined as dipole moments. The accumulation of dipole moments gives rise to polar charges on the crystal surface and induces a piezoelectric polarisation (P_{Pe}) in the layer.[90, 91] Polarisation of MgZnO and ZnO induces a very high internal electric field of ~5 MV/cm at the heterointerface region and is usually compensated by surface adsorbents. The exact potential relaxation mechanism remains unclear.[28, 90, 92] The overall polarisation discontinuity at the interface creates uncompensated bound charges in the MgZnO/ZnO heterostructure interface. Furthermore, the induced high electric field confines the free carriers in a triangular potential well at the interface region, the so-called 2DEG. The MgZnO/ZnO heterointerface hosts 2DEGs having high electron density concentrations and mobility, which can be utilised in HEMT-based applications. The carrier density of 2DEG is influenced by Mg concentration and layer dimensions.[28, 90] Figure 2.12 provides the historical background (2007–16) of research into 2DEG mobility as a function of carrier concentration in MgZnO/ZnO system. Two different relationships for mobility (μ) versus carrier density (n) shown by the dotted linear line are $\mu \, \alpha \, n$ (low density) and $\mu \, \boldsymbol{\alpha} \, n^{-3/2}$ (high density). For lower carrier density (n), the mobility is limited due to charged impurity scattering. Conversely, the alloy or interface scattering is restricted and affects mobility for the higher density (n) region.[88]

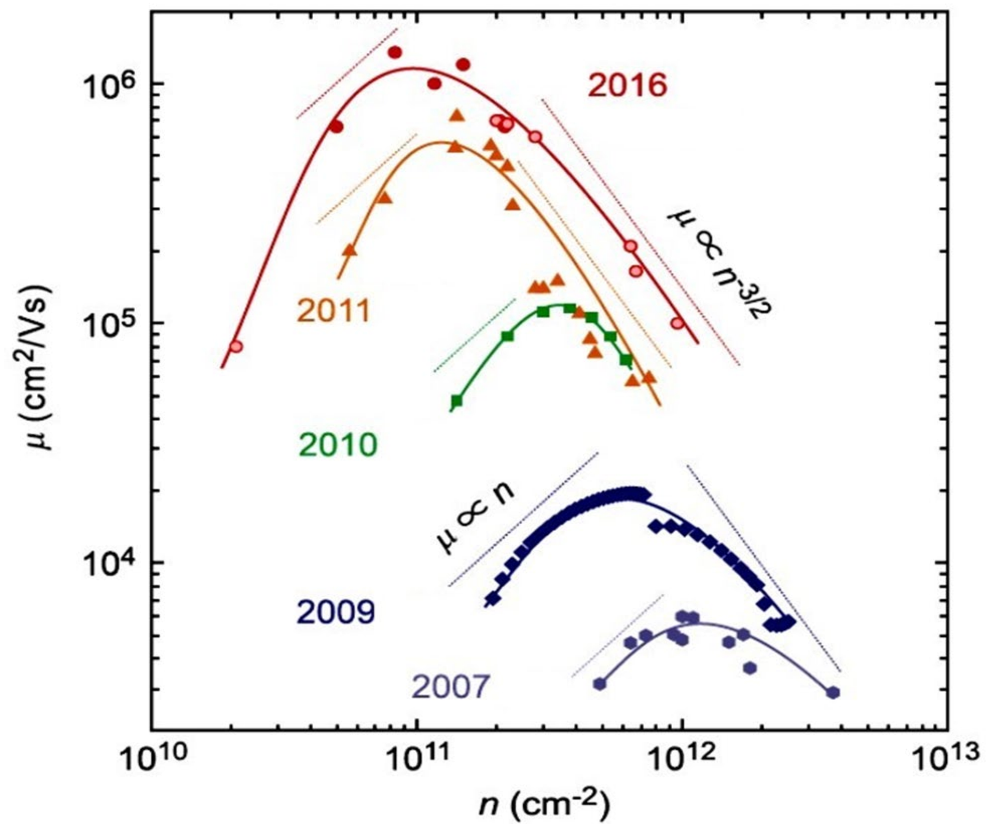

Fig. 2.12: A historical (2007–16) representation of mobility (μ) versus carrier concentration (n). All data taken at temperature ⩽2K for a MgZnO/ZnO 2DEG system. The mobility increasing with carrier concentration and reached to saturated value at the curve top. After μ saturation at some value of n, the mobility decreasing with further increasing n. The peak of each curve represents the saturated value for mobility (source [88]).

2.6. Two-dimensional (2D) Materials

2D materials are a class of nanomaterials, currently gaining considerable attention because of their exciting optical, electrical and chemical properties compared with their bulk counterparts.[93] 2D nanostructures are an easy source of 2D material-based systems with very high specific surface area, suitable for catalyst, sensor and energy storage device applications.[93, 94] Ultrathin 2D nanosheets have some special and unique

properties compared with other nanostructures like nanoparticles (0D), nanowires (1D) and bulk (3D). First, the single layer of a 2D ultrathin nanosheet has strong electron confinement with no inter-layer interaction, which makes it distinctive for basic material research and nanoelectronics applications. Second, the very high mechanical stability and excellent optical transparency make it flexible for transparent optoelectronic application. Third, the high lateral dimension with ultrathin bulk part creates high specific surface area, making it a potential candidate for surface-active device applications. [95, 96] Usually, the lateral dimension of a nanosheet is typically up to several microns or greater than 100 nm, and its thickness is in the order of atomic layer level, or less than 5 nm.

While investigations date back several decades, major progress was made in 2D materials research when graphene was successfully exfoliated from graphite using scotch tape.[96, 97] The characteristic 2D feature of a nanosheet offers unparalleled ability to finely tune its optical, electronic and chemical properties owing to electron confinement in the 2D layer. For example, graphene, a single atomic layer nanosheet, has appealing characteristics including very high mobility at room temperature, very high electrical and thermal conductive properties, superb optical transparency, high Young modulus and quantum Hall effect.[93, 96, 97] In parallel with graphene, other 2D nanostructure materials are also explored, such as TMDs, h-BNs and transition metal oxides.[93, 98, 99] In particular, a variety of boron and metal dichalcogenide 2D forms of h-BN, MoS_2, WS_2, $MoSe_2$ and InSe with stable properties under ambient conditions have been recently investigated.[16, 100] 2D nanostructure materials are fabricated by various techniques, such as mechanical force-assisted liquid exfoliation, chemical vapour deposition and the wet chemical approach. A crucial downside with all current synthesis techniques is their low production yield. Therefore, a thorough understanding is mandatory to improve facile, viable and reliable synthesis techniques to achieve high production yields for

device applications. Figure 2.13 shows the most highly investigated 2D materials including graphene (center), h-BN, metal and covalent organic frameworks (MOFs and COFs), TMDs, layered double hydroxides (LDHs), black phosphorous (BP) and transition metal carbides or nitrides (MXenes).[93, 96] Among various 2D nanomaterials, binary metal oxide has received little attention.

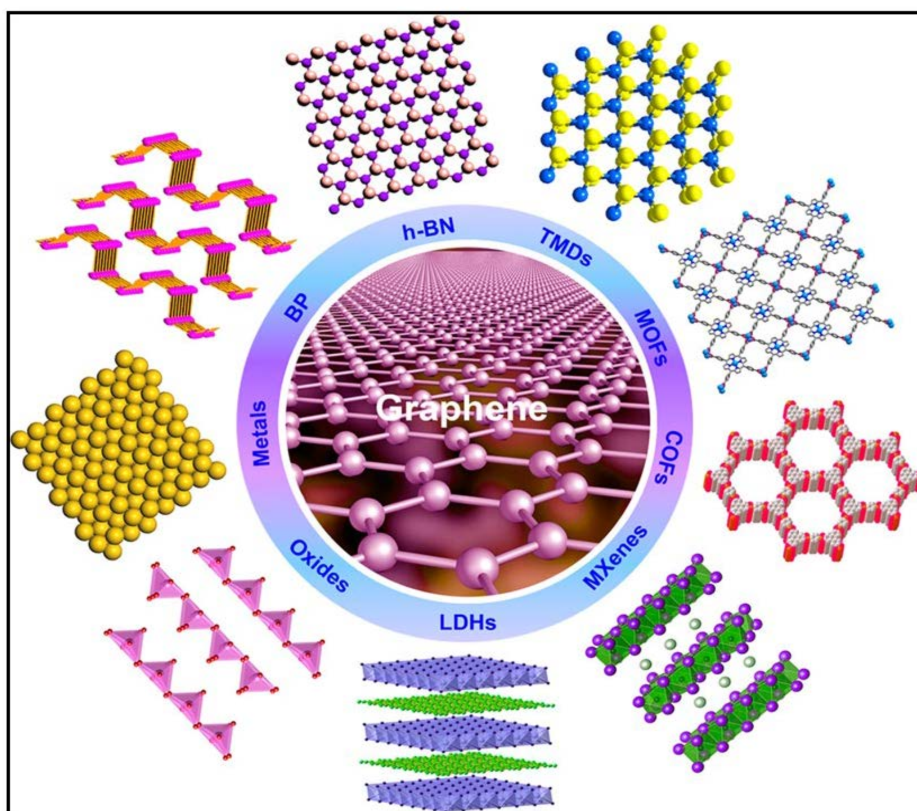

Fig. 2.13: Highly explored materials of the 2D nanostructures family with their corresponding atomic structure (source [96]).

2.6.1. ZnO Nanostructures and 2D Nanosheets

Among all nanostructure materials, metal oxides are a diverse functional material highly utilised in fundamental physics research as well as device applications, whose properties are strongly dependent on its dimension and size. The particular recent

surge of interest is due to their environment stability, relative ease of processing, cost-effectiveness and environmental friendliness, and because they are commonly occurring and non-toxic materials.[101, 102] Therefore, metal oxides have become the ideal candidate for in-depth investigation and large-scale production of 2D nanostructure materials. Some metal oxides, like ZnO, (Mg, Cd)/ZnO, Ga_2O_3 and $(In, Al, Ga)_2O_3$ alloy compound semiconductors have gained much attention.[103-105] Because of their wide bandgap, these materials have advantages over others, such as optical transparency and high operating temperature.

ZnO nanostructure materials of different sizes and shapes have been explored, as shown in figure 2.14.[106] However, the use of these nanomaterials to form the building blocks for integral devices limits their functionality for practical applications. Therefore, a nanostructure in the form of a nanosheet with large lateral dimensions can be easily processed, assembled and manipulated relative to other nanostructures for nanodevice applications.[107, 108] One theoretical finding is that a ZnO nanosheet of less than 1-nm thickness is expected to adopt a graphitic-like stable phase under ambient conditions.[109] Several theoretical calculations have been published on ZnO 2D nanosheets but there is negligible information from an experimental approach. H. Si et al. used first principle calculations for ZnO hexagonal nanosheets and studied their hydrogen storage property. Their theoretical findings confirm that ZnO nanosheets have higher absorption of hydrogen molecules than graphene.[110] Another theoretical study has been conducted on the ability of carbon dioxide (CO_2) absorption for environment cleaning. This theoretical calculation shows that adsorption of CO_2 molecules increased by doping nitrogen, carbon or boron in ZnO monolayer.[111] Most experimental approaches and research are based on the collective behaviour of nanoparticles and nanosheets; there is very limited information on a single nanosheet of ZnO.[112] The

main challenge with a single ZnO nanosheet is to fabricate an ultrathin nanosheets with enough lateral size to easily probe for nano-characterisation. In 2018, an experimental chemical template-assisted approach for ZnO 2D ultrathin nanosheets was employed; the optical and morphological properties of resulting ZnO nanosheets are discussed in figure 2.15. In this work, hexagonal ZnO 2D nanosheets with thickness down to a monolayer and lateral sizes up to 2 microns have been investigated. The ZnO excitonic emission increases with decreasing nanosheet thickness due to reduction in defect densities. [113] Moreover, ZnO 2D nanostructures have more ionicity than graphene, h-BN, silicene or germanene, which may result in significantly different properties from other atomic layer 2D materials. Therefore, the ZnO 2D-type nanostructure is expected to be utilised in deep UV range optoelectronics, catalysis, magnetism, H storage and CO_2 absorption based applications.[110, 111, 113-116]

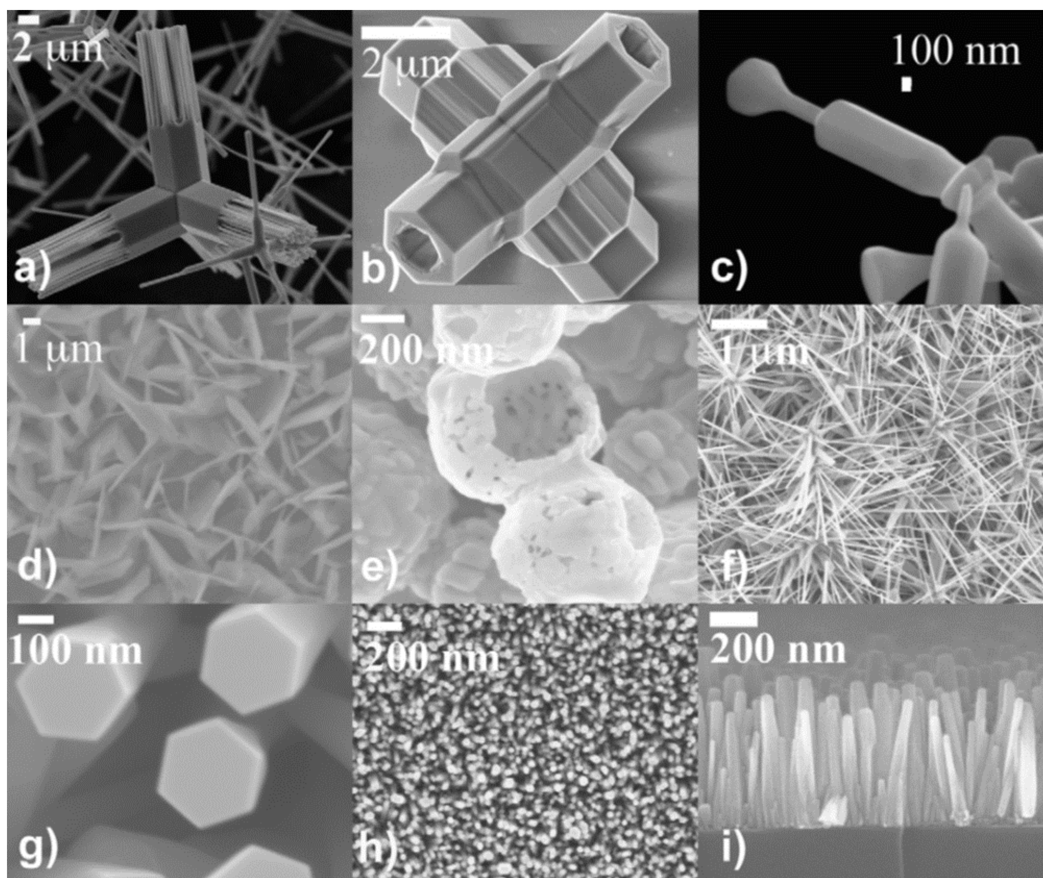

Fig. 2.14: Electron microscopy images of ZnO nanostructures with different shapes and sizes: (a, b) tetrapod nanostructure, (c) nanorods with varying diameters, (d) ensemble nanosheets, (e) nanoshells, (f) multipods and (g, h, and i) nano-rods/wires (source [106]).

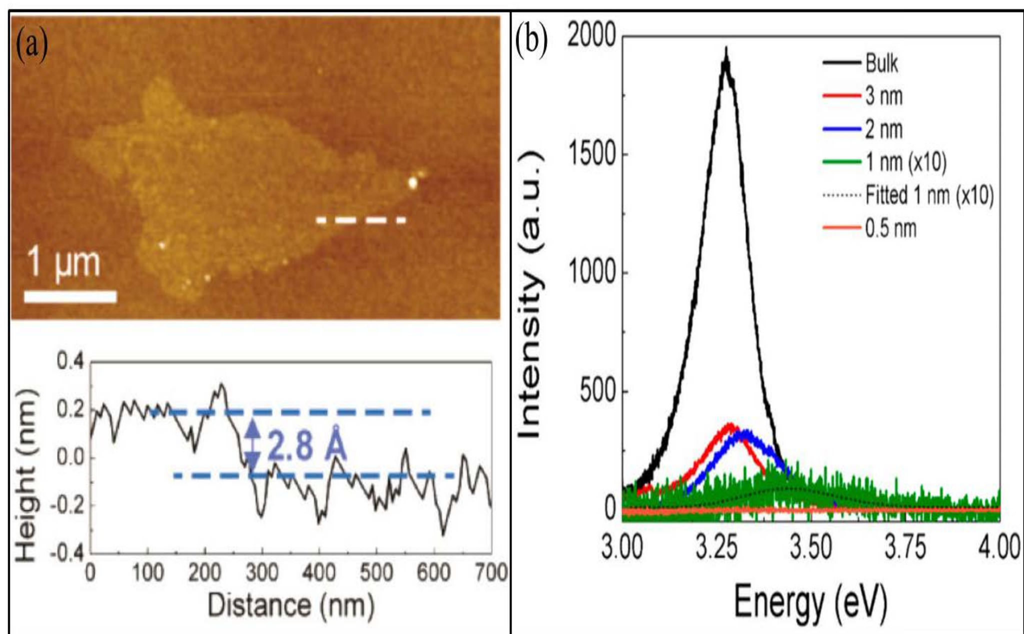

Fig. 2.15: (a) AFM image of a single ZnO nanosheet with corresponding line scan for height profile of thickness 0.28 nm; (b) PL spectra of different ZnO nanosheets along with bulk ZnO with dotted line showing fitting (source [113]).

Chapter 3

3. Experimental Techniques

This chapter discusses the main experimental tools, materials and methods involved in the current research. The target materials used were ZnO-, MgZnO-based materials and the characterisation techniques used, especially luminescence characterisation, are described.

3.1. Characterisation Techniques

A range of characterisation tools and techniques were employed for morphological, optical and structural analysis in this research. AFM and scanning electron microscopy (SEM) were used to determine the shape, size and surface topography of various samples, while X-ray diffraction (XRD) and Raman spectroscopy were used to gather crystal structure information. CL and PL techniques were used in the luminescence spectral investigation. NEXAFS spectroscopy was used in the analysis of unoccupied states of nitrogen and their chemical signatures in MgZnO. Monte Carlo simulation by CASINO programming was utilised for CL interaction volume and penetration depth analysis. These diagnostic techniques are explained in the following sections.

3.1.1. Atomic Force Microscopy

AFM is a powerful characterisation tool used to examine the 3D morphological properties of thin films and nanostructure materials. AFM imaging do not need conductive nature of material and can be used for semiconductors, insulators and conductive type materials. The working principle of AFM is the measurement of force between probing tip and surface of the material. The probing tip of AFM system is scanned on the tiny portion of the sample surface and collected the local morphological information. A schematic view of AFM set-up and tip image (SEM) is shown in figure 3.1. Usually, the probing tip is very sharp in a range of 3 - 6 μm tall and finishes with a tip radius smaller than 10nm.[117] During AFM, both vertical and lateral dimensional features can be measured by using laser beam reflection from cantilever. Generally, two types of AFM operation modes (contact and non-contact) for surface scanning. In contact mode, the tip is in soft physical contact with the sample surface and may cause sample surface degradation. On the other hand, the probing tip does not physically touch the sample surface in non-contact mode operation. The attractive Van der Waals forces play the role in soft non-contact mode operation. The variation in the amplitude is monitored during probing tip oscillation above the sample surface.

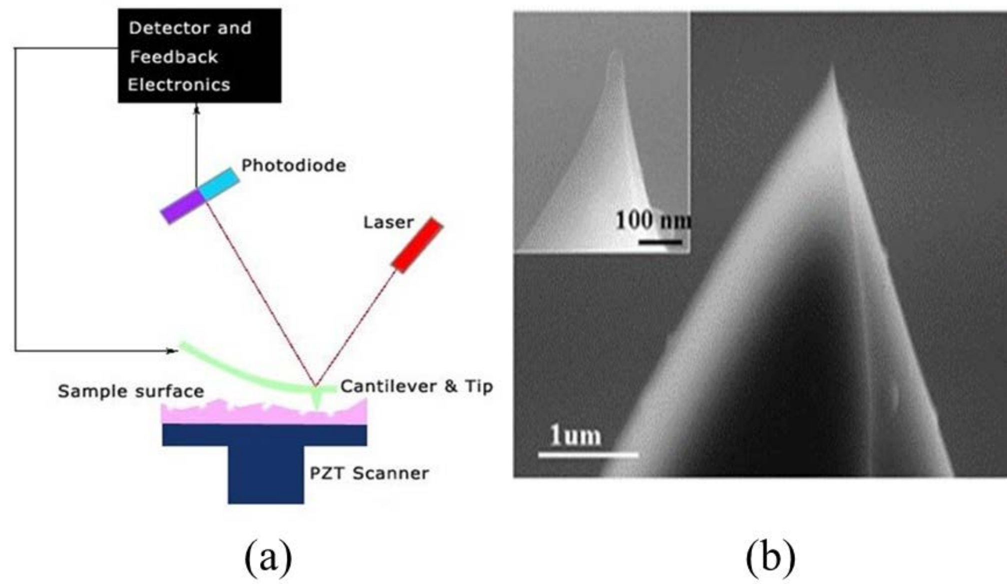

Fig. 3.1: (a) Diagrammatical view of AFM system including PZT (lead zirconium titanate) raster scanner, laser, cantilever with tip and electronic set-up. (b) SEM image of probing tip (a pyramid shape) for surface scanning, inset shows the last thinnest end of the tip. (source [117, 118])

In the current research, a Park XE7 (figure 3.2) and Nanoscope IIIa Dimension 3100 Scanning Probe Microscope (Digital Instruments) was used to examine the surface morphology of the bilayer and single-layer thin films, as well as ZnO 2D nanosheet thickness. All the surface probe measurements were conducted in non-contact tapping mode. For ZnO nanosheet thickness measurement, a mica sheet is used. Two software programs (XEI and NanoScope Analysis) were used for AFM image processing and surface roughness.

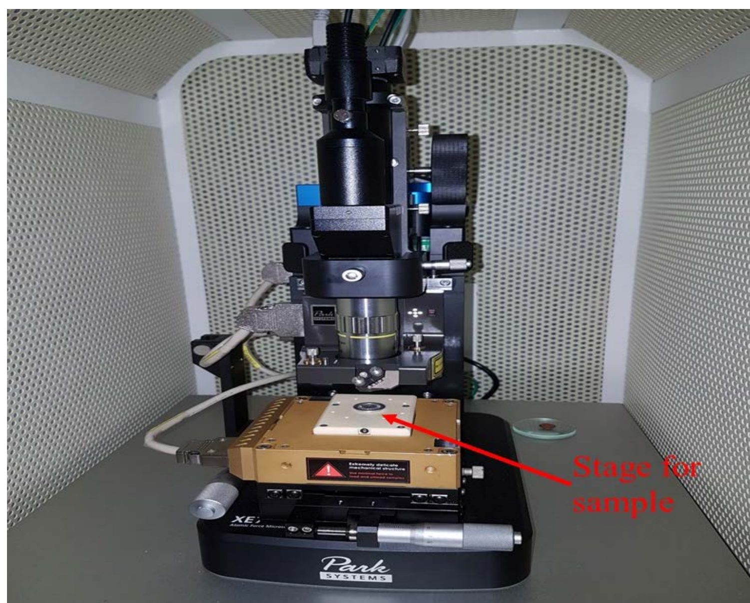

Fig. 3.2: Park XE7 AFM system on vibration free optical table in Microstructural Analysis Unit (MAU) at UTS.

3.1.2. Near-edge X-ray Absorption Fine Structure Spectroscopy

NEXAFS spectroscopy is a powerful analytical tool for the investigation of unoccupied states and their chemical position in a material. The principle mechanism of NEXAFS spectroscopy is depicted in figure 3.3. Soft X-rays (0.1 – 3 keV) are utilised in the NEXAFS probing technique. Here, near-edge means low kinetic energy (0.005 – 0.050 keV) of photoelectrons. Due to the low kinetic energy of photoelectrons, electrons are backscattered several times between the nearby atoms, which results in the improvement of fluorescence emission. In NEXAFS, the core electrons (inner-shell electrons) in the atom of a solid material absorb soft X-rays, resulting in the release of electrons. The released electrons form the inner shell, leaving a hole/vacancy. This vacancy is re-filled by the jumping of other high-energy shell electrons, resulting in two competitive emissions: a photon and an electron emission. The emitted photons and

electrons are called fluorescent photons and auger electrons (AEs), respectively. These two competitive emissions mostly depend on the atomic number of the probing target element. Further, in NEXAFS measurement, the energy of the excited X-ray photons are varied and their corresponding attenuated intensity by the material sample is measured.

In this thesis, the NEXAFS were performed at the Australian Synchrotron in Melbourne using a soft X-ray spectroscopy beamline source. The incident X-ray beam was perpendicular to the film surface. The photon energy scale was calibrated against the Au $4f_{7/2}$ peak at 84 eV from a clean gold film in electrical contact with the sample. There are two types of collection mode: total fluorescence yield (TFY) and total electron yield (TEY). In the TFY mode of NEXAFS, the florescence photon emitted from the target sample was measured, while in the TEY mode, electron emission was measured in the form of electrical current. The TFY mode provides information on the bulk region of the probed sample because of the long mean free path of photons, which is around 50 nm. [119]

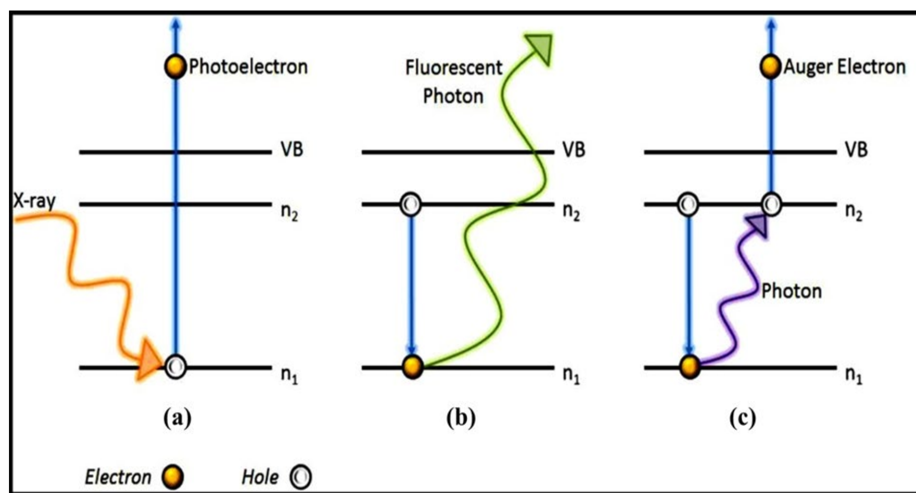

Fig. 3.3: Diagram showing the basic principles of NEXAFS spectroscopy upon incident by soft X-rays: (a) absorption of an X-ray photon resulting in electron emission (photoelectron); (b) fluorescent photon emission; (c) AEs emission (source [119]).

Figure 3.4 depicts a diagrammatical view of the Australian Synchrotron with its required optics and detectors for NEXAFS spectra measurement of N-doped MgZnO sample. The synchrotron storage ring produces electromagnetic radiation. This radiation is then passed through slits, monochromators and various optics to provide a soft X-ray source with the required energy. The soft X-ray beam is then incident on the target sample, which emits TFY and TEY signals in the form of fluorescence photon and electron-based signals.

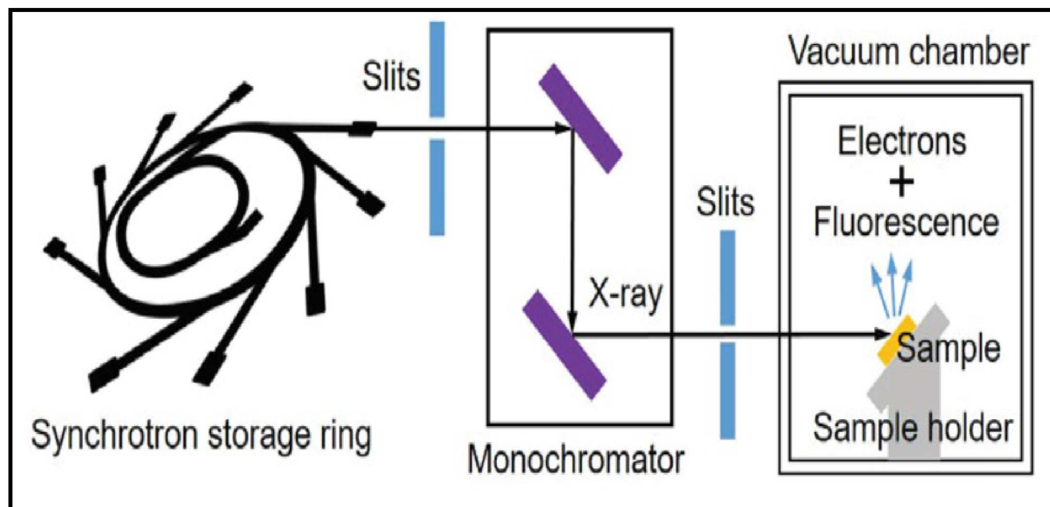

Fig. 3.4: A schematic representation of the NEXAFS system using a soft X-ray source at the Australian Synchrotron, Melbourne (source [120]).

3.1.3. Scanning Electron Microscopy

In SEM, when an energetic beam of electrons (1-30 keV) is incident on the surface of solid materials, generates various emission signals, including backscattered electrons (BSEs), secondary electrons (SEs), AEs, characteristic X-rays and CL signals. The SEs signal has low energy (1 – 3 eV) and provides topographic information, while the BSE signal provides crystal structure information for a solid sample specimen. X-ray signals provide compositional information for the sample and CL provides the electronic structure transition in solid materials. Figure 3.5 shows a schematic view of an electron

beam (e-beam) interaction with a material and their various output electronic and photonic signals. This study used a field emission scanning electron microscopy (FESEM) system (Zeiss Supra 55VP) for surface imaging of MgZnO and ZnO samples.

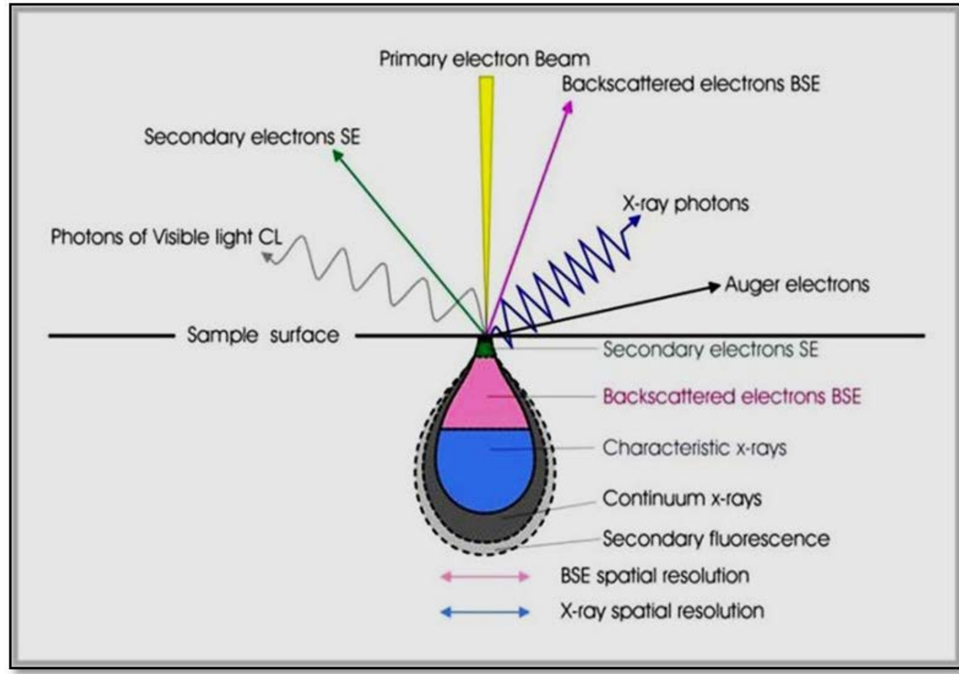

Fig. 3.5: Schematic representation of incident electron beam, different electronic and photonic emitted signals and their interaction penetration volumetric depth.(source [121])

3.1.4. Cathodoluminescence Spectroscopy

CL is a non-destructive spectroscopic technique employed to explore the luminescence and electronic properties of materials. CL optical spectra provide information regarding defects, dopants, impurities, bandgaps and extended defects. In semiconductors, the electrons focused beam absorbed by the materials, excited electrons from valence band to conduction band, leaving holes in the valence band. Once the electrons are excited to the conduction band, they spontaneously recombine with the holes in the valence band and emit an optical signal, which is collected to form a CL spectrum. There are different types of recombination channels. The recombination or light emission

from semiconductor materials is distributed into two categories: extrinsic and intrinsic. In extrinsic-type luminescence, excited electrons recombine with the localised energy states in the bandgap region; when electrons recombine to holes in the valence band this is called an intrinsic-type emission. Within the band gap region, various localised energy levels can exist, may leads to deep-level, DAP, and donors, acceptors bound excitonic emissions.[122] A schematic view of various recombination mechanisms, either excitonic or non-excitonic emissions, are shown in figure 3.6. CL excitation has advantages over PL because of its high penetration depth and high excitation energy, which is especially useful for wide bandgap semiconductors. Another advantage of CL over laser-based excitation is its high spatial resolution—up to the sub-50 nm region, below the light diffraction limit.

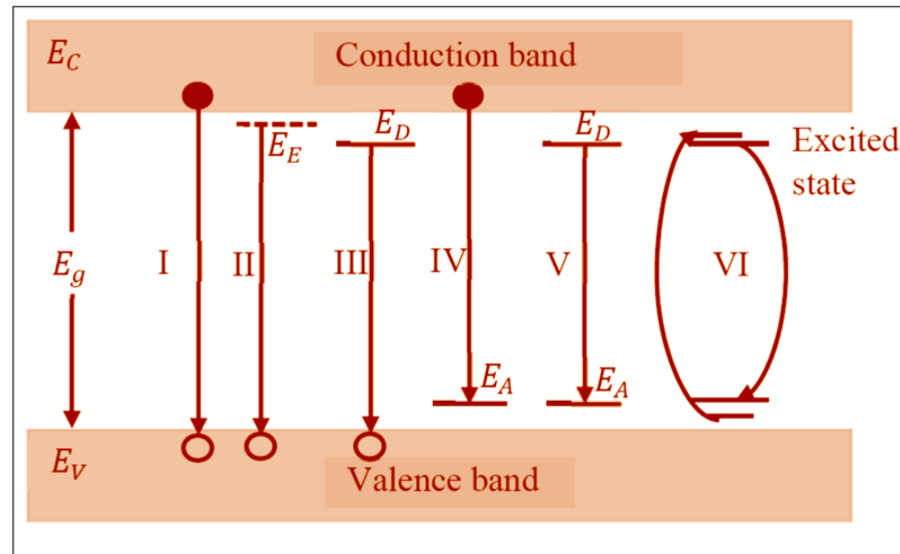

Fig. 3.6: Schematic representation of different transition or recombination pathways by electrons, holes and defect energy levels in semi-conductive materials: (I) optical bandgap emission due to conduction band electrons and valence band hole recombination; (II) free or bound excitonic emission; (III, IV and V) transition due to donor or acceptor states; (VI) the excitation and de-excitation pathway of incomplete inner-shell impurities.(source [122])

In this study, an FEI Quanta 200 ESEM system was used for the CL experimental analysis. The whole CL system has four major parts: ESEM, parabolic mirror, spectrometer and monochromators. A small hole of 30-micron diameter in the parabolic mirror centre passes the electron beam to hit the sample for excitation. The e-beam has accelerating voltages ranging from 0.5 to 30.0 kV. The optical emission from the sample is received by the parabolic mirror, which directs it to the spectrophotometer via optics and fibres. A Hamamatsu S7011-1007 charge-coupled device (CCD) sensor (three different grating) in a Hamamatsu C7021 detector head with an active area of 1,044 × 124 pixels was employed for high-resolution CL spectral analysis. In the CL analysis of ZnO/MgZnO MQWs, grating 1 was used with a wavelength range of 50 nm. A photomultiplier as also connected to the CL system for optic alignment and to achieve maximum signal. The CL spectra at various temperatures were collected using three types of stage and a temperature controller. For the liquid N temperature range (80 – 300 K), the Gatan C1002 cold stage was used, while Gatan CF302 can be used for the liquid helium temperature range (10 – 80 K). Another hot stage can be used for temperature up to 600 K. Figure 3.7 depicts a schematic view of the CL spectroscopic system. The PL system had the same set-up except the incident beam source was a laser instead of an e-beam. In the case of a ZnO nanosheet, a copper TEM grid was used for the CL probing analysis in transmission mode. Nanosheets are atomically thin and have very small bulk regions for electron hole pair generation. Therefore, a high accelerating voltage of ~ 30 kV and low e-beam current was used for CL spectra from the ZnO nanosheets, to achieve maximum CL intensity and small spot size of e-beam.

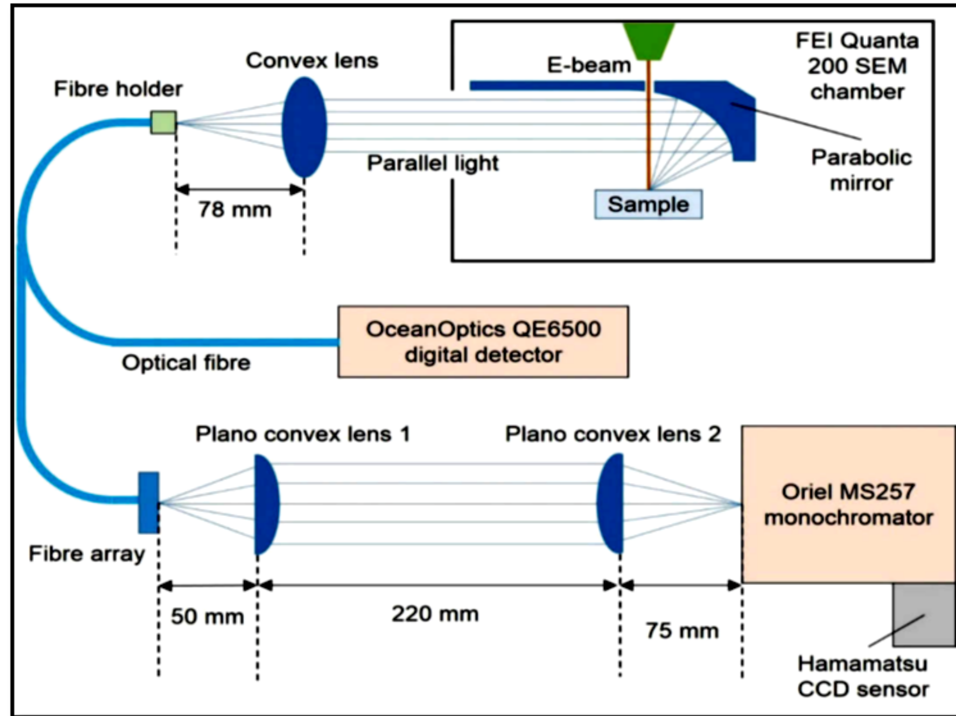

Fig. 3.7: CL spectroscopic system in a schematic form including different optics, optical fibres, detector and SEM chamber.(source [120])

3.1.4.1. Cathodoluminescence Spectrum Correction and Calibration

CL intensity correction is necessary in CL spectral analysis to account for the wavelength-dependent response of each optical component in the light collection system. An Oriel 63358 45 W quartz tungsten halogen (QTH) lamp with a known emission intensity versus wavelength spectrum was used for the correction of total response of the CL collection system. The National Institute of Standards and Technology (NIST) in the USA was conducted the Oriel lamp intensity versus wavelength measurement. The following relationship was used to correct the intensity of the CL spectral data:

$$\text{Corrected data} = \text{correction curve} \times \text{measured data} \qquad (3.1)$$

Furthermore, equation 3.2 was used to convert the CL intensity from wavelength to energy space:

$$I\ (eV) = \lambda^2 I\ (nm) \tag{3.2}$$

By using a Hamamatsu CCD spectrophotometer to obtain high-resolution luminescence spectra, one can measure luminescence intensity versus pixel positions across the CCD arrays. To convert the pixel position to wavelength scale, spectral database lines (Table 3.1) were used from a mercury (Hg) lamp, calibrated by NIST.[123] The two graphs in figure 3.8 displays the conversion from pixel to wavelength scale, which is stated and defined by the following relationship:

$$Wavelength\ (\lambda) = slope\ \times pixel + intercept \tag{3.3}$$

Using this linear fitting equation, the wavelength scale range corresponding to the pixel range can be derived. The following relationship was used to convert CL/PL wavelength spectra to their corresponding energy spectra:

$$Energy\ (eV) = {}^{1239.8418}/_{\lambda\ (nm)} \tag{3.4}$$

CL spectroscopy was investigated by varying three parameters: e-beam energy, e-beam power and sample temperature, while no facility was available for laser beam energy (wavelength) variation in PL spectroscopy measurements. These are discussed in detail in the next sections.

Table 3.1: NIST atomic spectra database used for pixel conversion calculation.(source [123])

Ion	Observed wavelength vacuum (nm)	Ritz wavelength vacuum (nm)	Relative intensity
Hg I	365.01580	365.01579	9000
Hg I	365.48420	365.48429	3000
Hg I	366.32840	366.32831	2000

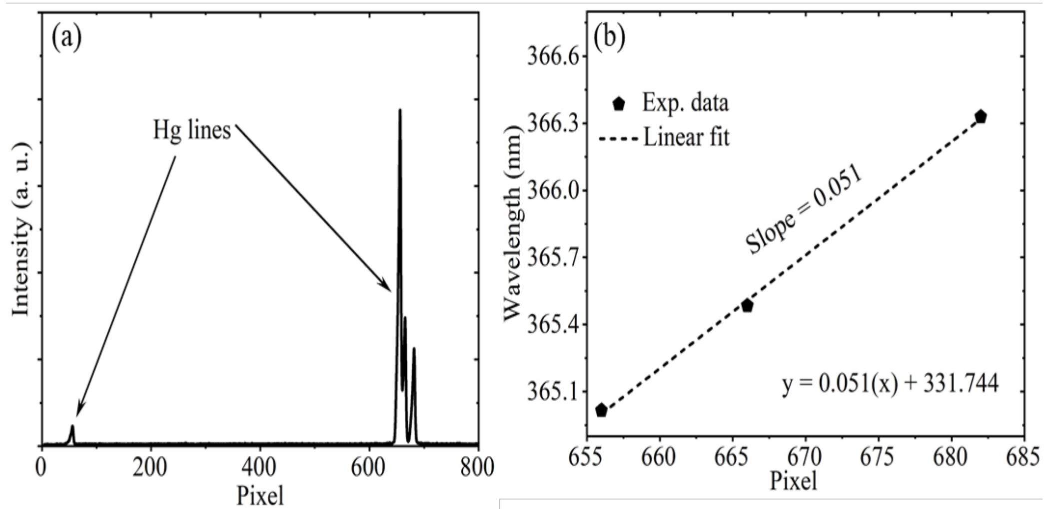

Fig. 3.8: (a) Intensity of CL versus pixels for an Hg lamp with central wavelength fixed at 360 nm by Hamamatsu CCD. (b) Linear fitting of the Hg spectral line taken from the NIST database and plotted against pixels. The corresponding linear equation with slope (0.051 nm) and intercept (331.744 nm) is shown inside graph b.

3.1.4.2. CASINO Simulation of Electron Energy Loss in MgZnO/ZnO MQWs

The Monte Carlo CASINO simulation program can be used for CL generation and penetration depth analysis by modelling the in-depth and in-plane profiles of the electron energy loss within the sample.[124] The penetration and spread of energetic e-beams is strongly dependent on the accelerating voltage as well as the average atomic number and density of the sample. Since the electron energy loss is directly related to the electron-hole pair density, the Monte Carlo simulation results can be used to estimate the spatial distribution of the CL generation. Alternatively, different mathematical models, including those of Everhart and Hoff, Gruen, Kanaya and Okayama, can be used to determine the penetration depth of CL generation. [122, 125]

The most common method used to determine the maximum CL generation depth (D_{CL}), is the Kanaya and Okayama model, which is typically used to calculate the electron range:

$$D_{CL} = R_e = {}^{0.0276 \times A}\big/_{\rho Z^{0.889}}\ E^{1.67}\ (\mu m) \tag{3.5}$$

where ρ is the density of the material or sample, A is the atomic number, Z is atomic weight and E is the e-beam energy, in keV. As mentioned above, the volumetric shape of the CL generation in a material strongly depends on the average atomic number of the sample. For low atomic number materials, a tear-drop volumetric shape is observed, while for high atomic number, a hemisphere is observed. The following expression is used for the calculation of generated electron-hole pairs: [122]

$$G = {}^{E(1-\gamma)}\big/_{E_f} \tag{3.6}$$

where G is the generation factor, γ is the part of energy loss owing to the backscattered electrons and E_f is the electron hole pair generation formation energy. E_f is related to the band gap (E_g) of the material, and can be found using the following relationship:

$$E_f = 2.8\, E_g + E^* \tag{3.7}$$

Where E^* is in the range $0.5 < E^* < 1.0$ eV and is sample dependent. For MgZnO/ZnO MQWs, the CASINO Monte Carlo simulated results at 2 keV e-beam energy are shown in figure 3.9. The atomic fractions of Mg, Zn and O were taken as 7.5, 42.5 and 50, while the complete MQWs depth CL simulation was carried out over the range of 1–7 keV e-beam energy.

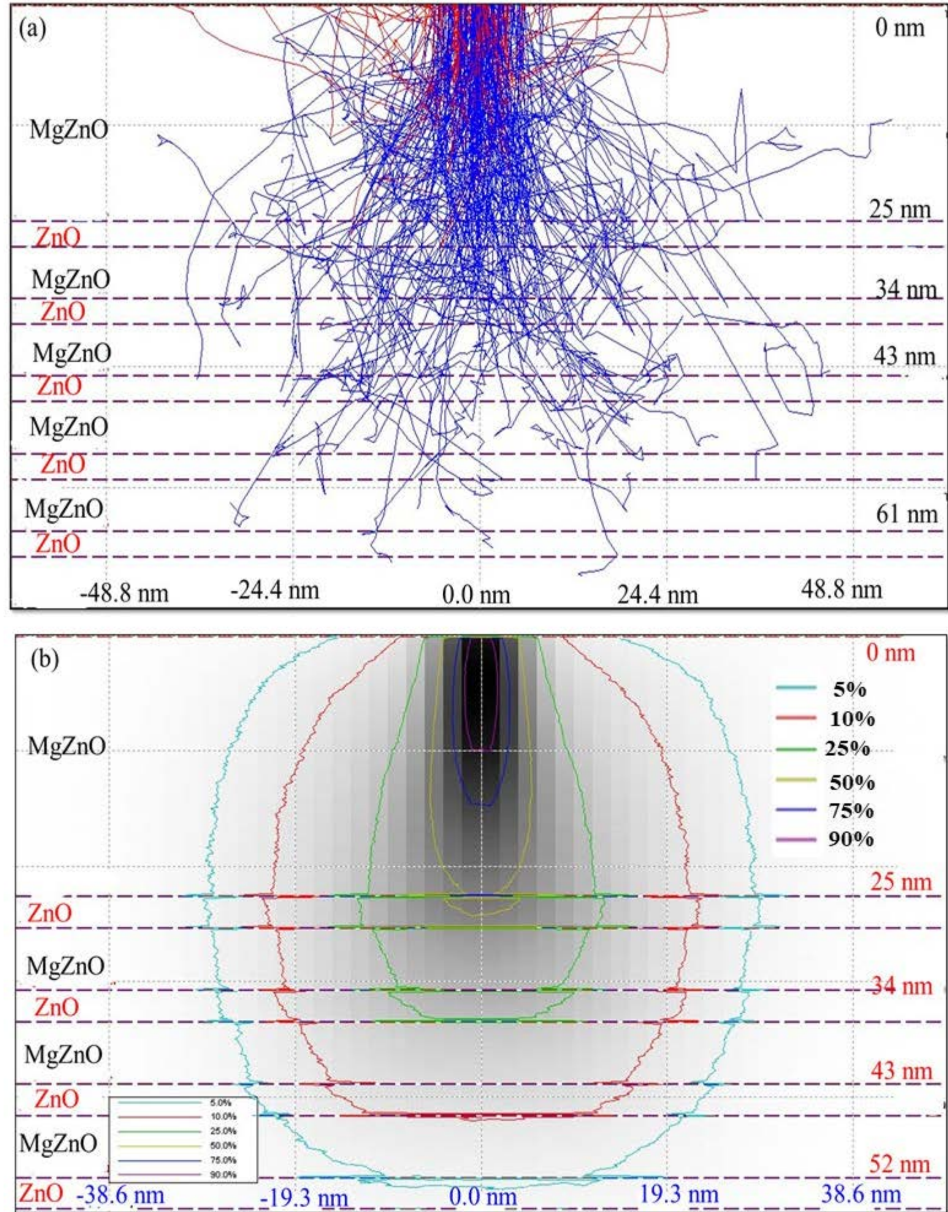

Fig. 3.9: CASINO simulation of electron beam interaction in MgZnO/ZnO MQWs structure at 2 keV e-beam energy: (a) electrons trajectory path lines are shown in red for backscattered electrons and blue for primary electrons; (b) cross-section of the electron energy loss at 2 kV showing the spatial distribution of electron-hole pairs.

3.1.5. Photoluminescence Spectroscopy

PL spectroscopy is a non-destructive, surface-sensitive and contactless probing technique for diagnosing electronic structure of semiconductor materials. In PL, a laser beam hits the target material, the material absorbs light energy ($h\nu$) and the electrons are excited to an upper energy state, so-called photo-excitation. For photo-excitation, the energy of the laser excitation source (E_{ex}) is generally greater than the bandgap energy (E_{gap}) of the target semiconductor. PL spectral analysis provides a detailed description of electronic structure, binding energy and defect origins near the surface region. Although, the CL and PL relaxation processes are similar, but there are significant differences between the two techniques. First, CL can produce hundreds of electron-hole pairs by each individual incident electron, and strongly depends on e-beam energy and material. On the other hand, only one electron-hole pair can generate by each photon in PL laser excitation. Second, since the PL energy loss profile decreases exponentially from the surface following Beer's law (equation 3.9), the PL signal is always maximised at the surface whereas in CL the probing depth increases with increasing kV. Third, although there is no major issue relating to the specimen charging in PL probing of poorly electrically conductive materials, there can be strong charging effects with e-beam excitation in CL. This study used a He–Cd laser source with two wavelengths—325 (UV) and 442 nm (blue), and a separate laser source with a 532-nm solid-state green laser. The power of the laser was varied by using neutral density filters for power-dependent PL analysis. Both laser and e-beam can also be used simultaneously incident on the sample, to achieve strong optical emissions.

3.1.6. Depth-resolved CL

Depth-resolved CL analysis was carried out by increasing the e-beam accelerating voltage to systematically increase the probing depth. The rate of electron hole pair generation was kept constant by adjusting the e-beam current to maintain a constant electron beam power;

$$P = V_b I_b \tag{3.8}$$

where P is the e-beam power at accelerating voltage (V_b) and e-beam current (I_b). The depth-resolved CL technique is used to characterise the surface, near surface and bulk optical properties of a material. At high accelerating voltage, self-absorption of the NBE emission occurs because of the increasing escape depth of the CL signal. The absorption intensity is expressed by the Beer–Lambert relationship:

$$I_\lambda = I_o e^{-\propto\lambda D} \tag{3.9}$$

where I is intensity, D is electron-hole generation depth and $\boldsymbol{\alpha}$ is the absorption coefficient of the target specimen, which is dependent on the wavelength. Since shorter CL NBE wavelengths are absorbed more strongly than longer wavelength emission, a red energy shift of the CL emission peak position is observed with increasing kV. The depth-resolved CL analysis was used for the MgZnO/ZnO MQWs samples.

3.1.7. Temperature-resolved CL and PL

Temperature-resolved CL/PL measurement is a powerful technique for investigating the origin of excitons, optical bandgaps and defect-related luminescence in semiconductor materials. The CL system used in this work has a temperature analysis range from 5 to 600 K. Below 80 K, liquid helium is used, while liquid N is used for the 80–300 K range with two different thermal controllers and stages. The range of temperatures used in this study was 80–300 K.

Generally, the luminescence (CL or PL) emission peak broadens with increasing temperature and narrows with decreasing temperature. This is due to electron–phonon interactions, which are enhanced at higher temperatures. With an increase in sample temperature, thermal shrinkage in band gap occurs, which results in redshifting of free exciton and a NBE and donor-bound exciton peak. There is competition between bound excitons and free exciton radiative recombination during temperature-dependent CL/or PL measurement. Bound excitons have higher intensity at lower temperature range, typically below 100 K, while free exciton emission peak intensity is enhanced in the high-temperature range, typically above 100 K. Further, from temperature-resolved CL/PL analysis, the activation energy for excitonic or non-excitonic recombination can be determined using the following exponential Arrhenius relationship:

$$I/I_o = 1/1 + C\ e^{E/KT} \tag{3.10}$$

In equation 3.10, I is the intensity at temperature T, I_o is the intensity at the lowest temperature at a given measurement, C is a constant, E is the activation energy and K is the Boltzmann constant.

3.1.8. Power-dependent CL and PL

CL or PL measurements based on power variation were conducted to investigate the kinetics of recombination channels with respect to beam power. In power-dependent CL or PL spectroscopy, the accelerating voltage/laser beam energy (wavelength) remained constant, while the e-beam current/ or laser power was altered. The integral intensity of luminescence peaks was determined by Gaussian fitting using the OriginLab software.

Mathematically, the following relationship expresses the relationship between the integral intensity of an emission peak and the incident beam power: [126]

$$I \propto P^{m} \tag{3.11}$$

where *I* is the integral intensity of the CL/PL peak and P is the e-beam/or laser beam power. The exponent m is found by linear fitting of logarithmic intensity (I) and logarithmic power (P) on the *y*- and *x*-axis. The slope *m* from logarithmic linear plotting provides information on the nature of the recombination channels. For a sub-linear ($m < 1$) power-law exponent, the luminescence peak emission is from lattice coupled deep level defects with slow relaxation times. While a linear ($m = 1$) and super-linear ($m > 1$) exponent is characteristic of bound or free exciton emission due to their fast decay rates.

3.2. Synthesis and Fabrication of the Samples in this Thesis

Majority of the samples were fabricated using the PLD technique at moderate temperature growth (typically ~600ºC). Two different source targets were used for MgZnO and ZnO film deposition on a c-plane sapphire substrate. A ZnO source was used for buffer layer deposition on a sapphire substrate to minimise the effect of mismatching lattice parameters with the top MgZnO layer. The highly pure ZnO and MgZnO (4 wt% Mg) commercial sintered target was evaporated under three ambient conditions: molecular nitrogen (N_2), molecular oxygen (O_2) and vacuum. The PLD system used for the (ZnO, MgZnO) sample deposition was the Coherent LPX 100 KrF excimer laser source with 248 nm wavelength. The pulse repetition rate was varied in the range of 1–50 Hz during film deposition. The laser fluence used with the high purity target material was up to ~4 J/cm^2. During film growth, highly pure molecular oxygen (O_2) was utilised

within the chamber in the pressure range 10^{-6}–10^{-3} Torr. All samples (except MQWs and ZnO 2D nanosheets) were fabricated in Nanovation, France. [127, 128] Details of the thin film samples are summarised in Table 3.2. The MQWs samples were fabricated using the molecular beam epitaxy (MBE) technique on a-sapphire substrate. There were 12 periods of MgZnO (6 nm)/ZnO (3 nm) on a buffer layer 75 nm thick. The capping or final layer of the MQW structure was MgZnO (Mg is 15 at%) with a thickness of 25 nm. The ZnO 2D nanosheets were fabricated via the multistep soft-chemical exfoliation technique. The 2D nanosheet suspensions were centrifuged at different rotation speeds to separate thin from thick nanosheets. CL probing of a single nanosheet was performed using a carbon-coated copper TEM grid, by taking a small amount of nanosheet suspension from the top of the bottle using a micropipette and then drop-casted it on the TEM grid. At the same time, the sample in the micropipette was drop-casted on an electronic-grade mica sheet for AFM analysis.

Table 3.2: Various samples with their corresponding thickness and other information.

Sample name	Thickness (nm)	Fabrication technique	Comments
ZnO/c-sapphire	145	PLD	Commercial target
MgZnO:O_2/c-sapphire	95	PLD	Oxygen (O_2) ambient
MgZnO:N_2/c-sapphire	180	PLD	Nitrogen (N_2) Ambient
MgZnO:vac/c-sapphire	80	PLD	Vacuum Ambient
MgZnO:O_2/ZnO/c-sapphire	240	PLD	Oxygen (O_2) ambient
MgZnO:N_2/ZnO/c-sapphire	325	PLD	Nitrogen (N_2) Ambient
MgZnO:vac/ZnO/c-sapphire	225	PLD	Vacuum Ambient
ZnO/bulk ZnO (A, M, C-plane)	430	PLD	ZnO on single crystal ZnO substrate with three different planes
MgZnO/ZnO/bulk ZnO A-plane	450	PLD	A-plane crystal orientation
MgZnO/ZnO/bulk ZnO C-plane	450	PLD	C-plane crystal orientation
MgZnO/ZnO/bulk ZnO M-plane	450	PLD	M-plane crystal orientation
MgZnO(6 nm)/ZnO(3 nm) /c-sapphire	208 nm	MBE	12 periods of MgZnO/ZnO on buffer layer of 75 nm ZnO and capping layer of 25 nm thickness
ZnO 2D nanosheet	1.1, 2.5, 5, 8 nm	Chemical Exfoliation	Centrifugation with different rotation speed, 500, 5,000, 12,000 and 18,000 g

Chapter 4

4. Hydrogenation of MgZnO/ZnO Multiple Quantum Wells

In this chapter, a detail analysis of hydrogen (H) doping effect on the luminescence properties of MgZnO/ZnO MQWs. The MQWs structures were grown epitaxially and subsequently post-annealed in a H remote plasma environment, so-called rapid remote plasma annealing (RRPA). A comprehensive CL studies reveal that following the H plasma treatment, the optical emission from the MQWs increases by over 10 times depending on the plasma time and temperature. Another important finding of this study is the complete quenching of defect-related optical emissions. RRPA presents a facile and effective approach to enhance the optical quality of oxide-based MQWs structures and could open the new door to the potential development of high-efficiency optoelectronic devices.

4.1. Introduction

There has been significant interest in developing high-efficiency optoelectronic and photonic devices based on ZnO owing to its high exciton binding energy, radiation hardness and ease of fabrication. [1, 129-131] ZnO-based MQWs receive much attention in optical device development applications because their emission wavelength peak can be finely tuned for particular purposes by adjusting structural parameters.[132] Currently, the development of cutting-edge growth techniques allows for the precise control of a thin film uniformity, stoichiometry and thickness, enabling numerous emerging technological applications. However, the optical emission efficiency of oxide and nitride-

based heterostructure devices such as MQWs, is limited by the presence of extended defects and competitive carrier recombination channels, which lead to non-radiative areas and reduced the lifetime for devices. These additional carrier relaxation pathways occur through impurities as well as extended defects, interface lattice parameters mismatching, well-width fluctuations and alloy inhomogeneity. [133-137] To eradicate these unwanted recombination channels and enhance the MQW optical emission, different procedure have been adopted to the ZnO-based MQWs, such as high-temperature thermal annealing or hydrogenation. [138, 139] On the basis of high chemical reactivity of H, it has been shown that H strongly changes the optical and electrical properties of ZnO, as it readily interacts with and passivates various defect centres and dangling bonds at extended as well as periodic crystal structural defects. [139, 140] Although, H plasma treatment has been used to enhance the optical emission in InGaAs/AlGaAs, InGaN/GaN and CdZnO/ZnO MQWs, [135, 139, 141], there is no report on the effects of H plasma treatment on MgZnO/ZnO MQWs. The focus of this study is to evaluate and characterise the effects of H doping on the luminescence properties of MgZnO/ZnO MQWs and to open the new opportunities for ZnO-based MQWs based applications.

It have already been proved from optical analysis that the NBE emission in ZnO material (bulk and nanostructured) can be considerably increased through the incorporation of atomic H.[142-144] This increase in the NBE emission has been attributed to a high diffusivity of H in ZnO, which enables the formation of H shallow donors. The incorporation of H, leads to rise of an additional radiative NBE recombination channel at low temperatures as well as passivation of competitive recombination channels responsible for deep-level emissions. [140, 143] Furthermore, H has been reported to make a stable complex consisting of zinc vacancy (V_{Zn}) and two H atoms, resulting the suppression of green luminescence (GL) peak at 540 nm wavelength.

[145] This research work relates with the doping of H atoms into MgZnO/ZnO MQWs by RRPA at low temperature (200ºC). The MQWs structure consists of 12 periods of ZnO (3 nm) / MgZnO (6 nm), were grown on a 75 nm ZnO buffer layer and capped with MgZnO barrier layer of 25 nm thickness. A summary of all MQWs samples along with post-processing parameters are shown in Table 4.1. The Mg concentration in the MgZnO barrier is ~ 15 at.%. The effect of H incorporation has been investigated using systematic CL microanalysis. The RRPA post-growth treatment have potential advantage over higher temperature traditional thermal annealing is due to its ability to enhance the desired optical emission of MQWs while preserve their crystal structure integrity. Previous reports on the effects of H incorporation into MQWs of InGaN and ZnCdO active layers have shown a significant enhancement on the PL intensity in MQWs. [139, 141] Herein, comprehensive characterisation of MgZnO/ZnO MQWs was carried out by employing temperature-, power density- and depth-dependent CL measurements and analysis.

Table 4.1: Summary of six treated MQWs samples. All RRPA-treated MQWs had the same conditions of H plasma with 150 W power and 0.1 mbar H pressure.

MQWs	Temperature (ºC)	Plasma H timing	Argon gas timing
Pristine MQWs	200	0	30 min
H:MQWs	200	20 sec	0
H:MQWs	200	40 sec	0
H:MQWs	200	90 sec	0
H:MQWs	200	5 min	0
H:MQWs	200	10 min	0

4.2. Morphological Properties

The cross-sectional TEM image view of the MQWs structure shown in figure 4.1. The regular periodic thin film layer structure of ZnO well region and MgZnO barrier region are flat and abrupt. The corresponding energy-dispersive X-ray (EDX) mapping of Mg, Al and Zn spatial distribution are shown in figure 4.2. Both EDX and TEM analysis results that the MQWs structure are of high epitaxial quality with no impurity detection. The post-growth RRPA treatment has no effect on the MQWs interfaces because of the low temperature using during the H treatment.

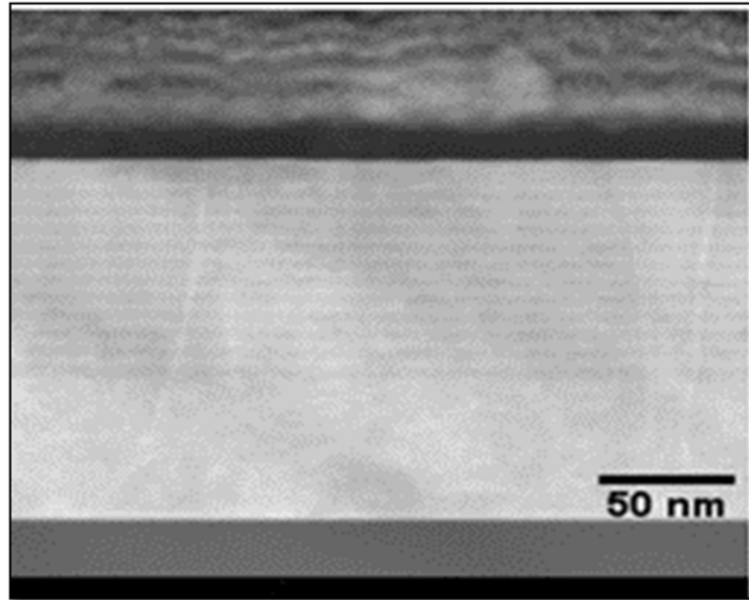

Fig. 4.1: TEM cross-sectional image of a MgZnO/ZnO MQWs structure with grey and blackish colours showing the periodic layers of ZnO and MgZnO, respectively.

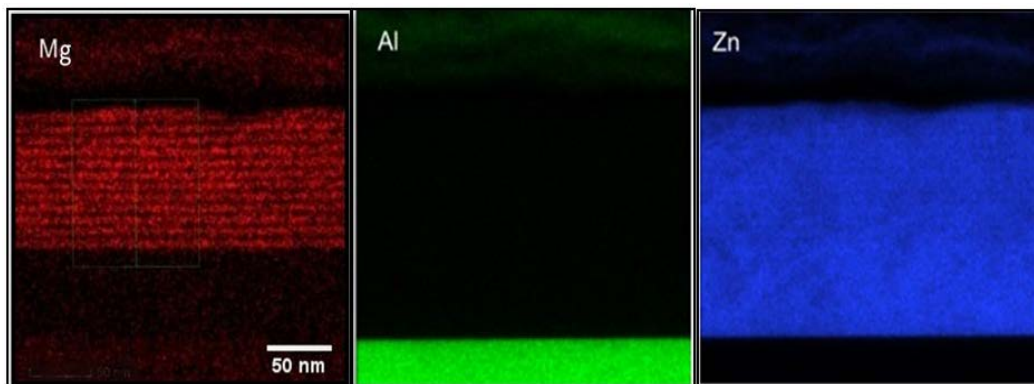

Fig. 4.2: Energy-dispersive X-ray mapping with spatial distribution of Mg, Al and Zn elements in a pristine MgZnO/ZnO MQWs . A layer distribution is shown for Mg but Zn shows a continuum region due to the presence of Zn in both MgZnO and ZnO layer. Al is only shown in sapphire substrate (Al_2O_3).

AFM images of surface morphology shown in figure 4.3 for pristine, short time (40 sec) and long-time (10 min) H plasma treatment samples. These AFM images reveals

that surface degradation has happened due to prolong time plasma treatment and induced near-surface defects. These surface defects act as a competitive recombination channels and reduced the MQWs optical emission. The production of competitive recombination channels will be discussed in detail in the next part of chapter.

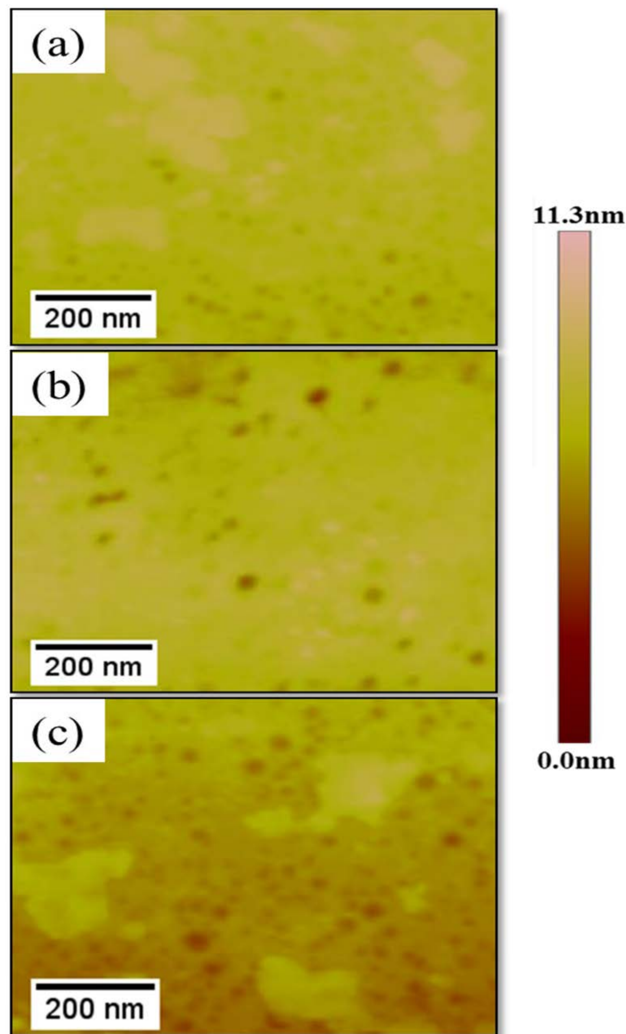

Fig. 4.3: AFM images: (a) pristine MQWs and H-doped MQWs after H plasma treatment for (b) 40 seconds and (c) 10 minutes. Surface degradation become clear after 10 min of plasma treatment. These surface defects act as competitive recombination channels, reducing the MQW optical emission.

4.3. Cathodoluminescence Properties

The luminescence properties of MgZnO/ZnO MQWs were thoroughly analysed by CL spectroscopic techniques. Various CL techniques, such as power-resolved CL, temperature-resolved CL and depth-resolved CL approaches have been studied in the following section.

4.3.1. Enhancement of MQWs Emission by Hydrogen Incorporation

In-depth CL microanalysis has been carried out to study the optical properties of pristine MQWs and H-doped MQWs samples. Fig. 4.5(a) shows a typical CL spectrum is measured at 80 K for the MQWs samples, which was annealed in H remote plasma at 200ºC (denoted H:MQWs) and in Ar gas at the same temperature for 30 min (denoted pristine MQWs). As H is known to exhibit a high diffusivity of 0.2 cm^2/s in ZnO, so it can diffuse to micron depth in the sample at 200ºC. Accordingly, H can easily migrate through the entire MQWs structure to the ZnO buffer layer.[23, 58] Several types of radiative transitions can be clearly distinguished in figure 4.5(a): band-edge emission from the MQW at 3.423 eV, basal stacking fault (BSF) emission at 3.389 eV and the NBE emission from the ZnO buffer layer at 3.367 eV. [146-148] Power-resolved and depth-resolved CL (later in this chapter) analysis further proves that the MQW and NBE emission of pristine and RRPA-treated MQWs are excitonic by nature and not related to lattice-coupled defect. The separation of ~34 meV between the MQW and BSF emission is consistent with embedded zinc-blende structure within the wurtzite structure in MQWs, as reported elsewhere.[147] In addition to the NBE emission, the MQWs structure display a GL band at 2.3 eV (inset of Fig. 4.5b), corresponds to V_{Zn} defects in the ZnO

material.[140] Upon the H plasma treatment, the MQW emission rapidly increases with the H plasma time, reaching its maximum intensity (~10 times of pristine MQWs) after a 40 sec exposure time. The overall enhancement factor for all RRPA-treated MQWs are summarised in Table 4.2. Conversely, both the GL and BSF peak are completely quenched after H incorporation. The complete elimination of the GL (inset of figure 4.5b) is entirely consistent with the passivation of V_{Zn} by H atoms. [140] Previous studies on BSF-related luminescence have shown that the BSF emission could be ascribed as an acceptor-like free-to-bound transition, though the exact nature of the acceptor is unknown. [149] Such acceptor would interact strongly with H^+ donors, leading to the complete suppression of BSF emission by the RRPA treatment. The emergence of the NBE ZnO emission at 3.367 eV, due to H donor-bound excitons in bulk ZnO, confirms that H is incorporated into all the MQWs and the buffer layer after the plasma anneal. At 2 kV accelerating voltage, the electron-hole pair generation depth by the e-beam is around 60 nm in MQWs. This penetration depth of e-beam is far away from the ZnO buffer layer, and so no chance of e-beam carriers to reach to buffer layer for excitation. In this way, the ZnO NBE emission is related to the buffer layer, which is excited by the forward generated MQW CL optical emission. This reabsorption process of CL within the MQWs structure leads the two optical emission (MQW and ZnO NBE) to be vary in proportion to each other. Fig. 4.5b shows the integrated MQW emission versus H plasma time, revealing a rapid rise in intensity followed by a relatively slower decline after reaching a maximum at an exposure time of 40 seconds. The integral intensity was determined for all samples by Gaussian fitting, as shown in figure 4.4. Accordingly, the observed reduction in the MQW emission with longer H plasma exposure time is attributed to a surface degradation effect (see the AFM images of the MQWs sample surface before and after the plasma treatment in Fig. 4.3). The formation of near-surface structural defects in

prolonged plasma treatments lowers the MQW intensity as they act as competitive recombination channels. These surface competitive recombination channels are increased with RRPA treatment time, while all other parameters are kept constant. The surface recombination velocity is increased with the increasing of defects on the surface. This means that the flow of carriers from the bulk to the surface region increased due the depletion region created by higher defects on the surface. Therefore, the recombination velocity increases and luminescence of MQWs emission decreases with the increasing of RRPA treatment time of H. [150]

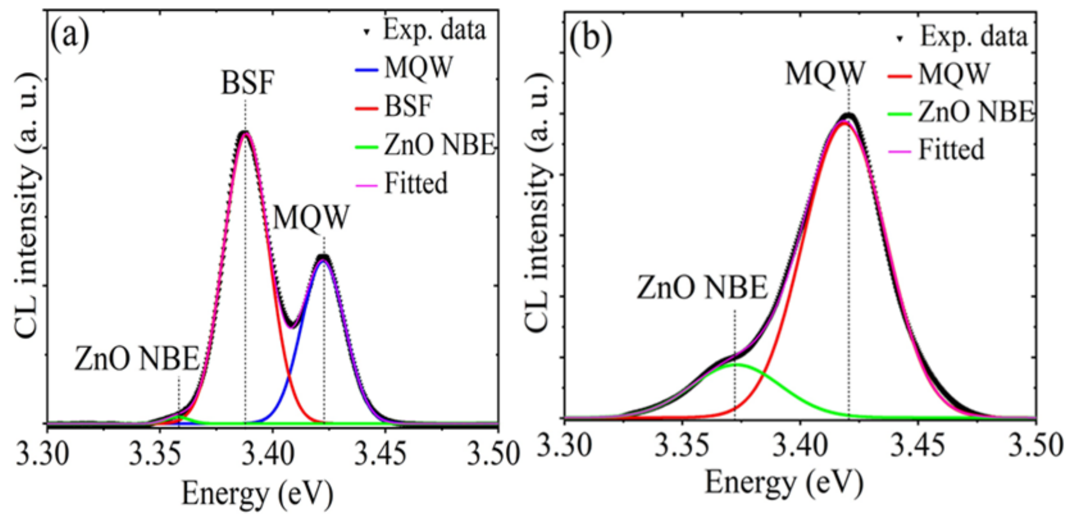

Fig. 4.4: Fitted CL spectra of (a) pristine and (b) H-doped MQWs for extraction of integral intensity by using Gaussian function.

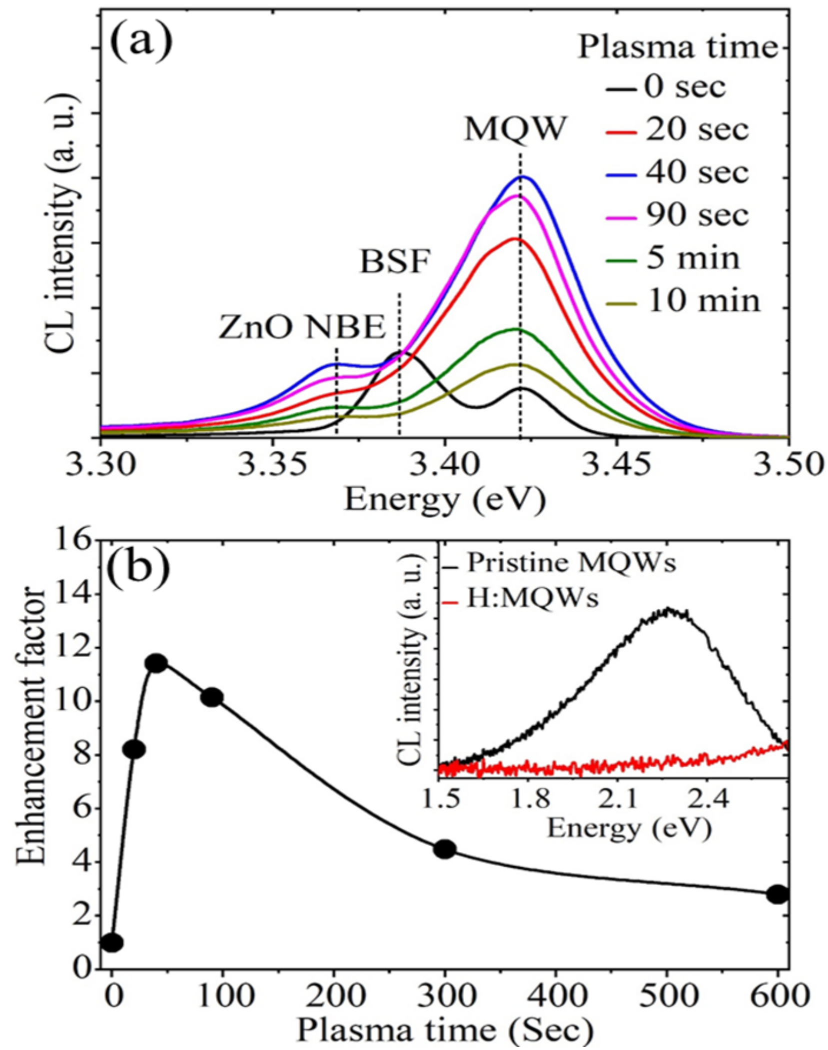

Fig. 4.5: (a) CL spectra of pristine and RRPA-treated MgZnO/ZnO MQWs (V_B = 2 kV, I_B = 3.8 nA, T = 80 K), showing a significant increase in the MQW emission peak and complete quenching of the BSF emission peak following the incorporation of H. (b) Enhancement factor of the MQW peak as a function of plasma time for the same acceleration voltage (2 kV), showing a rapid rise in MQW emissions followed by a slow decline after reaching a maximum after 40 sec of plasma treatment. The decrease in MQW emissions after prolonged plasma treatment is due to surface degradation as discussed in AFM results. The inset of Fig. 4.5(b) shows defect-related green emission at 2.3 eV from the pristine MQW being completely quenched after RRPA treatment.

Table 4.2: All values of integral, peak intensity of pristine and RRPA-treated samples and their corresponding enhancement factor for integral intensity and peak intensity ratio. Enhancement factor is defined as the ratio of H-doped and pristine MQWs CL emission peak.

RRPA-treated time	**Peak intensity (I_o)**	**Integral intensity (I)**	**Enhancement factor (peak intensity ratio)**	**Enhancement factor (integral intensity ratio)**
0 sec (pristine sample)	37959	758	1	1
20 sec	153444	6225	4.0	8.2
40 sec	200523	8654	5.3	11.4
90 sec	186799	7698	4.9	10.1
5 min	83534	3394	2.2	4.5
10 min	56284	2123	1.5	2.8

4.3.2. Thermal Stability of RRPA MQWs Emission

Not only is MQW emission enhanced by H doping but the results also indicate that the RRPA-treated sample are also highly thermally stable. The enhanced luminescence in the RRPA-treated MQWs persists for over six months in ambient condition and was almost unaffected after annealing at 300 and 400 ºC for one hour as shown in figure 4.6 (a), indicating their high thermal stability. The high thermal stability of the RRPA-treated MQWs, compared with H-doped ZnO bulk, suggests that H radicals incorporated into the MQWs structure by the RRPA are mainly trapped at defect sites (such as V_{Zn} and BSFs), which possess a much higher diffusion activation energy than interstitial sites. Figure 4.6(b) shows that the H plasma treatment (RRPA) of MQWs are far better than simple annealing in ambient H_2. This shows that H_2 molecules adsorbed onto the barrier surface and almost no diffusion occurred in the MQWs structure. The results indicate that the low-temperature RRPA method is far superior than high-temperature annealing in H_2, presumably because of the high reactivity of ZnO to H radicals produced by the remote plasma technique.

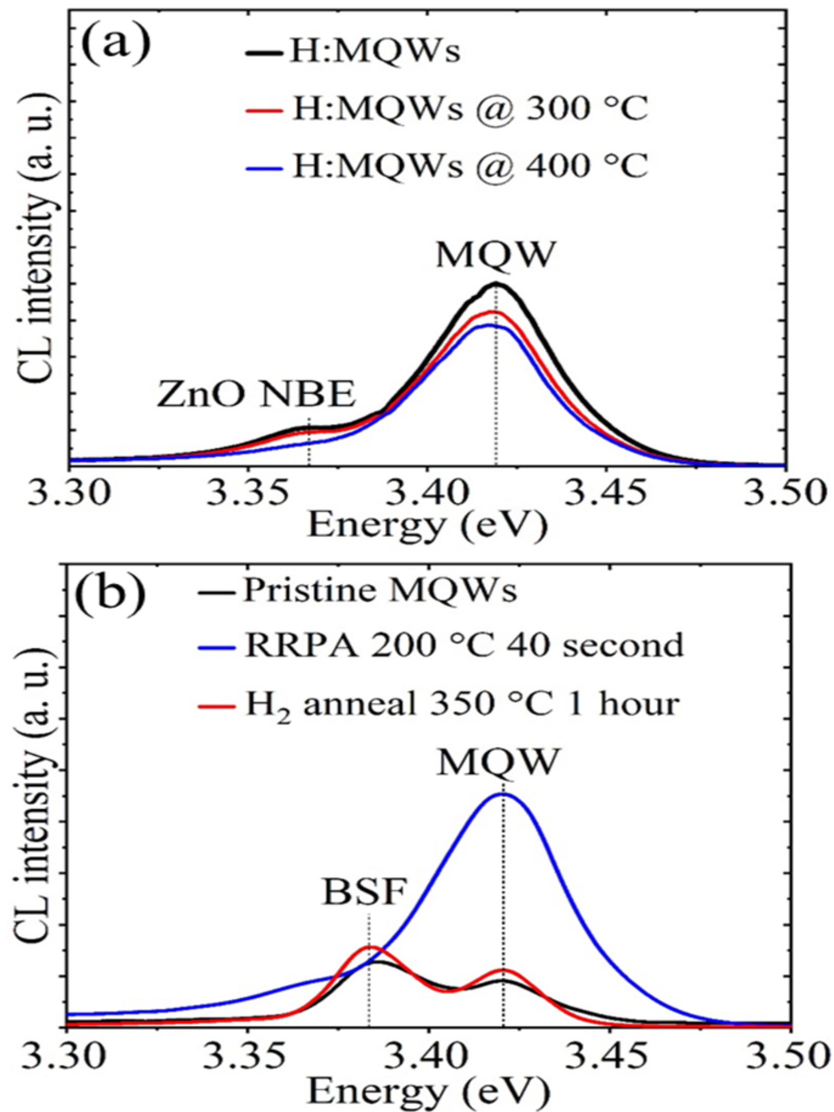

Fig. 4.6: (a) CL spectral results of RRPA-MQWs before and after annealing at 300 ºC and 400 ºC for 1 hour in an Argon gas environment. CL taken at V_B = 2 kV, I_B = 3.8 nA, T = 80 K, showing 80% of the initial luminescence intensity retained after the 400 ºC anneal. (b) CL spectra suggesting that H plasma is highly reactive and thoroughly diffuses through the MQWs, occupying V_{Zn} and BSFs sites and enormously enhancing MQW emissions. In contrast, if the pristine MQWs is annealed in a H_2 atmosphere instead of plasma at 350 ºC for 1 hr almost no change is seen in CL spectra, other than a slight change in intensity.

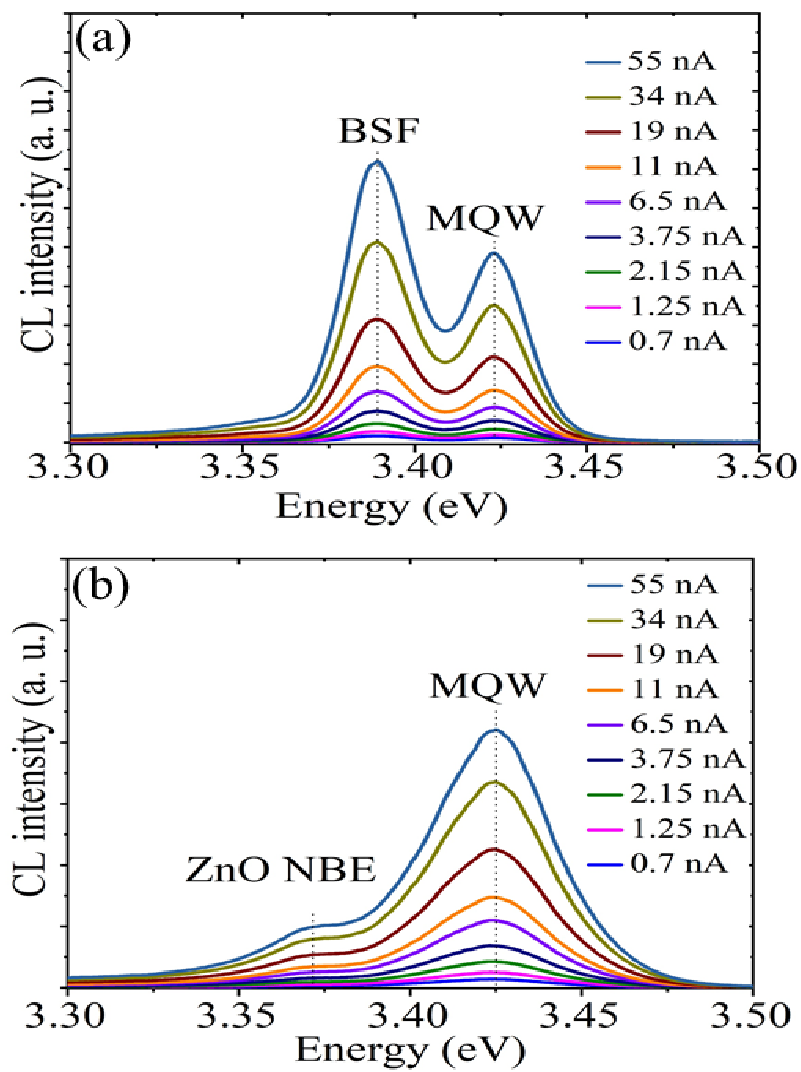

Fig. 4.7: Power-resolved CL spectroscopic results of (a) pristine and (b) RRPA-MQWs. The accelerating voltage was kept constant at 2 kV, while the beam current (I_B) was increased from 0.7 nA to 55 nA. The MQW, BSF and ZnO NBE emission peaks are not shifting with increasing power.

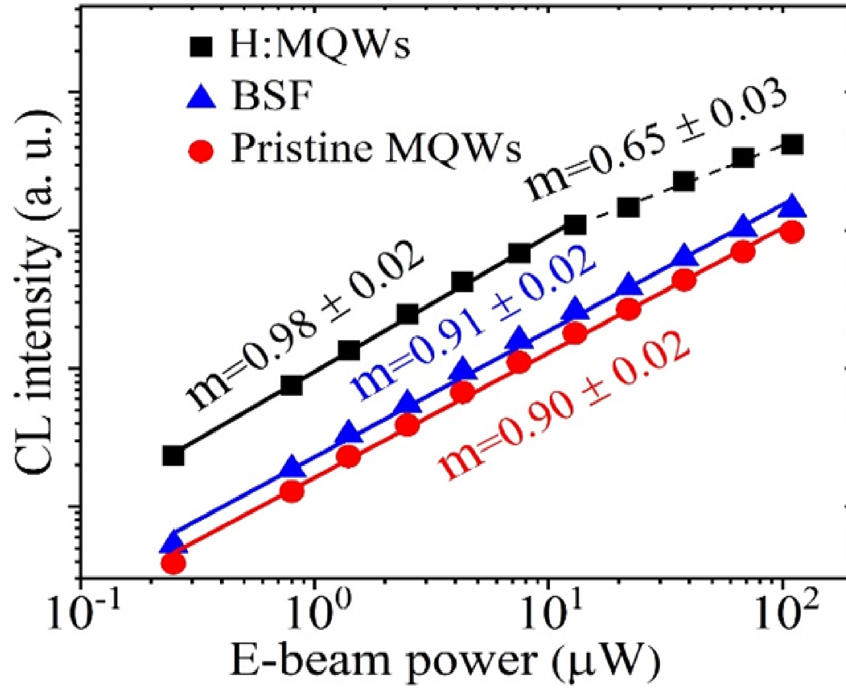

Fig. 4.8: Log-log plots based on the power-law model ($I_{CL} \propto P^m$), which yields the power index m = 0.90 ± 0.02, 0.98 ± 0.02 and 0.91 ± 0.02 for pristine MQW, H-doped MQW and BSFs emission, respectively.

4.3.3. Temperature- and Excitation-dependent CL

The MQW emission peak enhancement and their excitonic recombination mechanism is further investigated by power-resolved CL analysis for both pristine and RRPA-treated MQWs (Fig. 4.7(a and b)) at a fixed e-beam accelerating voltage (2 kV), while the e-beam current was changed from 0.7 nA to 55 nA. The peak position energy of the MQW emission in both (RRPA and pristine) MQWs samples are unchanged with increasing excitation power, indicating negligible quantum confined Stark effect, consistent with a nonpolar MQWs system.[147] The spectra are analysed using the power-law model, $I_{CL} \propto P^m$, where I_{CL} is the CL intensity and P is the e-beam power. The log-log plots (Fig. 4.8) based on the power-law model yielding the power index m =

0.90 ± 0.02, 0.98 ± 0.02 and 0.91 ± 0.02 for pristine MQWs, H-doped MQWs and BSFs emission, respectively. These values indicate that these emissions are of excitonic nature and not related to a lattice-coupled defect.[151] Following the incorporation of H, the power index *m* increases from 0.90 ± 0.2 to 0.98 ± 0.2 due to the H passivation of competitive recombination channels. The saturation of exciton recombination in the RRPA-treated MQWs (m = 0.65) at P > 13 μW is due to the activation of competitive H-related channels with increasing e-beam excitation current.

To investigate the recombination dynamics of CL spectra for both pristine and RRPA-treated MQWs samples, temperature-dependent CL microanalysis have been carried out at a fixed accelerating voltage and e-beam current. The resulting temperature-resolved CL spectra for both (pristine and H-doped) MQWs are shown in figure 4.9 (a,b) in a temperature range of 80 to 200 K. Three luminescence peaks (MQW, BSF and ZnO NBE) are red-shifted with increasing temperature due to thermal bandgap shrinkage. Voigt function fitting of the CL spectra gives the integrated intensities of the ZnO NBE, BSF, and MQW emission peak along with their full width at half maxima (FWHM) for all temperature range; an example of the fitting deconvolution is displayed in figure 4.9(c). Thermal quenching of these luminescence bands with increasing temperature follows an Arrhenius nature with activation energies of E_a = 33.1 ± 1.5 and 46.2 ± 2.2 meV for the MQW emission in the pristine and RRPA-treated MQWs samples, respectively, as depicted in figure 4.9(d). The activation energy value of the BSFs emission (29.9 ± 1.7 meV) is consistent with the reported value for nonpolar MgZnO/ZnO MQWs.[147] Further, this E_a value is notably similar to that of the MQW band in the pristine MQWs, suggesting that the thermal activation of carriers is controlled by the thermal activation of competitive non-radiative recombination centres, which is expected for MQWs structures prior to the H passivation of defects. The activation energy (E_a) of

the RRPA-treated MQW emission is identical to the binding energy of H donors in ZnO, [35] pointing towards the activation of a dominant recombination channel related to the ionisation of H donors. It can be observed from Fig. 4.9(a, b) that the linewidth of MQW emission peak becomes broader after the H introduction, which can be attributed to a change in the exciton-phonon interaction strength, as a result of H passivation of defects. Figure 4.10 shows the temperature dependence of the FWHM of the MQW emission for the pristine and H-doped MQWs structures. Based on Segall's expression for the temperature-dependent linewidth of excitons, the FWHM can be described by the following equation: [152]

$$\beta(T) = \beta_{inh} + \beta_{ph}T + \frac{\beta_{LO}}{\exp(\hbar\omega_{LO}/k_B T)-1} \tag{4.1}$$

where β_{inh} is the temperature-independent term describing the inhomogeneous linewidth accounting for the scattering of impurities, defects and well-width fluctuations. The second term is associated with the acoustic phonon scattering, which is negligibly small compared with the LO scattering and can be ignored at T > 80 K. [153] The third term is the linewidth due to the LO phonon scattering, which dominates the phonon scattering at high temperatures (β_{LO} and $\hbar\omega_{LO}$ are the phonon coupling strength and LO phonon energy, respectively). The $\hbar\omega_{LO}$ was used for curve fitting procedure in our temperature-dependent MQW linewidth. The energy for $\hbar\omega_{\mathrm{LO}} = 72$ meV has already been studied to be invariant with the well-width for ZnO MQWs.[154] Both solid line curves in figure 4.10 represent the best fit to the FWHM data points based on equation 4.1, yielding β_{inh}= 17 meV and β_{LO} = 130 meV for the pristine MQWs, and β_{inh}= 25 meV and β_{LO} = 371 meV for the 40 second RRPA-treated MQWs. The higher β_{inh} value in the RRPA-treated MQWs is likely due to the formation of additional recombination channels via H donors. This higher value of β_{inh} for RRPA-treated MQWs structure lead to additional scattering

by H impurities and H-defect complexes. The notable increase in β_{LO} in the MQWs after the RRPA treatment indicates a much stronger exciton-LO phonon coupling process in the optical emission of the RRPA-treated MQW structure. For comparison, β_{LO} is ~ 250 meV for epitaxial-grown undoped MQWs with a similar well-width on the lattice matched substrate. [155] Previous studies by other workers have shown that as the quantum well thickness becomes larger, β_{LO} increases because of a lowered exciton binding energy. [153] The exceptionally high β_{LO} in the RRPA-treated MQWs can be attributed to a reduction in the exciton binding energy due to the enhanced screening of excitons by free electrons that are produced by H donors in ZnO.

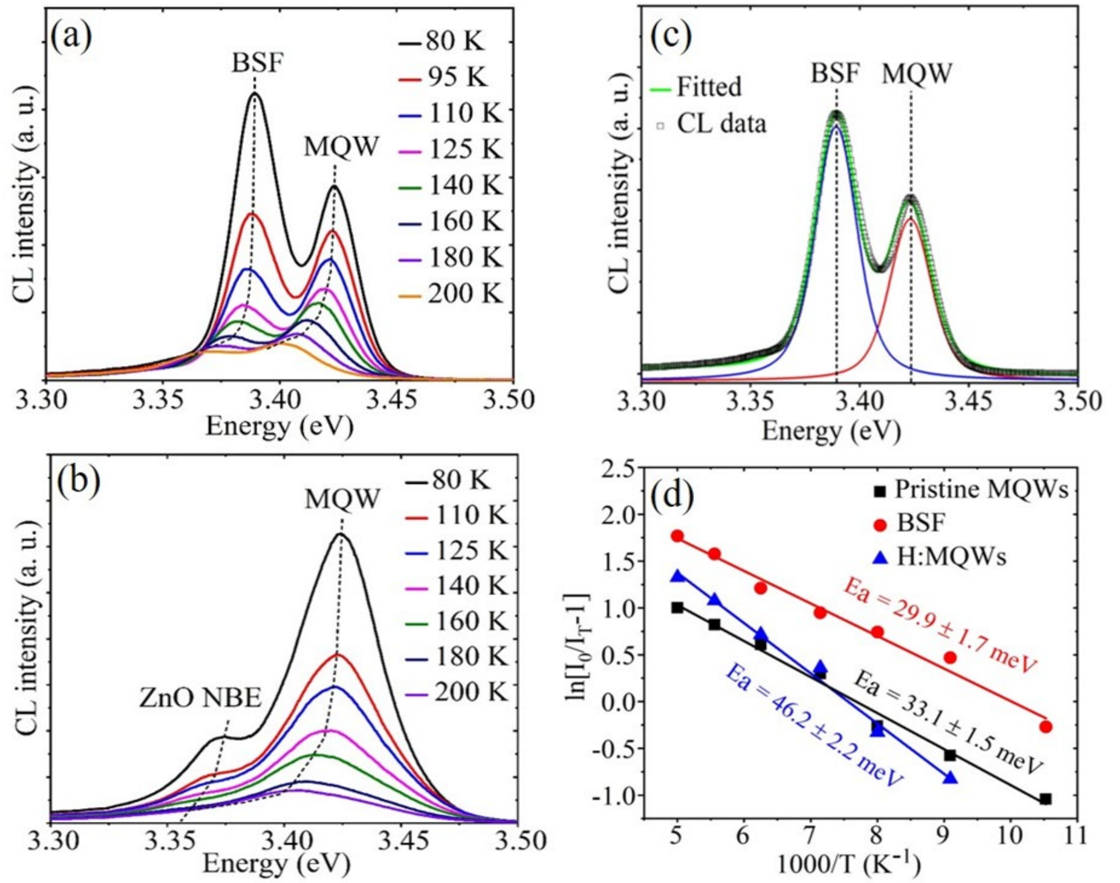

Fig. 4.9: Temperature-resolved CL spectra of (a) pristine and (b) 40-sec RRPA-treated MQWs samples at accelerating voltage V_B = 2 kV, I_B = 3.8 nA in a temperature range of 80–200 K. (c) Example of a fitted CL spectrum for extraction of the integrated intensities of BSF and MQW emission peaks and FWHM for the entire temperature range. (d) Arrhenius plots of the intensities of MQW (both pristine and RRPA) and BSF emissions, yielding the thermal activation energy E_a = 29.9 ± 1.7 meV for BSFs emission and 33.1 ± 1.5 meV and 46.2 ± 2.2 meV for the pristine and RRPA-treated MQWs emission, respectively.

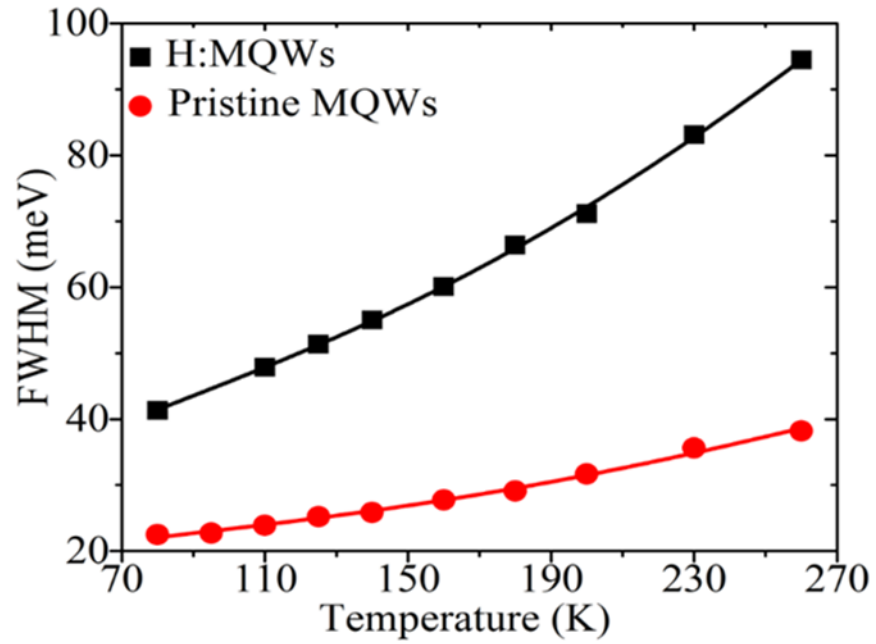

Fig. 4.10: FWHM of the MQW emission as a function of temperature for pristine and RRPA-treated MQWs. The solid line represents the fit to the experimental data points according to equation 4.1. The larger FWHM in the RRPA-treated MQWs is due to enhanced exciton-phonon coupling strength.

4.3.4. Depth-dependent CL Analysis

To further explore the spatial distribution of luminescence emission in the MQWs structure, depth-dependent CL was carried out for the pristine and RRPA-treated MQWs. In this measurement, the e-beam power and hence the injected electron-hole (e-h) pair rate (e-beam current) in the sample was kept constant as the CL excitation depth was increased by raising the electron beam energy (accelerating voltage). Monte Carlo simulation was carried out using the CASINO programme to determine the spatial distribution of the injected electron-hole pairs in the MQWs for the acceleration voltages between 2 and 7 kV as depicted in figure 4.11.[156] The depth profiles reveal that at V_B = 2 kV the measured MQW emission is generated only from the top four QWs, with the upper QWs contributing a stronger MQW signal compared with the bottom QWs emission. At V_B = 4 – 5 kV the MQW optical emission is contributed fairly by all 12 MQWs, while V_B > 6 kV an increasing number of e-h pairs are generated within the ZnO buffer layer region. Depth-resolved CL analysis was compared with CASINO simulated electron energy loss results, as shown in figure 4.12(a). Two peaks are observed: MQWs and BSF with peak positons at 3.389 eV and 3.423 eV, respectively. The energy separation between the MQW and BSFs emission is 35 ± 2 meV, consistent with the reported value for a non-polar MQWs system.[147] The slight variation in the MQW emission energy is attributed to strain inhomogeneities due to the lattice mismatch between the substrate and the bottom quantum wells layers.[157] Figure 4.12(b) shows the measured luminescence enhancement factor, which is defined as the ratio of the MQW emission intensities from the RRPA-treated MQWs to the pristine MQWs, as a function of V_B. A second top x-axis is also shown to display the sampling depth simulated from CASINO results. The enhancement factor increases with V_B up to 4 kV, which is then followed by a slow decline after reaching a maximum value of 18. The maximum MQW

enhancement factors at 4-5 kV confirms that H diffuses into all the MQWs. The surface degradation caused by H plasma could contribute to low enhancement factors in the top four QWs. Another consideration is that H could diffuse out from top MQWs, which cannot be ruled out. The decline in the enhancement factor at $V_B > 5$ kV could be due to self-absorption effects as photons from deep QWs are absorbed by upper MQWs.

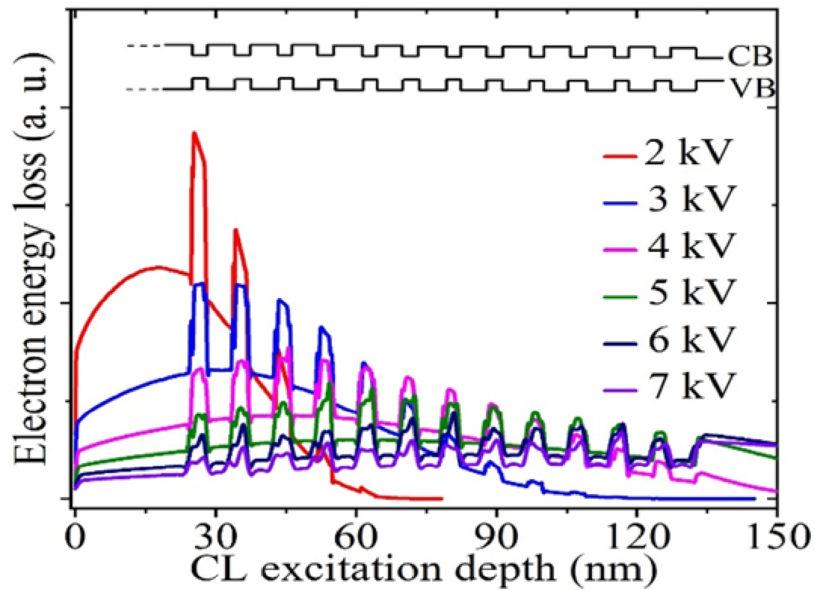

Fig. 4.11: CASINO-simulated electron energy loss profiles generated in the MQWs for V_B = 2–7 kV, showing the e-beam reaches all 12 MQWs at 4 kV. Inset shows a schematic diagram of the valence and conduction bands for the MQWs structure.

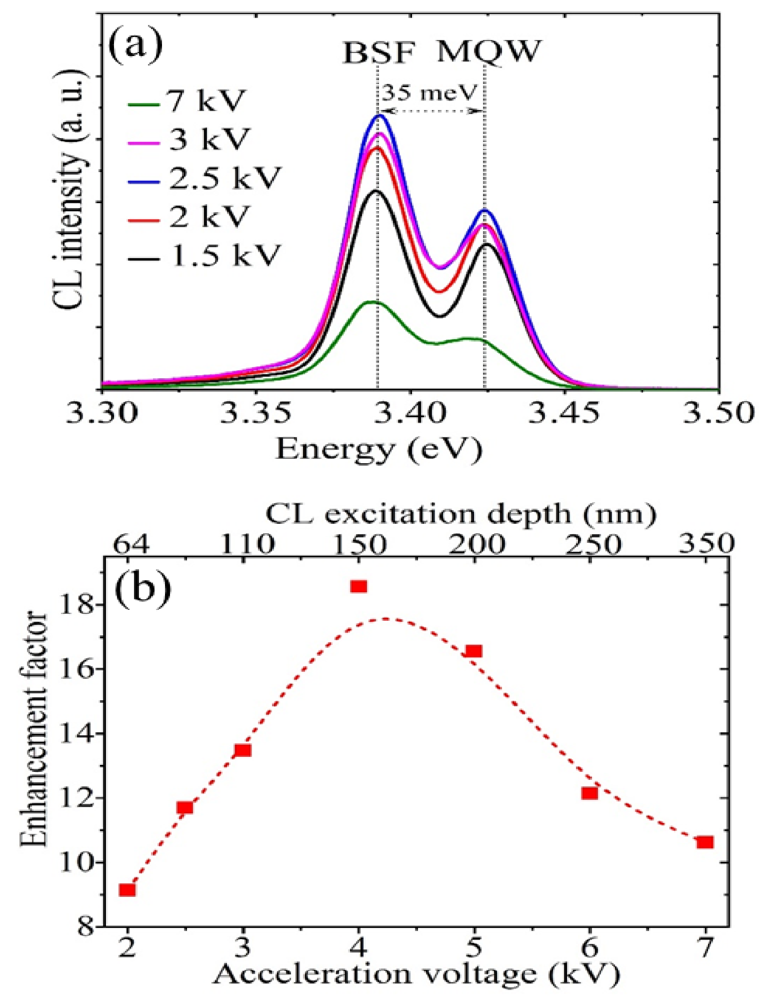

Fig. 4.12: (a) Depth-resolved CL spectra of pristine MQWs at 80 K over a range of acceleration voltages from 1.5 to 7 kV at constant beam power ($V_B \times I_B$) of 15 μW. (b) The enhancement factor (the intensity ratio of the RRPA-treated to pristine MQWs) as a function of acceleration voltage (bottom x-axis) and excitation depth (top x-axis).

4.4. Conclusions

The effects of the incorporation of H via RRPA treatment on the radiative emission from MgZnO/ZnO MQWs have been systematically investigated. RRPA treatment can be used to effectively control and tune the optical features of MgZnO/ZnO MQWs, while the crystal structure integrity is unchanged. The optical emission of pristine and RRPA-treated MgZnO/ZnO MQWs samples has been studied by CL probing technique. H doping was found to have pronounced effect on the MQWs emission intensity, while the BSFs and deep-level emission are completely suppressed. The integral intensity of MQW emission was improved by around 10 times compare with the pristine MQWs sample. Based on the CL kinetics and temperature-dependent measurements, the enhancement is attributed to the passivation of competitive recombination channels, most likely point defects and stacking faults in the MQW structure. Theoretical modelling of the MQW spectral line width indicates that the exciton and LO phonon coupling process is much stronger in the plasma-treated MQWs, which arises from exciton screening effects. The work shows that rapid plasma annealing presents a facile, effective method to enhance the optical quality of oxide-based MQWs structures.

Chapter 5

5. Nitrogen Acceptors in MgZnO

In this chapter, the optical and structural properties of N-doped MgZnO thin film are described. It is well known that ZnO is naturally n-type, while a p-type is mandatory to fabricate bipolar junction devices. It is still a challenge to fabricate a reliable, stable and reproducible p-type ZnO material. p-type ZnO should have a sufficient amount of acceptor concentration to produce an excess of holes carriers. N is the well explored and still a strong candidate dopant for producing acceptors contents in ZnO as well as MgZnO. Significantly, the alloying of ZnO with the optimized amount of Mg increases the band gap and improves the incorporation of N acceptors as well as reducing the concentration of residual intrinsic donors-like defects in ZnO. Therefore, here the in-depth optical analysis along with it chemical signatures of intentional N acceptors in MgZnO epilayer will be discussed.

5.1. Introduction

Wide band gap oxide-based semiconductors have emerged in recent years as an important material for use in a number of optoelectronics applications. [8, 158] In spite of the lack of availability of majority p-type doping, ZnO has become one of the most prevalent oxide semiconductors, thanks to a distinctive property set including: a direct wide band gap, intrinsically high transparency over the whole visible range, a relatively high piezoelectric response and a resistivity that can be tuned from semi-insulating right

through to semi-metallic by doping. Moreover, the band gap of ZnO can be engineered upwards by alloying with MgO to fabricate UV sensors, quantum wells and 2DEG at MgZnO/ZnO heterointerfaces.[13] Further, it has been shown that epitaxial growth can allow MgZnO to retain the wurtzite structure up to 33 at% of Mg,[78] which takes it into the range of ultra-wide-bandgap semiconductors and makes it potentially attractive for use in future high-power electronics devices. Analogous to ZnO, the group VA elements N, P, As and Sb substituted on oxygen anion sites are considered potential acceptor dopants in MgZnO, with N being the most promising candidate as the shallowest acceptor.[159-161] Indeed, it is already known that N can be favourably substituted onto an oxygen site (N_O) and act as an acceptor in ZnO because it has a similar ionic radius to oxygen as well as well-matched Zn-O and Zn-N bond lengths of 0.193 and 0.188 nm, respectively.[64, 69]

Computational studies, supported by Raman measurements, have revealed that alloying ZnO with MgO enhances the solubility of N by lowering the formation energy of substitutional N_O acceptors, and thereby increases the doping concentration level.[4] It is postulated that holes generation may be increased through the substitution of Zn by isovalent Mg, which further improves the N solubility and raises the ionisation energies of compensating donors.[162-164] Moreover, several groups have adopted MgZnO:N for the p-side in fabricating exploratory MgZnO bipolar homojunction devices.[160, 165] However, considerable controversy still exists over the chemical identity of N acceptors in MgZnO. To date, most of the literature on N doping in MgZnO primarily relates to electrical characterisation, with only a few studies targeting study of the N acceptors themselves. Although UV emission bands in MgZnO close to the band gap have been unambiguously assigned to neutral (D^oX) and ionised donor-bound excitons (D^+X),[166,

167] neutral acceptor bound excitons (A^oX) reported in the literature[5, 167] have not yet been unequivocally identified.

In this chapter, a more detailed study is presented to provide a deeper understanding of the chemical and optical properties of N acceptors in MgZnO:N. Although, ion implantation could be a viable technique to explore high N doping levels, this method generally creates significant damage to the crystal lattice, so alternatively an in-situ approach was adopted in this study involving PLD. $Mg_{0.16}Zn_{0.84}O$ epilayers were fabricated by PLD using similar conditions but under three different growth ambients, N, oxygen and vacuum, shown in Table 5.1. NEXAFS and PL spectroscopy were used to systematically investigate the chemical and optical properties of the MgZnO epilayers. The results are in good agreement with the classical picture of N in ZnO, albeit it with a significantly deeper acceptor level in MgZnO. Hence, it was established that N is primarily incorporated in MgZnO:N in the $(N_2)_{Zn}$ chemical state, giving a strong signature of DAP emission centred at 3.45 eV at 80 K. This, along with a marked increase in resistivity, indicates that $(N_2)_{Zn}$ is playing the role of a compensating deep acceptor in MgZnO.

Table 5.1: Values for three MgZnO film thicknesses with their corresponding ambient conditions on ZnO buffer layer and c-sapphire substrate. The buffer layer thickness is 145 nm. All other growth parameters are the same except for the different ambient growth conditions. The film thicknesses were determined by optical reflection interferometry with an Ocean Optics system.

Thin film	**Thickness (nm)**	**Growth ambient**
MgZnO:O	95	O_2
MgZnO:N	180	N_2
MgZnO:vac	80	vacuum

5.2. Structural and Morphological Properties

Surface morphological characteristics of the three different MgZnO epilayers have been studied by AFM and SEM microscopy, as shown in figure 5.1 (a & b). The AFM was carried out in a non-contact tapping mode to find the surface texture. The main finding from AFM and SEM imaging is that no noticeable differences in the surface morphology were observed for all three types of MgZnO. The root mean square roughness (RMS) are almost similar (5.3 to 6.0 nm) and showing a good uniformity of all three different PLD growth MgZnO thin films. Therefore, the type of ambient conditions, N, oxygen, and vacuum during PLD growth of MgZnO films does not have a noticeable

effect on their surface morphologies. The parameters extracted from XRD rocking curve, AFM and electrical resistivity by four-probe method are summarised in Table 5.2.

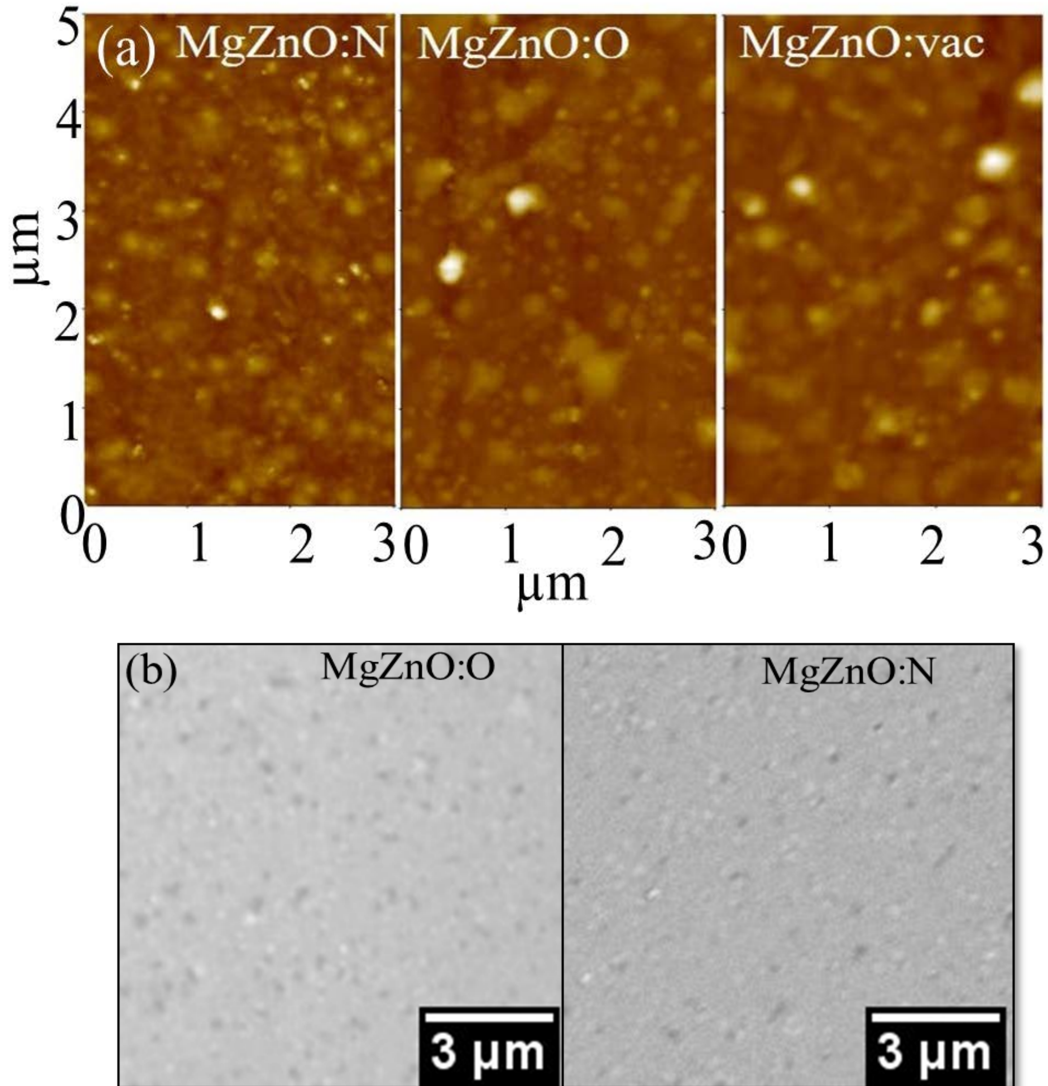

Fig. 5.1: (a) AFM images of MgZnO:N, MgZnO:O and MgZnO:vac and their corresponding RMS values for surface roughness: 5.3, 6.0 and 5.8 nm, respectively for 5 × 3 μm^2 scanning area. (b) SEM images for MgZnO:O and MgZnO:N films along with their scale bar.

Table 5.2: *c* lattice parameter, FWHM of rocking curves for (0002) plane, RMS surface roughness and electrical resistivity (ρ) for the ZnO underlayer and MgZnO/ZnO bilayers at 300 K. Electrical resistivity was measured using a Signatone co-linear four-point probe system equipped with a Keithley 2400 source meter.

Layer	**c (Å)**	**Rock curve FWHM (°)**	**Roughness (nm)**	**ρ (Ω.cm)**
ZnO	5.218	0.006	0.9	0.07
MgZnO:N/ZnO	5.209	0.095	5.3	0.60
MgZnO:O/ZnO	5.162	0.09	6.0	0.08
MgZnO:vac/ZnO	5.223	0.10	5.8	0.08

5.3. Near-edge X-ray Absorption Fine Structure

To investigate the chemical states of N in MgZnO:N/ZnO, NEXAFS spectra were acquired around the N K-edge, which corresponds to resonant electron transitions from the N 1*s* initial state to the final unoccupied N-related states of *p*-symmetry. Figure 5.2 shows the NEXAFS measurements for the MgZnO:N/ZnO and MgZnO:O/ZnO layers. The spectra for the MgZnO:O/ZnO and MgZnO:vac/ZnO are featureless showing only background signal around the N K-edge since their N content is below the NEXAFS detection limit. Conversely, the NEXAFS spectrum for the MgZnO:N/ZnO comprises four distinct resonant peaks (labelled P1, P2, P3 and P4). The strong resonance P1 at 400.7 eV is consistent with the characteristic N 1*s* to π^* transition in N-N species.[168] To the best of our knowledge, there are no NEXAFS data for N in MgZnO; however, a similar sharp resonance peak, close to the P1 position, has previously been ascribed to

molecular N in ZnO [66], GaN [169], and InN [170] that were doped with N ions. Accordingly, the resonance P1 attribute to N molecules in MgZnO:N. The shoulder P2, at 399.7 eV, is at the same position as the resonance previously observed in N-doped ZnO crystals and can be assigned to the transition involving N $2p\pi^*$ and Zn $3d$ hybridised orbitals [66, 171]. The structural resemblance of P2 in MgZnO and ZnO indicates the formation of N-Mg and N-Zn bonds, consistent with N substitution on oxygen sites (N_O) in the lattice. The higher energy components, P3 and P4, are close to the characteristic absorption peaks of various N oxides, such as NO_2 (at 403.2 eV) and N_2O (at 404.5 eV)[171, 172], which indicates the existence of substitutional N on Zn sites in the MgZnO:N epilayer. It is proposed, therefore, that N ions are present in several oxidation states in MgZnO, in addition to the configurations N_O and N_2, by forming N-O, O-N-O and N-N-O bonds. The relative intensities of the N chemical states were obtained by deconvoluting the N K-edge spectrum using a Gaussian-Lorentzian function, as shown in figure 5.2, showing that about half of N exists in the N_2 state while only ~ 13% is in the N_O states. Moreover, the relative integral intensity with their corresponding chemical signatures are shown in Table 5.3.

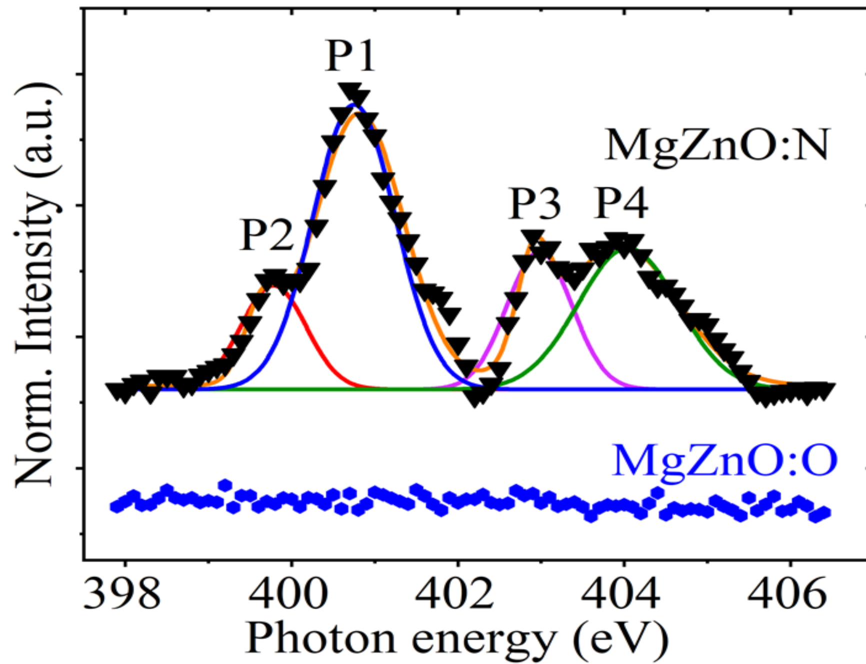

Fig. 5.2: (a) NEXAFS N K-edge spectra of MgZnO:N/ZnO and MgZnO:O/ZnO recorded in the bulk-sensitive TFY mode. The N content in the MgZnO:O/ZnO and MgZnO:vac/ZnO was below the NEXAFS detection limit. The spectrum of the MgZnO:N/ZnO is fitted with four mixed Gaussian–Lorentzian functions (the solid curve is the fit) corresponding to four different chemical states of N. The experimental data are shown as a non-continuous curve of triangular and hexagonal points.

Table 5.3: Peak position and their corresponding chemical signature, and relative intensity in percentage for each peak in the NEXAFS measurements.

Peak	Peak position (eV)	Chemical signature	Relative percentage of intensity (%)
P1	400.7	N_2	46
P2	399.7	N_O	13
P3	403.0	NO_2	18
P4	404.1	N_2O	23

5.4. Optical Band Gap Analysis

Transmission spectrophotometry (figure 5.3a) was used for the optical band gap determination by using Tauc's relation (equation 5.1). The wave like pattern in the transmission spectra is due to interference effect in thin film and shows that the film is low surface roughness and highly uniform thickness.[173] Transmission spectra shows two falling of transmission, so-called transmission edge. These transmission edges correspond to ZnO and MgZnO layers at around 3.38 and 3.60 eV, respectively. Figure 5.3(b) shows the Tauc's plot for the three bilayers. There are sharp absorption edges at ~3.38 eV and ~3.6 eV, corresponding to the optical band gaps of the ZnO underlayer and the MgZnO over-layer, respectively. The Tauc's plots also show that the band gap of MgZnO:N is a bit smaller than the MgZnO:O by only ~ 5 meV, and combined with the

XRD results, indicating that the N doping has little effect on the band structure and crystalline quality of the MgZnO epilayer in this PLD fabrication route:

$$\alpha h\nu = C\left(h\nu - E_g\right)^n \quad (5.1)$$

where $\boldsymbol{\alpha}$ is absorption coefficient, C is constant, h is Planck's constant, ν is frequency of incident radiation and E_g is band gap of the thin film. The value of n depends on the nature of the material band gap. The power index n of 2 or ½ corresponds to indirect and direct bandgap semiconductor materials, respectively. Figure 5.3a shows two transmittance edges corresponds to ZnO and overlayer MgZnO thin films. The ZnO transmittance edge is completely sharp while the sharpness of MgZnO transmittance edge is affected by Mg impurity concentration. The Tauc's relation were plotted for MgZnO and ZnO band gap in their region of interest as shown in figure 5.3b. The two linear portions as shown by dotted line in figure 5.3b represents direct band gap nature of ZnO and MgZnO thin films. The dotted lines shown in figure 5.3b, interpolated from linear part of the graph and intercept at x-axis ($h\nu$). The intercept on the x-axis indicates the band gap: E_g(ZnO)=3.36 eV and E_g(MgZnO)=3.60 eV.

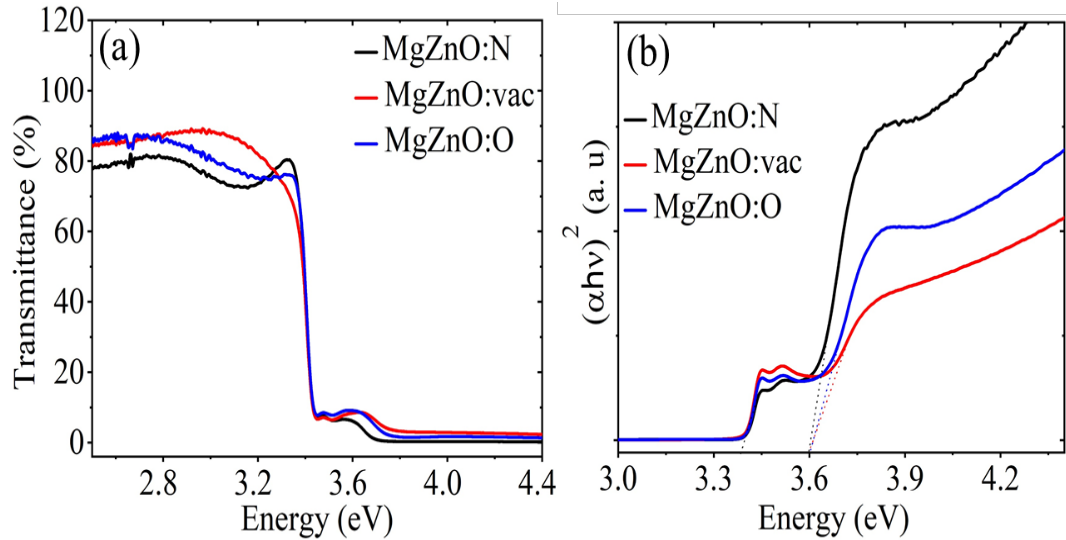

Fig. 5.3: (a) Optical transmission spectra for three type MgZnO with maximum transmittance around 84%. (b) Tauc's plots for optical absorption of the epilayers yielding a band gap of ~3.38 eV for the ZnO underlayer and ~3.6 eV for the MgZnO over-layer.

5.5. Photoluminescence Spectroscopy

To study the N acceptors related luminescence characteristics in MgZnO epilayers, PL techniques were employed. Three different MgZnO with three different growth environment (N, oxygen and vacuum) and one buffer layer of ZnO were probed under identical laser probing conditions, using a laser wavelength of 325 nm and a vacuum of ~10^{-6} mbar in the chamber.

5.5.1. Donor–acceptor-pair Emission

The PL spectra for the MgZnO:N/ZnO, MgZnO:O/ZnO and MgZnO:vac/ZnO bilayers and of the ZnO buffer layer are displayed in figure 5.4. Two sharp peaks at 3.352 and 3.373 eV, observed in all PL spectra, are attributed to the radiative recombination channels of donor-bound excitons (DX) and free excitons (FX) peaks in the ZnO buffer layer, respectively.[174] Additionally, all epilayers samples exhibit a periodic set of PL

peaks at 3.519, 3.592, 3.665 and 3.739 eV as a result of multiphonon resonant Raman scattering (RRS).[175] These sharp Raman peaks are separated from the He–Cd 3.812 eV laser line by multiples of the LO phonon energy of MgZnO, E_{LO} = 73 meV, where the Raman peak position (E_{RRS}^n) is given by $E_{RRS}^n = 3.812 - nE_{LO}$ eV (n = 1, 2, 3, 4).[176] The presence of the RRS peaks confirms the high crystalline quality of the epilayers.[175, 176] Significantly, all three of the MgZnO epilayers exhibit a broad NBE PL response positioned at 3.61 eV, which is consistent with the band gap measured using the Tauc's plot in figure 5.3. The broadening of the MgZnO NBE is most likely due to potential fluctuations effects caused by lattice disorder in the MgZnO alloy thin film. In comparison, the MgZnO:N/ZnO bilayer shows an additional broad PL emission centred at 3.45 eV, which is 160 meV below the MgZnO NBE. This rules out its assignment to a N acceptor bound exciton emission that is reported to be to less than 100 meV below the bandgap of MgZnO films.[5, 177] The 3.45 eV PL emission in the MgZnO:N is similar to a previously reported shallow DAP transition in N-doped ZnO at 120 meV below the NBE.[66, 178] This result indicates that the N acceptor level in MgZnO:N is ~ 40 meV deeper than in ZnO:N, assuming that the binding energy of the dominant donor in ZnO and MgZnO is similar. This deeper nature of N acceptors in MgZnO:N is in agreement with the expected downward shift (ΔE_{VB}) of the $Mg_{0.16}Zn_{0.84}O$ valence band maximum relative to the ZnO level due to the ZnO/MgZnO band offsets; as in, for example, Ohtomo et al. [179], which reports a ΔE_{VB} = 46 meV for ZnO/$Mg_{0.2}Zn_{0.8}O$. The DAP emission shift from the NBE emission is also comparable with the reported level of E_V + 160 meV measured by deep level optical spectroscopy for acceptors in N-doped MgZnO with 10 at% Mg.[164]

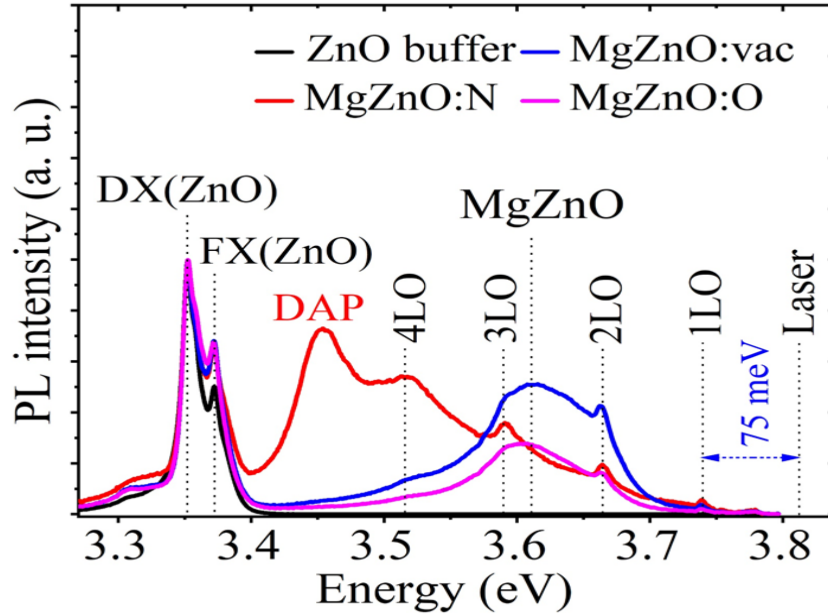

Fig. 5.4: PL spectra of the MgZnO/ZnO bilayers and the ZnO underlayer (T = 80 K, E_{laser} = 3.814 eV, I_{laser} = 2 kW/cm^2). The MgZnO:N exhibits a pronounced DAP emission at 3.45 eV due to N acceptors. The FX and DX emission peaks originate from the ZnO underlayer. The four sharp Raman peaks (labelled 1LO, 2LO, 3LO and 4LO) are separated from the laser line by multiples of the LO phonon energy of 73 meV.

5.5.2. Temperature-dependent Photoluminescence

Temperature dependence PL of the radiative transitions gives insights into the thermal behaviour and activation energies of the recombination channels. Figure 5.5 displays the temperature-resolved PL spectra for the ZnO NBE and MgZnO emission bands. With increasing temperature, the ZnO DX emission is quenched rapidly as neutral shallow donors become increasingly unavailable for radiative recombination as a result of their thermal ionisation. Concurrently, the intensity of the ZnO FX peaks decreases, broadens and red shifts because of lattice dilation and electron-phonon interaction at low and elevated temperatures, respectively. In a similar manner, the MgZnO:N NBE, at around 3.60 eV, shifts to lower energy and quenches as the temperature increases from

80 K, whereas the intensity of the MgZnO DAP is rather independent of temperature up to 140 K. As expected, being independent of temperature, the positions of the sharp RRS emission peaks remain constant. Figure 5.6 (a) shows the temperature dependence of the peak position of the MgZnO:N DAP peak and the ZnO FX for comparison. The plot reveals that the DAP initially redshifts from 80 to 180 K and then blue shifts from 180 K onwards. This “S-shape” profile is highly characteristic of DAP recombination in semiconductor alloys with significant band-edge potential variations caused by compositional fluctuations.[180] Here, as the temperature increases from 80 K, photo-generated carriers are able to populate from deeper local potential minima arising from compositional fluctuations, which produces the observed redshift. With a further temperature rise above 180 K, these deep states empty due to thermal ionisation, leading to the blue shift in the peak position. The DAP blue shift could result from shallow donor thermal ionisation. However, figure 5.6 (a) shows that the DAP red shifts at a much slower rate than the FX with increasing temperature, which supports the thermal fluctuation mechanism. Since the 3.45 eV peak is completely absent in the MgZnO:O/ZnO and MgZnO:vac/ZnO bilayers, this “S-shape” behaviour strongly supports the assignment of the 3.45 eV PL emission in the MgZnO:N/ZnO bilayer to DAP recombination involving a N deep acceptor. The Arrhenius plots of the ZnO FX and MgZnO:N DAP intensities are shown in figure 5.6(b), yielding activation energies of 63 ± 4 and 48 ± 3 meV, respectively. The measured E_a value for the FX is consistent with the exciton binding energy of ZnO (60 meV) and associated with thermal disassociation of excitons. The 48 meV E_a value of the MgZnO:N DAP is similar to the reported binding energies (43 and 56 meV) for N acceptors in MgZnO films.[5] However, this E_a value is too low to be logically ascribed to thermal ionisation of the N acceptor involved in the 3.45 eV emission, which has much greater binding energy as estimated above.

Accordingly, the 48 meV activation energy of the DAP in MgZnO is assigned to the binding energy of the dominant donor in the MgZnO layers.

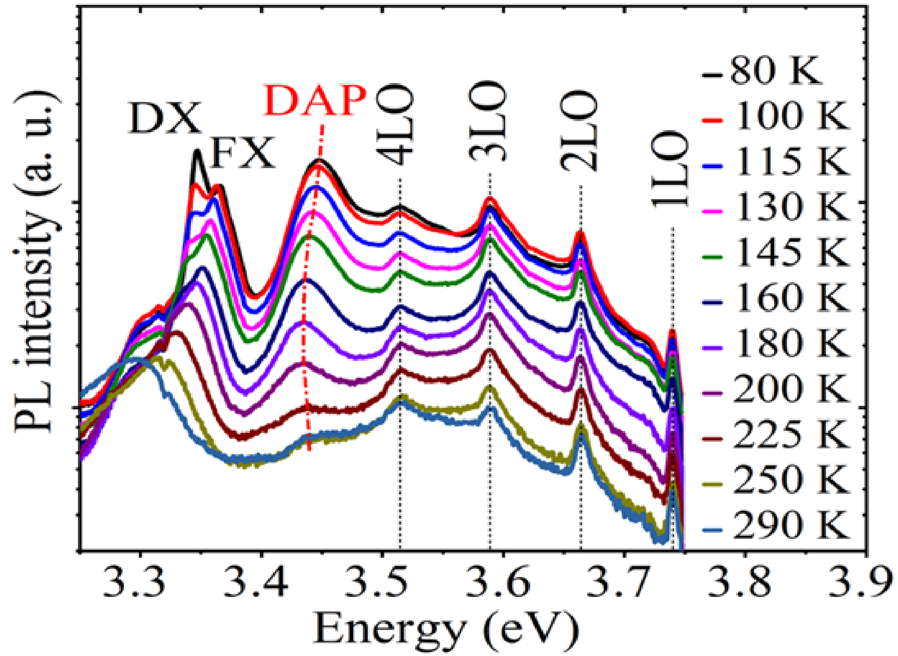

Fig. 5.5: Temperature-resolved PL spectra for the MgZnO:N/ZnO sample with a logarithmic intensity scale for a temperature range 80–290 K.

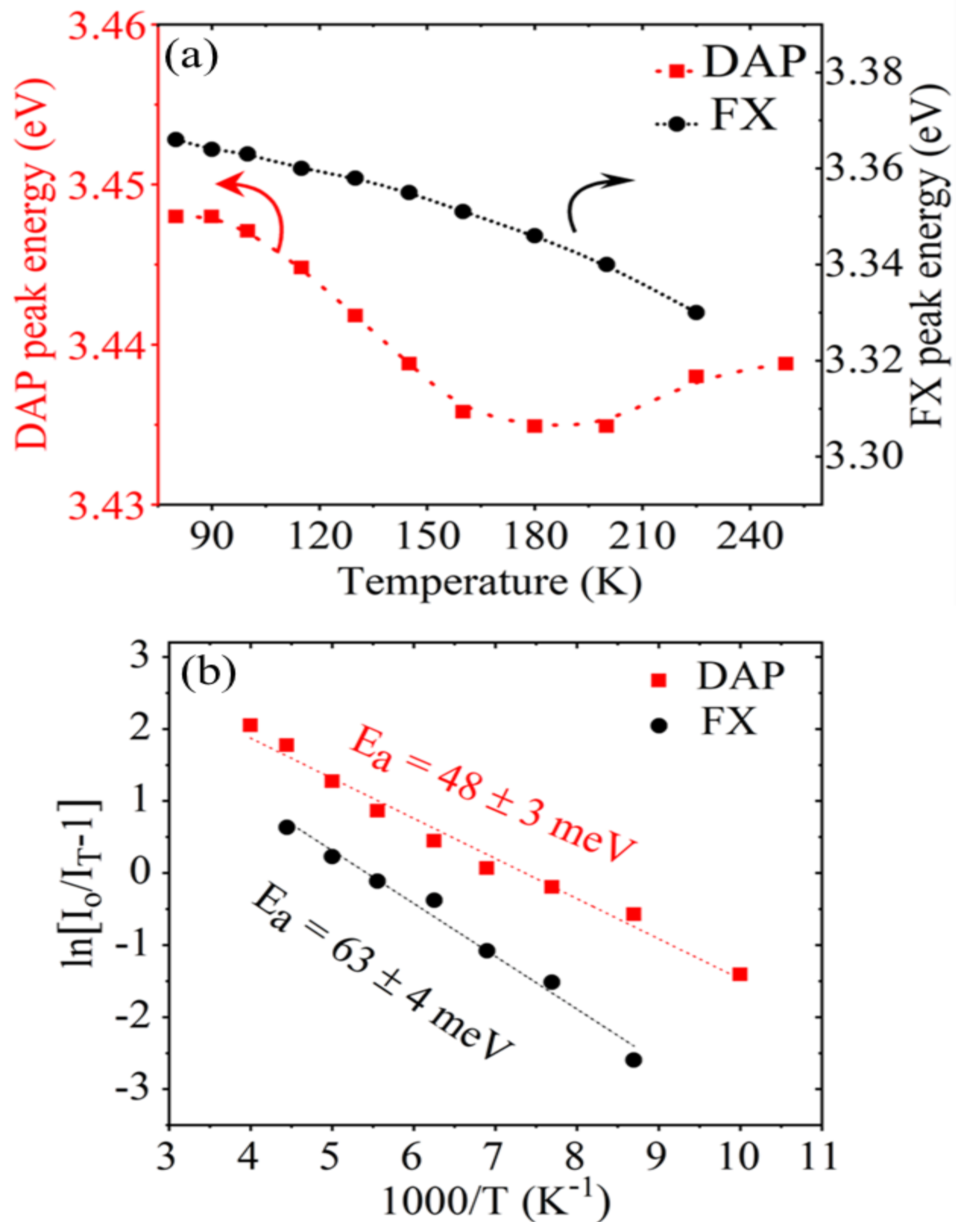

Fig. 5.6: (a) Peak energies for the ZnO FX and MgZnO N-related DAP emissions in MgZnO:N/ZnO as a function of temperature. The FX peak position redshifts monotonically with increasing temperature, while the DAP follows an 'S-shape' emission shift due to compositional fluctuations. (b) Arrhenius plots yielding $E_a = 48 \pm 3$ eV and $E_a = 63 \pm 4$ eV for the DAPs of MgZnO and FX of ZnO, respectively.

5.5.3. Excitation Power-dependent Photoluminescence

To confirm the nature of the emission bands, power-dependent PL measurements was conducted for the MgZnO:N/ZnO bilayer, as shown in figure 5.7. With increasing laser intensity, the FX and RRS peak positions remain unchanged, whereas the 3.45 eV band gradually shifts to higher energies as shown in Fig 5.8(a). This blue shift with increasing excitation power is characteristic of DAP transitions and is explained by the Coulombic interaction between spatially separated DAPs at different distances.[178] The emission energy of the DAP is given by the following relationship:

$$hv(\text{DAP}) = E_g - (E_A + E_D) + \frac{e^2}{4\pi\epsilon r} \tag{5.2}$$

where E_g is the bandgap, r is the distance between DAPs, E_A and E_D are the donor and acceptor binding energies, respectively. The last term accounts for the Coulombic interaction between the ionised donor and ionised acceptor pairs involved in the radiative DAP recombination transition. For the overlap between the wave functions of the donor and acceptor to be significant, r is typically less than ~ 2.5 nm.[181] Using this value and E_D = 48 meV, equation 5.2 results in $E_A \approx 169$ meV, which confirms that the N acceptor level in MgZnO:N is deeper than in ZnO:N as estimated above. With increasing the excitation power density from 0.1 to 3 kW/cm^2 (see figure 5.8(a)), the DAP blue shifts about ~ 8 meV, which originates from the saturation of distant pairs with long lifetimes and a redistribution of the DAP recombination to closer pairs with a larger Coulombic interaction. The power density excitation data are further analysed using the power-law model, $I_{PL} \propto I_{laser}^k$, where I_{PL} is the integrated PL intensity and I_{laser} is the laser intensity. The log-log plots based on the power-law model are displayed in figure 5.8(b), which

yields a power-law exponent $k \approx 1$ within the experimental error of the measurement for both the ZnO FX and MgZnO DAP bands. The linear dependence of the FX on excitation density is expected because of the fast excitonic recombination lifetimes, typically < 1 ns.[182] However, with DAP recombination a sub-linear power-law exponent is generally expected due to saturation of the deep-level defects involved in the radiative transition. The linear DAP intensity dependence on excitation density observed for the MgZnO:N indicates that the deep level is not saturated under our excitation regime, which suggests the presence of a relatively high concentration of N acceptors.

Our NEXAFS studies reported above reveal the existence of several chemical states of N-related defects that are possible candidates for the deep acceptor in the 3.45 eV DAP transition observed in the MgZnO:N sample. N is an amphoteric impurity in ZnO and can act, therefore, as either a donor or an acceptor impurity. Indeed, our NEXAFS results shown in figure 5.2 reveal the incorporation of both types of dopants in MgZnO:N. Here, the P1 and P2 peaks are attributed to the presence of N_2 molecules and N_O acceptor states, respectively, while the P3 and P4 resonances were assigned to substitutional N on Zn sites, which act as donors. The significant concentration of these donor centres in the MgZnO:N sample is probably due to non-equilibrium PLD growth conditions at relatively low temperatures. In ZnO, isolated N_O is a deep acceptor, with the (0/-) level 1.3 eV above the valence band maximum,[183] thus this state is clearly too deep to act as an acceptor in the 3.45 eV DAP emission. It has been proposed that the N_O-V_{Zn} complex could produce a shallower defect level at 160 meV; however, such a complex would be thermodynamically unfavourable in low-temperature PLD growth as there is a huge potential barrier of 1.1 eV to its formation.[184] $(N_2)_O$ is a shallow donor, which cannot explain the acceptor involved in the observed DAP emission. In contrast, when occupying a cation site, $(N_2)_{Zn}$ has been predicted to be a shallow double acceptor with a binding

energy of ~ 120 meV,[185] and would be deeper by ~ 22 meV in $Mg_{0.16}Zn_{0.84}O$ due to the downward shift of the MgZnO valence band-edge relative to that of ZnO.[179] These results, coupled with our observation that N_2 is the dominant state in the MgZnO:N, make the $(N_2)_{Zn}$ state the most likely candidate for the acceptor in the 3.45 eV DAP emission. Given the fact that NEXAFS is highly sensitive to the local bonding environment of N in the lattice. The similarity of the P1 peak energy in the MgZnO:N NEXAFS spectrum to other molecular N_2 peaks previously recorded in nitrides and oxides (such as GaN, InN and ZnO)[169] suggests that N_2 molecules in MgZnO:N are only weakly bound to the lattice.

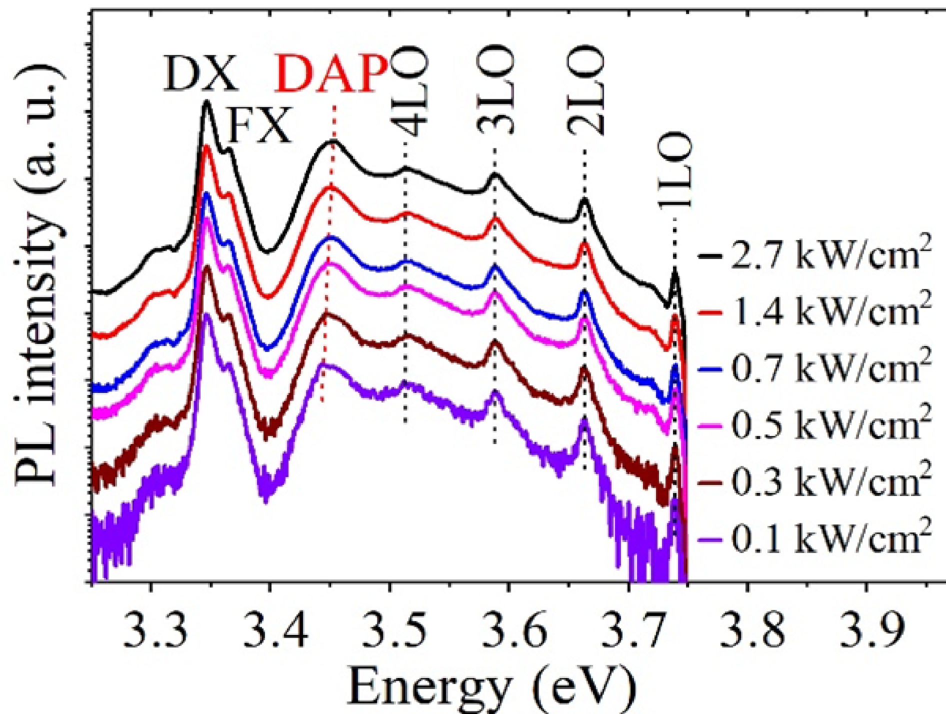

Fig. 5.7: Excitation power-dependent or power-resolved PL spectra of the MgZnO:N epilayer at 80 K for excitation power densities ranging from 0.1 to 2.7 kW/cm^2. The MgZnO:N DAP peak gradually blue shifts with increasing excitation density, while the FX(ZnO), DX(ZnO) and RRS peak positions remain unchanged.

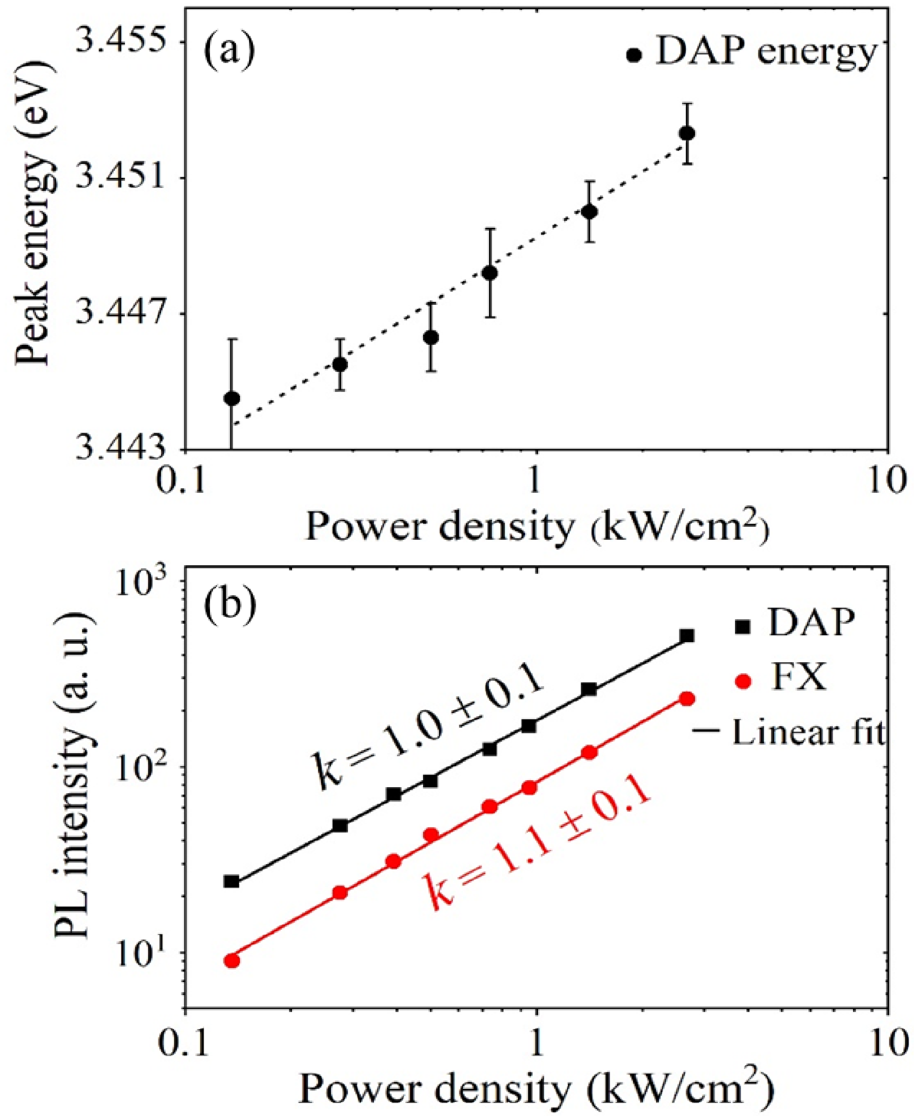

Fig. 5.8: (a) Small blue shifting of the DAP peak position by ~8 meV over the measured power density range is characteristic of DAP emissions. (b) Log-log plot of the ZnO FX and MgZnO DAP integrated intensities as a function of excitation density. The lines are the fits to the power-law model $I_{PL} \propto I_{laser}^{k}$ with a power exponent k = 1.0 and 1.1 for the DAP and FX emissions, respectively.

5.6. Conclusions

MgZnO epilayers (with 16 at% Mg) grown from a MgZnO target in a molecular N ambient showed N doping to a level where its’ chemical states could be measured by NEXAFS. Such a large dopant concentration was achieved by growing epitaxial MgZnO on ZnO buffer layers using relatively low-temperature PLD which favours the incorporation of N. Four-point electrical measurements revealed a significantly increased resistivity compared with MgZnO:O and MgZnO:vac layers grown under similar conditions. PL spectroscopy revealed an N-related 3.45 eV DAP band that was absent in MgZnO epilayers grown in an oxygen atmosphere or vacuum and which had exhibited comparable NBE emission. The DAP band in MgZnO is located at 160 meV below the band-edge emission at 3.61 eV and has an activation energy of 48 meV. It was found that N dopants exist mostly in the molecular state, which weakly bonds to the MgZnO lattice. Based on the experimental evidence, it is suggested that the DAP in MgZnO:N is due to radiative recombination involving deep $(N_2)_{Zn}$ acceptors and shallow donors and that the relatively high concentration of deep $(N_2)_{Zn}$ acceptors acts to effectively compensate the predominant n-type conductivity and thus render the MgZnO:N layers significantly more resistive.

Chapter 6

6. Two-dimensional ZnO Nanosheets

This chapter reports the results of ZnO 2D nanosheets. In this work, correlative optical and structural analysis of few-atomic-layer ZnO nanosheets fabricated through multistep soft-chemical exfoliation process was conducted. To date, excitonic emission in ZnO 2D nanosheets remains unexplored despite the fact that this scientifically important semiconductor has been widely used in devices. Microscopic and Raman investigation reveals superior crystalline quality of the nanosheets, compared with the parent material prior to exfoliation, which leads to the exploration of the quantum confinement of excitons and phonon coupling within single 2D nanosheets. CL and PL studies demonstrate a strong thickness-dependent quantum confinement effect in ZnO 2D nanosheets, which leads to significant variations in the excitonic and defect properties of the nanosheets. The novel optical properties of ZnO 2D nanosheets could have a great potential in a range of optoelectronics and emerging quantum devices applications.

6.1. Introduction

Two-dimensional (2D) materials like graphene and TMDs atomic level nanosheets has opened the door in other potential anisotropic materials with weak inter-layer bonds and strong in-plane bonds.[186, 187] Different types of 2D layer semiconductor materials including wide band gap (like h-BN, ZnO and Ga_2O_3)[188-190] and narrow band gap (like MoS_2, $MoSe_2$, WS_2, and InSe)[187, 191] with stable properties

under ambient conditions have been studied and shown to be useful for future nano-optoelectronics. Further interest in 2D materials is motivated by the possibility of combination of different types of nanosheets that leads to 2D nanodevices such as heterojunction diodes, memory devices and field-effect transistors with high switch on/off ratios.[187] Among all semiconductors, ZnO have large exciton binding energy (60 meV) and small electron effective mass, leading to stable excitons in ZnO at room temperature. ZnO is an efficient light emitting material with high UV luminescence at room temperature and attractive optoelectronic properties could offer opportunities for innovative device applications in photonics and optoelectronics.[192] Despite all other properties, ZnO have wurtzite crystal structure, and each Zn or O atom has four nearest neighbours with a strong in-plane bonds along the (0001) surface compared with a weaker out-of-plane bonds. This anisotropic crystal structure intrinsic characteristic suggests that ZnO can be exfoliated into nanosheets.

In this chapter, few-atomic-layer electronic-grade ZnO nanosheets with several microns lateral dimensions fabricated by a soft liquid-phase exfoliation method have been demonstrated. This fabrication method is highly suitable for modern device fabrication and capable of producing 2D nanosheets with excellent optical properties. These fabricated nanosheets with different thicknesses exhibit unique excitonic and structural characteristics. More interestingly, compared with the parent bulk ZnO, the fabricated ZnO nanosheets exhibit an enhanced exciton-photon coupling strength manifested in the emergence of LO phonon replicas in the excitonic luminescence spectrum and 2D exciton quantum confinement. Remarkably, the optical property of the ZnO nanosheets bears a close resemblance to that of highest quality ZnO epilayers by MBE growth. [193] The 2D quantum confinement effect of excitons in ZnO nanosheets have strong correlation

with the thickness of nanosheets, which have been confirmed by single-nanosheet CL probing technique.

6.2. Structural and Morphological Properties

XRD and Raman scattering spectroscopy were used for structural properties, while AFM, SEM and TEM are used for morphological analysis. The following section demonstrate the structural and morphological properties of ZnO 2D nanosheets and parent bulk microparticles sample. A schematic view of the arrangement of Zn and O atom in single monoatomic layer of ZnO is shown in figure 6.1.

6.2.1. Structural Properties

XRD diffraction pattern are shown in figure 6.2(a) for both ZnO parent microparticles and their extracted exfoliated 2D nanosheets. The X-ray measurements were conducted by CuKα radiation for a 2θ range of Bragg diffraction angle from 30 to 40 degrees. Analysis of XRD pattern of the soft-exfoliated nanosheets prepared on a Si wafer shows pure ZnO phase with all diffraction peaks $(10\bar{1}0)$, (0002) and $(10\bar{1}1)$ are related to ZnO and no other impurity phases are observed. This result shows the wurtzite hexagonal structure of the parent ZnO microparticles is well maintained during the exfoliation process and same diffraction peaks appears for ZnO nanosheets. Interestingly, the exfoliated nanosheets have preferential surface orientation along the [0001] zone axis, as indicated by the increase of the (0002) XRD peak intensity. This reflects that the ZnO parent microparticles favourably split along the basal c-plane during the soft-exfoliation process. The increase in (0002) peak intensity for 2D nanosheets is due to the improvement in (0002) crystal planes orientation after exfoliation and slight redistribution of grains.

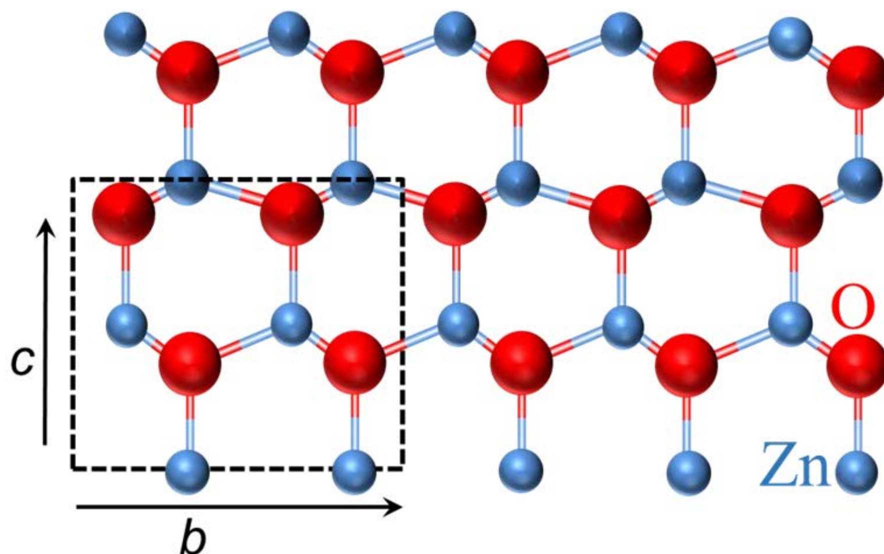

Fig. 6.1: Schematic representation of atomic arrangements of Zn and O in a single monolayer ZnO by repeating the unit cell in an appropriate crystal plane direction.

Figure 6.2(b) shows the micro-Raman spectra in backscattering geometry for ZnO parent microparticles and soft-exfoliated nanosheets on a Si wafer to further study of structural quality and defects analysis. The typical wurtzite Raman modes of ZnO in both parent sample and 2D nanosheet shows and confirms that wurtzite crystalline quality are well maintained after exfoliation processes. As the 532 nm laser penetration depth (*i.e.* ZnO is transparent for 532 nm wavelength) is considerably higher than the ZnO nanosheets thickness, so an intensive peak appears at 520 cm^{-1} from the Si wafer. Also, the Si peak intensity is higher in 2D nanosheets compared with the parent microparticles due to difference in the thickness of both target samples. Several other Raman peaks at 331, 378 and 438 cm^{-1} relate to intrinsic E_2(high) – E_2(low), A_1(TO) and E_2(high) mode of wurtzite structure for ZnO, respectively, while the peaks at 407 and 582 cm^{-1} correspond to oxygen vacancies (V_O) and zinc interstitial (Zn_i), respectively.[194, 195] Both parent sample and 2D nanosheets have strain-measure Raman E_2(high) peak at 437.8 ± 0.5 cm^{-1}, showing that no significant crystal structure strain was produced in atomically thick ZnO nanosheets. The most remarkable feature is the reduction in

intensity of the two 407 and 582 cm^{-1} intrinsic defect-related Raman modes, showing a large improvement in crystal structure quality as a result of exfoliation process. This study shows exciting and unique results regarding its high crystalline structure, because the liquid-phase exfoliation technique is currently debated as potentially less-viable routes compared with physical routes for the fabrication of high-quality electronic-grade 2D materials. These results leads to the conclusion that by soft liquid-phase exfoliation methods that employ mild low-energy sonication conditions, high-quality atomically thick ZnO 2D crystals can be achieved.[196]

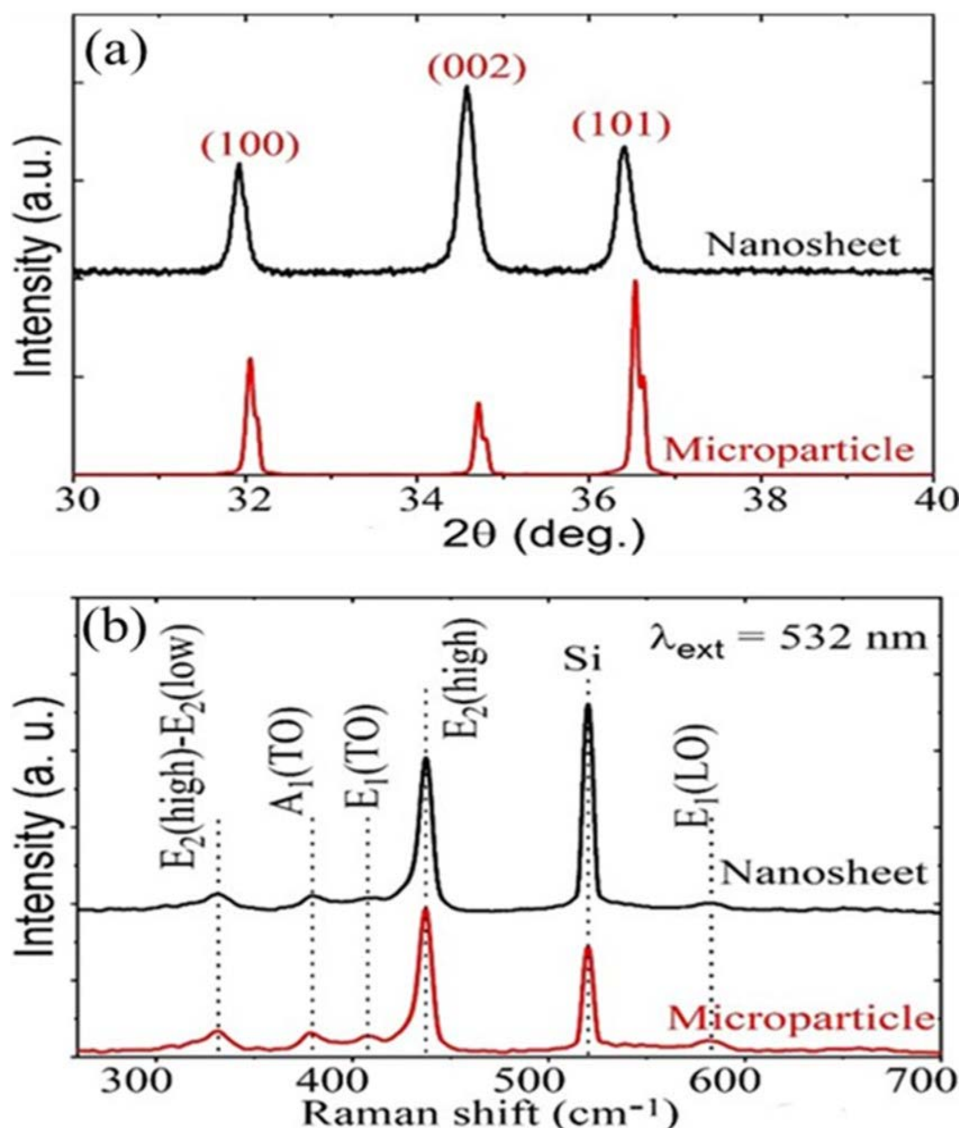

Fig. 6.2: (a) XRD spectra of ZnO 2D nanosheets and its parent microparticles with all the diffraction peaks indexed by the wurtzite crystalline phase (JCPDS 36-1451). There is no impurity phase observed but the (0002) peak or c-plane orientation is enhanced for the exfoliated ZnO nanosheet. (b) Raman scattering spectra of ZnO nanosheets and microparticles at room temperature confirming the wurtzite crystal structure and reduction in the intrinsic defects in exfoliated nanosheets.

6.2.2. Morphological Properties

Figure 6.3(a and b) shows the SEM image of the parent ZnO microparticles sample, and figure 6.3(c and d) shows the TEM image of exfoliated single 2D nanosheet. The electron microscopy images clearly reveal the successful fabrication of ZnO 2D nanosheets through chemical exfoliation process. These images show a clear transformation from faceted microparticles (having diameters in the range of 0.5 – 5 μm) to ZnO 2D nanosheets of hundreds of nm to several μm in lateral dimensions. Moreover, the stacking and layering of ZnO 2D nanosheets is evident from subtle changes in contrast, which relates to different thickness regions. The similar lateral dimensions of parent ZnO microparticles and exfoliated nanosheets is further support the importance of low sonication energy-based soft liquid-phase exfoliation strategies to fabricate 2D materials.[196] The EDX technique was used for qualitative determination of compositional purity and spatial distribution. Here in figure 6.4, the EDX results and their corresponding elemental mapping of ZnO nanosheet reveals Zn and O elements signatures without any impurity phases, confirming the compositional purity of the exfoliated 2D nanosheets.

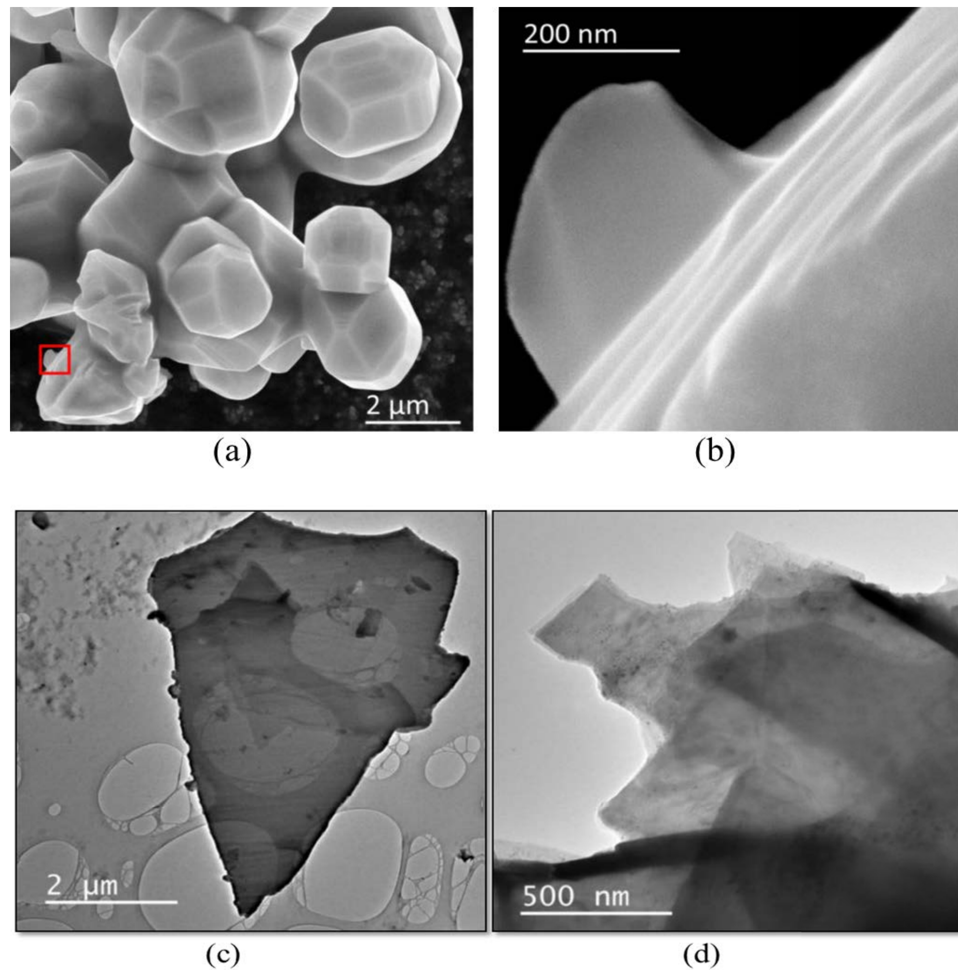

Fig. 6.3: Morphological characterisation of parent ZnO microparticles and exfoliated nanosheets; (a) SEM of the parent faceted ZnO microparticles; (b) corresponding image of small area (red square) in (a) representing the structural layered susceptible to exfoliation. (c,d) TEM images of ZnO 2D nanosheets shown under two different scale bars. The TEM images demonstrate that the nanosheets have lateral dimensions similar to those of parent microparticles.

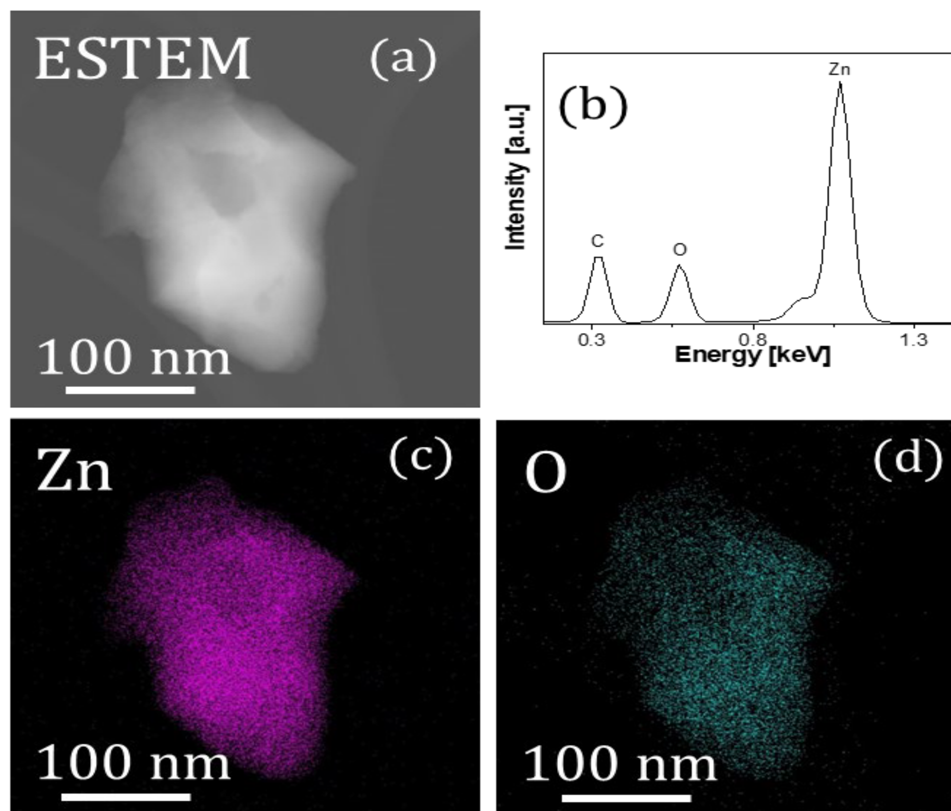

Fig. 6.4: EDX spectrum and elemental maps of a nanosheet showing signatures corresponding to Zn and O X-ray energy edges. This result supports the compositional purity and uniform spatial distribution throughout the soft-chemical exfoliated ZnO nanosheets. The observed C X-ray peak in (b) arises from the carbon-coated TEM grid.

To study the morphological properties of 2D nanosheet of varying thicknesses; centrifugation of ZnO nanosheet suspension at 500, 5,000 and 18,000 g rotating speed and then probed by TEM and AFM characterisation. All the TEM and AFM micro-images of single ZnO 2D nanosheet are shown in figure 6.5. ZnO with lowest centrifugation speed of 500 g are relatively thick and their thickness typically being tens of ZnO monolayers, as expected. An increase in centrifugation speed to 5,000 g, the resulting ZnO nanosheet is in the order of ten monolayers thickness. To further increase the centrifugation speed to 18,000 g, heavier flakes (thicker and larger) are gradually

eliminated from the solution and the acquired suspension will mainly composed of few-atomic-layer 2D nanosheets. The progressive reduction in nanosheets thickness to less than 10L (where L is the thickness of one ZnO monolayer) with increasing *g*-force can be seen from TEM image contrast and AFM images of corresponding ZnO nanosheets dispersed on a mica substrate from the size-selected suspensions. Therefore, few-atomic-layer nanosheets can be obtained using the highest centrifugation speed of 18,000 *g*.

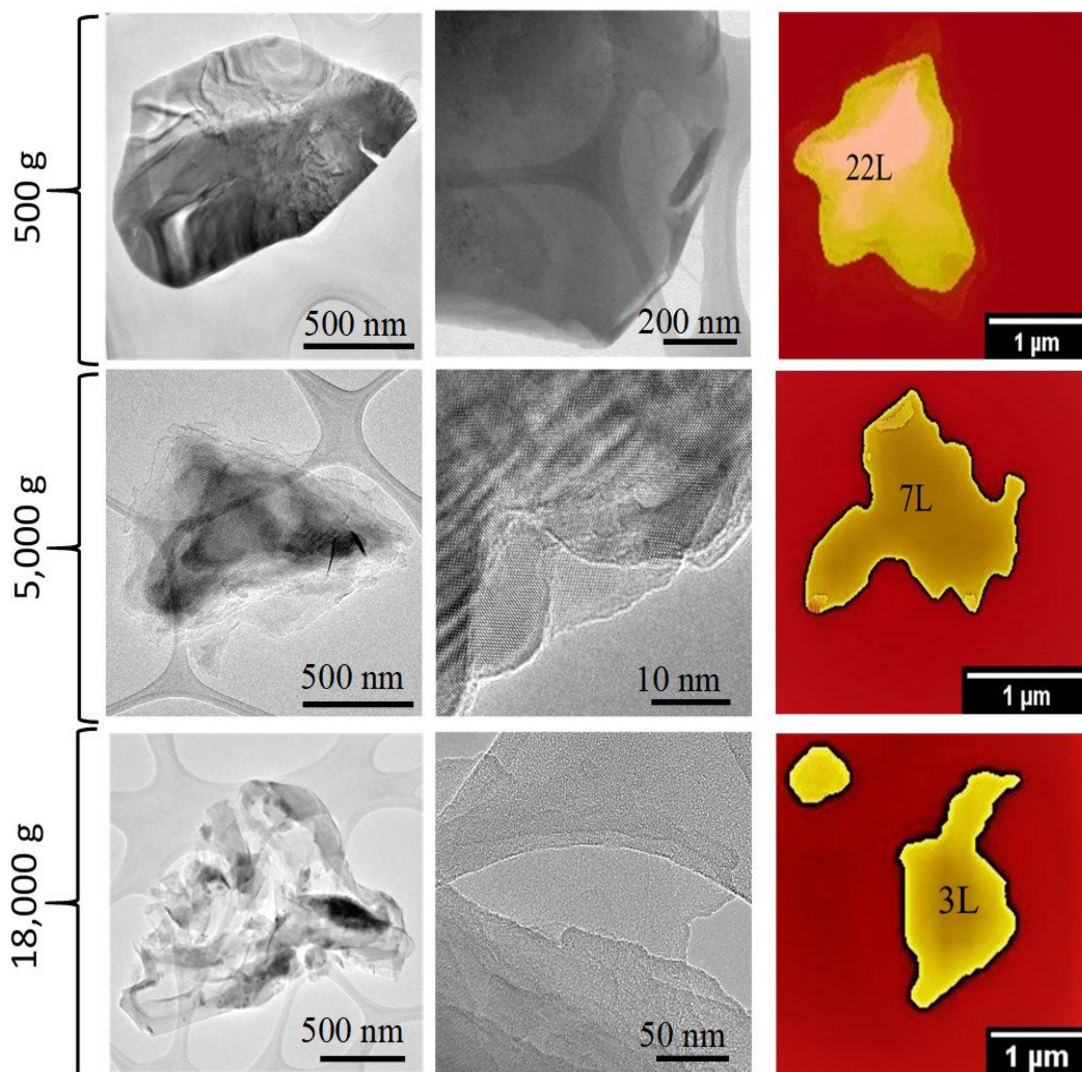

Fig. 6.5: TEM and AFM micro-images of a ZnO single nanosheet prepared from three different suspensions at centrifugation speeds of 500, 5,000 and 18,000 g. Both image measurements were performed on individual nanosheets by drop-casting onto TEM grids and mica substrates. Increasing the centrifugation speed of suspension enables isolation of reduced thickness for a series of samples. As can be seen in the AFM and TEM images, the lateral dimension is predominantly in the 0.5–2-μm range, consistent with the average size of the parent ZnO microparticles, while the thickness progressively decreases with increasing *g*-force. AFM images shows 3L, 7L and 22L nanosheet thickness, where L is one monolayer of ZnO and equal to 0.52 nm.

6.3. Optical Properties

Optical properties of three different sized selected ZnO nanosheets suspension have been determined by employing a standard optical spectrometer coupled with an integrated sphere. Nanosheets of reasonably uniform thickness can be obtained by progressive centrifugation of the exfoliation product at increasing g-forces. Three different ZnO nanosheet suspensions were obtained at 500, 5,000 and 18,000 g centrifugation speeds; their AFM images are shown in figure 6.6 (a-c). As expected, ZnO nanosheets obtained at a low centrifugation speed (500 g) are generally thick, with their thickness typically in excess of 14 monolayers. By increasing the centrifugation speed to 5,000 g, thicker nanosheets were progressively eliminated and the suspension is composed of nanosheets with thickness less than 10 monolayers. Those nanosheets obtained at the g-force of 18,000 are atomically thin nanosheets with thickness 2-6 monolayers. Figure 6.6 (d-f) shows the extinction (ε), absorption (α) and scattering (σ) coefficient spectra of exfoliated ZnO nanosheets suspensions obtained at centrifugation speeds of 500, 5,000 and 18,000 g. For each of the resultant nanosheet dispersions, the extinction coefficient spectra were measured in a standard optical spectrometer and then the absorption spectra using an integrating sphere. The extinction spectra were obtained from transmission ($T = 10^{-\varepsilon Cl}$), where ε is the molar extinction coefficient, C the molar concentration of ZnO, and l the cuvette path length. The acquired extinction (ε) coefficient spectra, which incorporate the contribution of both absorption (α) and scattering (σ) term for soft-exfoliated ZnO nanosheets according to the well-known relation: ε(λ) = α(λ) + σ(λ). To investigate relative analysis of ε, α and σ coefficient separately for ZnO nanosheets with three different g-speed, relative spectral graphs are presented in figure 6.6(d-f). The suspension of exfoliated nanosheets resulted from

18000 *g* configuration displays extremely high extinction coefficients in the UV region, which progressively reduces as the nanosheet thickness increases. As extinction coefficient includes both absorption and scattering. For small nanoparticles suspensions, the scattering is weak, and the extinction is almost equal to absorption. On the other hand, the extinction coefficient from nanosheets with high aspect ratio has strong possible contributions from wavelength dependent scattering.[197, 198] Moreover, the non-resonant light scattering from 2D nanosheets with high aspect ratio is different from small nanoparticles suspension. The light scattering profile of ZnO nanosheets of different thickness is also consistent with recent findings for nanosheets of other wide-bandgap semiconductors that show highly efficient light scattering from high aspect ratio nanosheets in the non-resonant regime. [199] This further confirms the success of the size-selection approach to produce ultrathin ZnO 2D nanosheets. The ultrathin nanosheets from 18000 g have over 60 times higher UV absorption capacity.

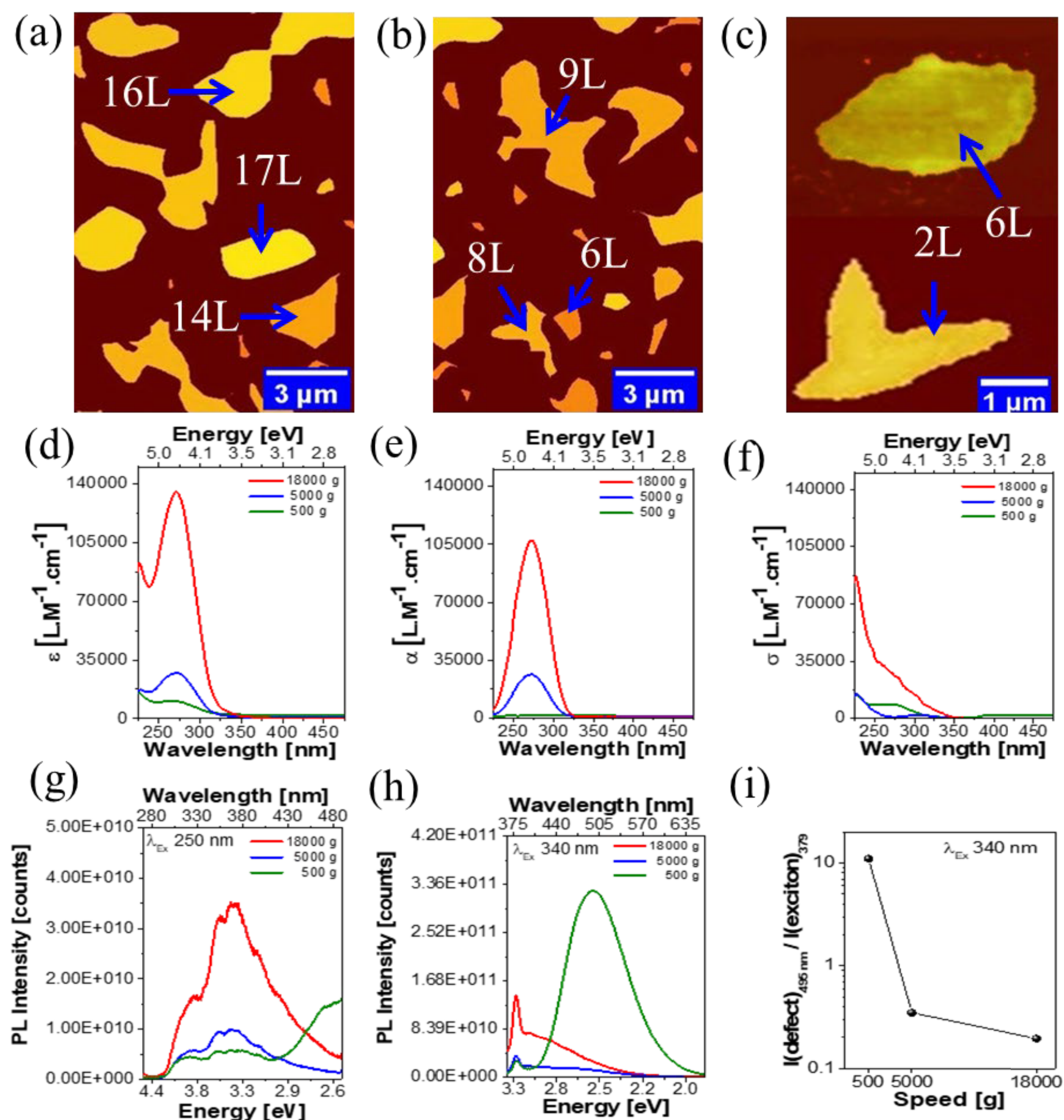

Fig. 6.6: (a, b, c) AFM images of an exfoliated ZnO nanosheets with their corresponding nanosheet thickness range, acquired at three centrifugation speeds of suspension (see table 6.1). Spectra of (d) extinction coefficient ε, (e) absorption coefficient α and (f) scattering coefficient σ for three different exfoliated ZnO suspensions. (g, h) PL spectra by the laser excitation wavelengths of 250 nm and 340 nm, respectively. PL spectra show an emergence of the excitonic peak at 3.27 eV (379 nm) and suppression of the V_O-related defect emission band at 2.5 eV (495 nm) along with an increasing of quantum

confinement in ZnO nanosheets acquired via increasing *g*-force. (i) PL intensity ratio I(defect)/I(exciton) as a function of centrifugation speed (*g*).

Table 6.1: ZnO 2D exfoliated nanosheets with corresponding thickness ranges.

ZnO Nanosheet (Centrifugation speed)	**Thickness range**
500 g	≥14*L*
5,000 g	≤9*L*
18,000 g	2–6*L*

6.3.1. Photoluminescence Spectroscopy Analysis

PL properties are shown in figure 6.6(g and h) and their defect intensity ratio are in figure 6.6(i). One inherent limitation of liquid-phase exfoliation technique is that the exfoliated product contains a mixture of nanosheets of different thickness and lateral dimensions. The cumulative PL characteristics emission of ZnO nanosheets suspension for three different centrifugation speed by using two laser source (250 and 340) nm, are shown in figure 6.6 (g and h). Two peaks were observed by the excitation of 340 nm laser wavelength under same probing conditions. The first narrow peak at 3.27 eV in the UV range is the typical NBE emission associated with excitonic recombination, and the second peak, which is much broader, at 2.5 eV (495 nm) can be related to oxygen vacancy (V_O) related defects.[200] Thick ZnO nanosheets, obtained at a low centrifugation speed of 500 g, exhibit a dominant defect emission due to a high concentration of V_O defects, resembling the bulk state of ZnO. On the other hand, thin nanosheets obtained at high

centrifugation speeds (>5,000 *g*) exhibit only the UV band while the defect emission intensity remarkably decreases by over 50 times at the highest centrifugation speed (figure 6.6(i)), consistent with the Raman spectroscopy results. This observation is attributed to a lower concentration of point defects, as vacancy defects in the thinner ZnO nanosheets can potentially diffuse efficiently to the nanosheet surface during processing and be eliminated, so improving the optoelectronic quality. The reduction in defects in ultrathin 2D materials during chemical soft-exfoliation has not been reported in other materials to the best of our knowledge. However, it is believed that the observed phenomenon in ZnO 2D nanosheets is reminiscent of the inherent strain relaxation and defect diffusion property of ZnO nanostructures.[201] Therefore, the observed PL response reveals that ultrathin layers of ZnO 2D nanosheets shows significant enhancement of UV excitonic emission over their thicker nanosheets counterparts.

6.3.2. Cathodoluminescence Analysis of Single ZnO Nanosheet

The excitonic luminescence characteristics of soft-exfoliated ZnO nanosheets were further investigated individually by a combination of AFM and transmission-mode CL technique. The ZnO nanosheet sample for both AFM and CL probing taken at the same time from suspension and simultaneously drop-casted with equal drops from micropipette on mica sheet for AFM and carbon-coated copper TEM grid for CL measurements. As shown in figure 6.6(a-c), a variety of ZnO nanosheets with the lateral dimension in the micron range and thickness down to 3*L* were acquired after being separated at a centrifugation speed of 18,000 g. To clearly show the 2D single-nanosheet thickness, a single AFM image with corresponding height *z*-profile of a typical nanosheet, which has an average thickness of 8.5 ± 0.4 nm, and 2.6 ± 0.4 nm corresponding to 17*L*

and 6*L*, were presented in figure 6.7(a and b), respectively. The AFM images indicate that the exfoliated nanosheets are smooth on the atomic scale with an average surface roughness significantly smaller than the thickness of one monolayer (as determined from the z profile). The thickness of one monolayer ZnO is equal to 0.52 nm.

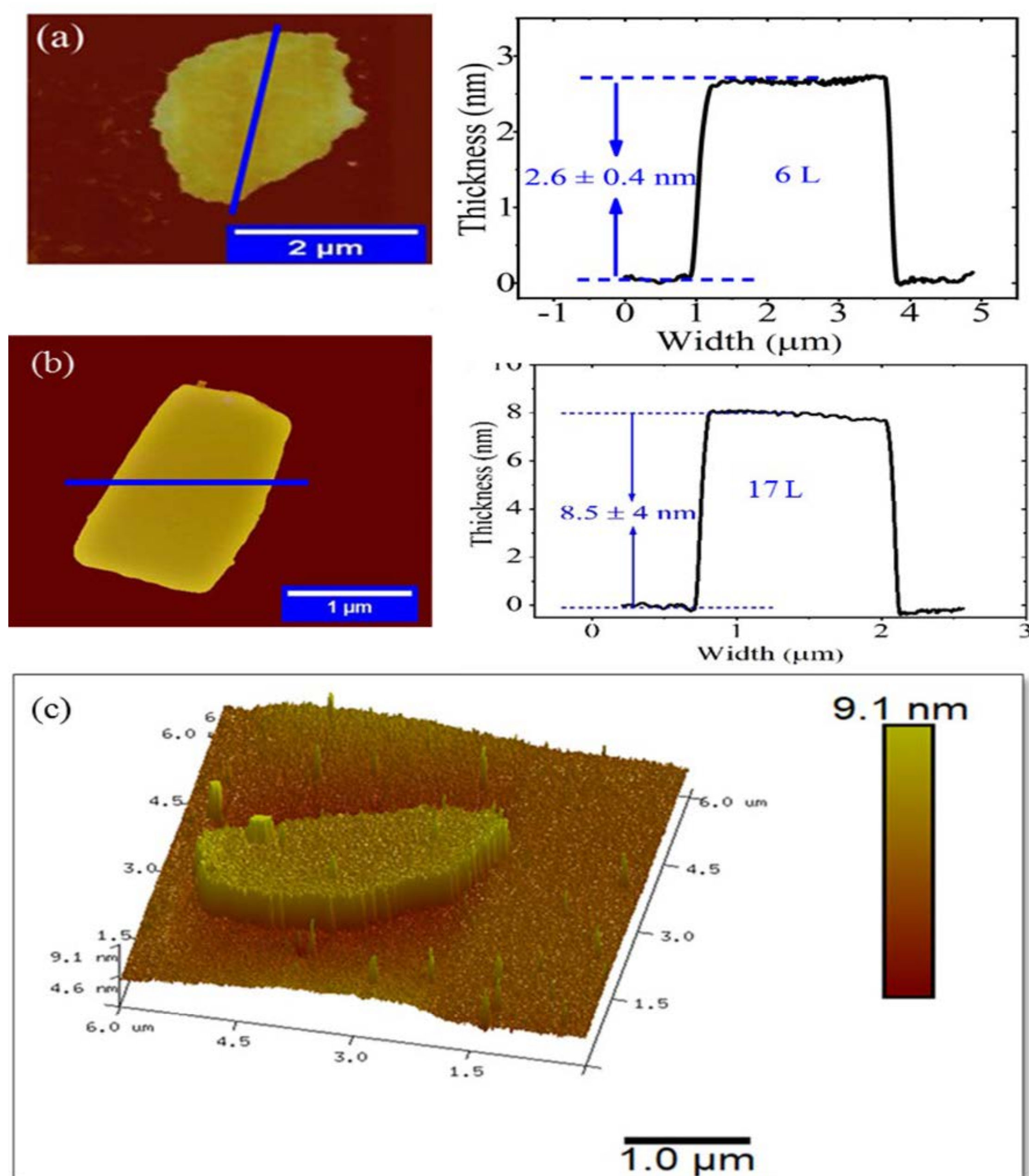

Fig. 6.7: AFM image of a single thin nanosheet with a thickness of (a) 6 *L* and (b) 17 *L* (*L* = 0.52 nm), together with their height profile using a line scan. (c) Three-dimensional (3D) AFM image of a typical nanosheet at micrometre (μm) scale range along the *x*- and

y-axis (lateral dimension) and at nanometre (nm) scale range along the *z*-axis (i.e. nanosheet thickness).

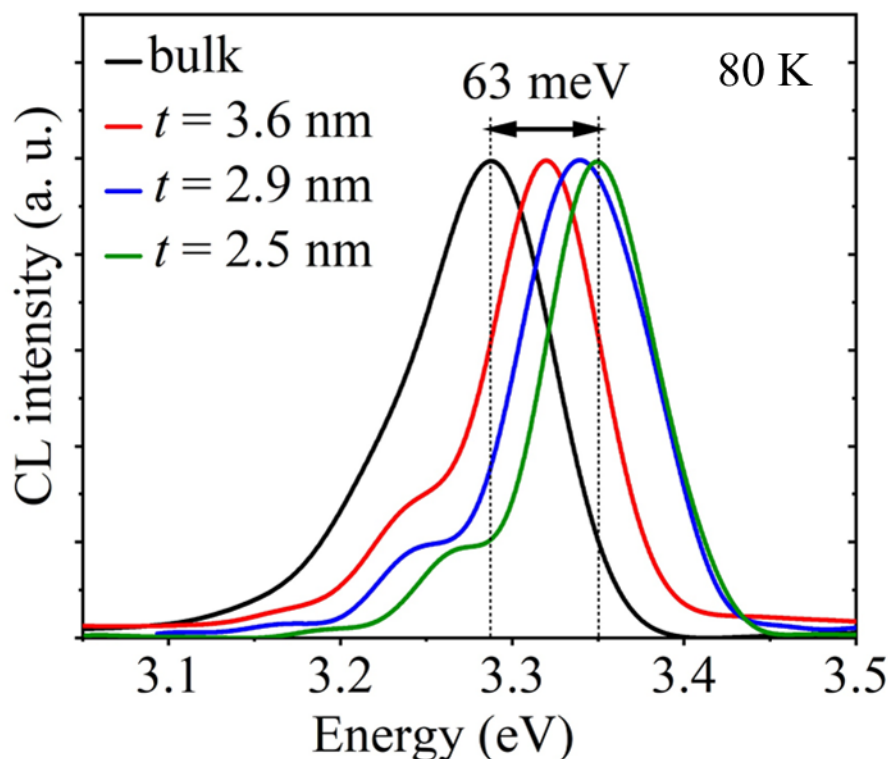

Fig. 6.8: CL spectra acquired from individual exfoliated nanosheet and parent ZnO microparticle (bulk) at 30 kV e-beam accelerating voltage, showing a gradual blue shift of the exciton emission with decreasing nanosheet thickness up to 2.5 nm, consistent with the quantum confinement of excitons.

The CL spectra at 80 K temperature acquired from individual nanosheets show a systematic blue shift and spectral narrowing with decreasing nanosheet thickness down to ~ 2.5 nm, as shown in figure 6.8. The CL spectral results show that the excitonic peak energy of the ZnO 2D nanosheet monotonically increases as the nanosheet becomes thinner, reaching a maximum energy of ~3.35 eV. The difference between parent microparticle and 5 *L* nanosheet thickness excitonic peak energy is 63 meV. The peak intensity and positon of the CL emission from the nanosheets persists with continuing e-beam irradiation, indicating their high chemical stability

It has previously established that the exciton binding energy could increases significantly in semiconducting 2D materials due to reduced bulk dielectric screening as the electric field produced by an exciton can extend outside the 2D interfaces.[186, 189] For instance, the binding energy in the limit of an atomically thin WS_2 layer has been shown to be four times higher than that in the bulk WS_2.[186] However, an increase in the exciton binding energy would cause a red shift in the FX emission energy instead of a blue shift. Additionally, for the ZnO nanosheets studied in this work, any change of the exciton binding energy due to any alteration of the dielectric screening is expected to be small since the exciton Bohr radius in ZnO is 2.34 nm, which is smaller than the thickness of the thinnest measured nanosheet. Therefore, the observed increase in the FX recombination energy is attributed to the quantum confinement of excitons in the ZnO nanosheets and model this dependence on the nanosheet thickness, L, using a square quantum well potential of infinite height:

$$E_{2D} = E_{bulk} + \Delta E_{2D} = E_{bulk} + \frac{\pi^2 \hbar^2}{2L^2 m_{ex}} \quad (6.1)$$

where ΔE_{2D} is the exciton energy shift due to the quantum confinement effect, m_{ex} is the reduced effective mass of an exciton, E_{bulk} is the excitonic energy of bulk ZnO, L is nanosheet thickness and h is Planck's constant. Using the reported effective mass of electrons ($m_e = 0.23 m_0$) and holes ($m_h = 0.59 m_0$) for transportation along the *c*-plane of bulk ZnO crystals,[202] m_{ex} is estimated to be $m_{ex} = \left(\frac{1}{m_e} + \frac{1}{m_h}\right)^{-1} = 0.165\, m_o$, where m_o is the rest mass of electron. CL measurements locally taken at several spots within individual nanosheet show very slight variations in the excitonic spectrum. Using equation 6.1, AFM nanosheet thickness of $L = 2.6 \pm 0.2$ nm yields $\Delta E_{2D} = 280 \pm$

36 meV. This value is significantly smaller than the measured value of the CL peak shift (63 meV). The experimental values of ΔE_{2D} is deviated from the theory, suggesting that the real confinement potential of excitons in the nanosheet could be different to the hard wall potential used in the model. This could be due to the chemisorption of gas molecules on the ZnO surface, which enables carrier wave functions to penetrate into these impurity layers, increasing the effective quantum well width of nanosheets. The microparticles at 80 K exhibit a broad, asymmetrical exciton emission peaking at 3.29 eV due to the superposition of FX and its phonon replica, with the first replica (FX-1LO) being the major contribution to the asymmetrical peak shape of the NBE emission. [203]

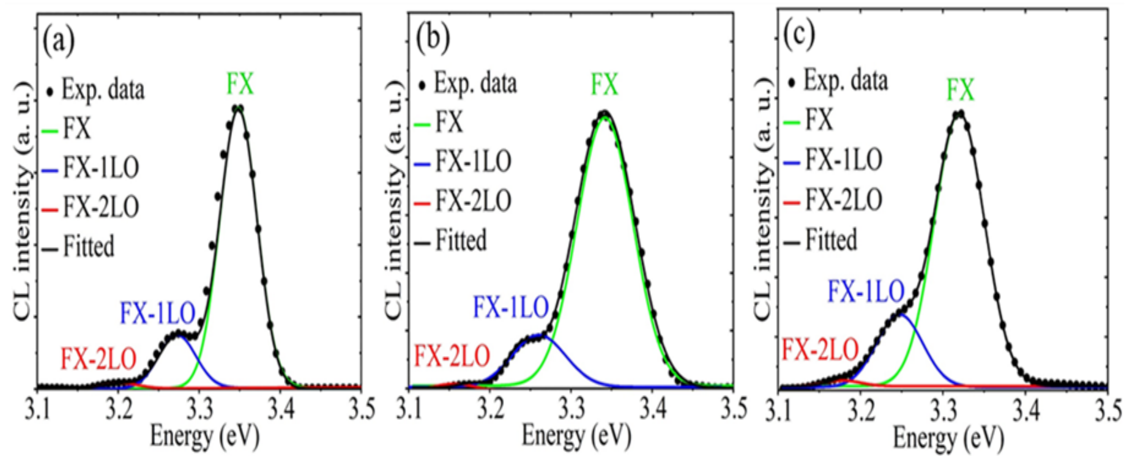

Fig. 6.9: Fitted spectra of experimental CL data points with a Gaussian function for three nanosheets; (a) 2.5 nm, (b) 2.9 nm and (c) 3.6 nm thickness with a free exciton (FX) component and its phonon replicas (FX-1LO and FX-2LO) for integral intensity determination.

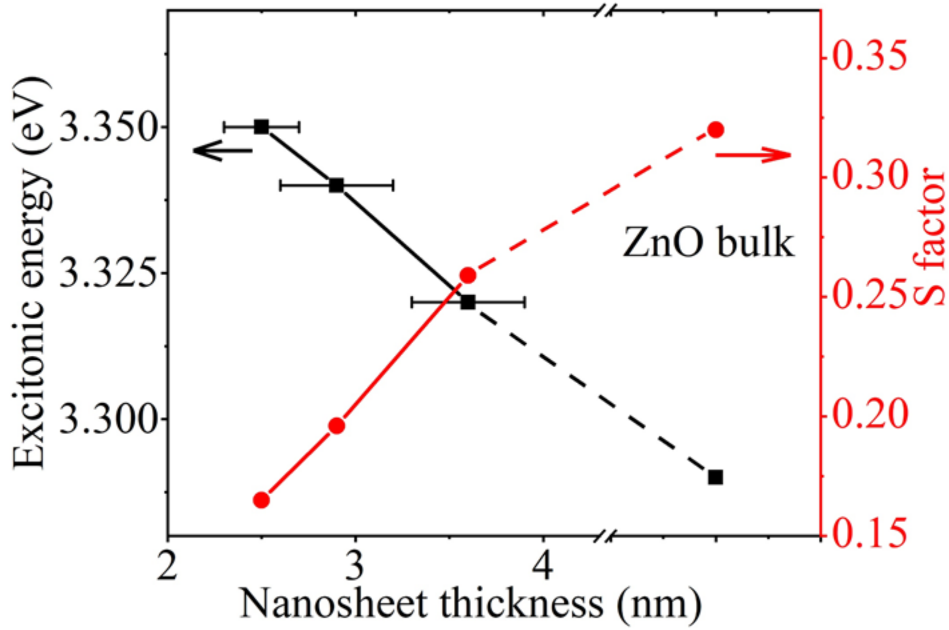

Fig. 6.10: FX photon energy (left y-axis) and Huang–Rhys phonon coupling factor *S* (right y-axis) as a function of nanosheet thickness. Here, the Huang–Rhys phonon coupling factor *S* is defined as the intensity ratio of FX-LO/FX.

The strength of electron-phonon coupling strength in ZnO is mainly governed by the Fröhlich interaction between electrons and LO phonons. The integrated intensities was analysed of the FX and its LO phonon replicas using the Poisson distribution ($I_n \sim \exp(-S)\frac{S^n}{n!}$, where I_n is the intensity of the *n*th replica),[204] and the Huang-Rhys factor *S* was empirically determined from the curve fitting and deconvolution of the excitonic CL spectra as shown in figure 6.9(a-c). Basically, Huang-Rhys factor *S* is a quantitative analysis of exciton-phonon coupling strength in the ZnO 2D nanosheet. The *S* value is found to increase with the nanosheet thickness in the range 0.17-0.25 (Fig. 6.10); these values are significantly smaller than the reported range of 0.35-0.6 for bulk ZnO crystals.[204] The weak coupling strength of excitons to LO phonons in the exfoliated ZnO nanosheets is consistent with a reduction in the defect density,[205] which

is confirmed by Raman spectroscopy as described above. Moreover, non-radiative decay of excitonic emission may happen due to defect-related energy states, which leads to a reduced effect on phonon emission intensity compared with free excitonic emission due to fast relaxation time of LO phonon. An alternative explanation is the effect of the quantum confinement whereby the exciton wave function becomes less polar, thus reducing its coupling strength with the polar ZnO lattice via the Fröhlich interaction.[206] However, further studies of exciton confining potential on the exciton-phonon coupling will be required.

6.3.2.1. Temperature-resolved Cathodoluminescence

The CL result of microparticles at 80 K exhibit a broad, asymmetrical exciton emission peaking at 3.29 eV due to the superposition of FX and its phonon replicas, with the first replica (FX-1LO) being the major contribution to the asymmetrical peak shape of the NBE emission.[207] Overall, the NBE emission of thin ZnO nanosheet is dominated by the FX emission at $T > 80$ K (since the contribution from bound excitons to the NBE emission would be significantly smaller as they are thermally ionised at this temperature), bearing close resemblance in spectral shape to those observed in ZnO epilayers and single crystals.[208] The strong FX emission in the thin nanosheets is attributed to the enhanced optical quality, which is supported by the reduction in the 582 cm^{-1} Raman mode peak (see figure 6.2b) and broad PL emission band at 2.5 eV both associated with V_O defects as shown in figure 6.6(i). The reduced spectral width of the excitonic emission and the emergence of clear phonon replicas are characteristic of enhanced crystalline quality in the ZnO nanosheets. Further, temperature-resolved CL analysis of ZnO nanosheet was carried out in a temperature range of 80 K to 160 K as shown in figure 6.11(a). For improved accuracy and reproducibility of the curve fitting for the CL spectra of the nanosheet, the peak energies of FX-1LO and FX-2LO as

functions of temperature were measured. Assuming a Gaussian line shape for the FX emission and considering the transition probability for phonon-assisted FX-1LO and FX-2LO replicas, their energy positions can be expressed as follows [209]:

$$E_{FX} - E_{FX-LO} = \hbar\omega_{LO} - \frac{3}{2}k_bT \quad (6.2)$$

$$E_{FX-LO} - E_{FX-2LO} = \hbar\omega_{LO} + k_bT \quad (6.3)$$

Here, E_{FX} is the FX transition energy, E_{FX-LO} and E_{FX-2LO} are the peak energy of the first- and second-order LO replicas, respectively. The value of $\hbar\omega_{LO}$ is 72 meV, while the energy separation between (FX and FX-1LO) and (FX-1LO, FX-2LO) will be 63 meV and 80 meV at 80 K, respectively. The above equations (6.2 and 6.3) describe the variations of the peak energy of the phonon replicas relative to the free excitons (FX) with temperature; these temperature-dependent separations between (FX, FX-LO) and (FX-LO, FX-2LO) were used as constraints in the curve fitting of the nanosheet. Since the FX emission is dominant in ZnO at T > 80 K, the Gaussian peak fitting of the nanosheet spectra could be reliably made with the FX component fitted to the high energy side of the excitonic emission spectrum of the nanosheets. This curve-fitting approach enables accurate determination of the intensities of the FX and its phonon replicas as a function of temperature, allowing the accurate evaluation of the thermal behaviour of excitons in the nanosheets. The Arrhenius plot of the FX integrated intensity, shown in figure 6.11(b), yields an activation energy of $E_a = 61.3 \pm 4.7$ meV, which is comparable to the exciton binding energy in bulk ZnO of 60 meV.[210] This result confirms the dielectric screening of excitons in the exfoliated ZnO nanosheets is negligibly weak.

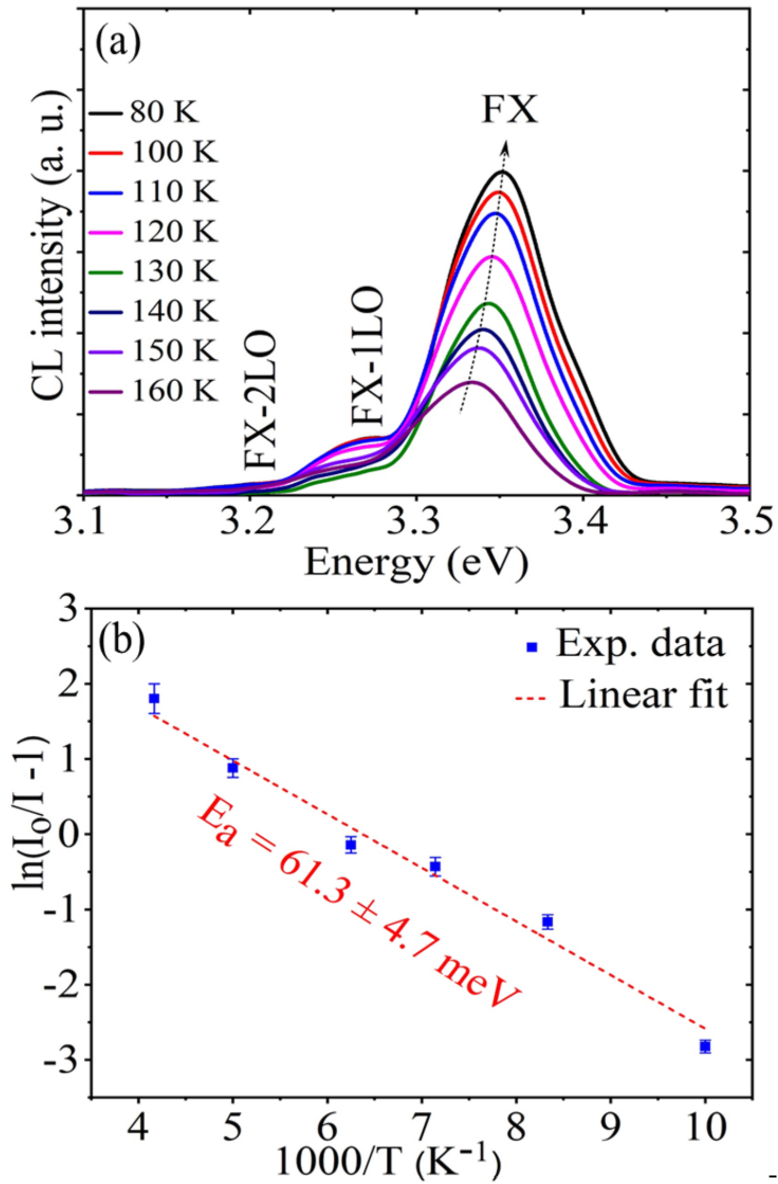

Fig. 6.11: (a) Temperature-resolved CL of ZnO exfoliated 2D nanosheet. (b) Arrhenius analysis of the FX-integrated intensity yielding E_a = 61.3 ± 4.7 meV, corresponding to the exciton binding energy in ultrathin nanosheets.

6.4. Conclusions

In summary, the structural and optical properties of ZnO ultrathin 2D nanosheets prepared through chemically soft-exfoliation method have been investigated. The 2D morphological properties of ZnO exfoliated nanosheets have been confirmed by AFM, SEM and TEM probing analysis. The XRD and Raman scattering analysis reveals that the nanosheets have maintained their wurtzite crystal structure with preferential orientation of c-plane after exfoliation synthesis process. After successful soft-exfoliation process of parent sample, the ZnO nanosheet shows high (0002) crystal plane orientation with the lateral dimension in micrometres. PL results shows that the ZnO nanosheets have the least defect-related emission as compared with microparticles bulk ZnO sample. The nanosheets shows enhanced optical quality relative to the original parent bulk material, as evidenced by the observation of strong free exciton and phonon replica emission peaks in the CL spectra. Single-nanosheet CL analysis reveals a quantum confinement effect with the shift of the excitonic emission consistent with the planar quantum confinement of excitons by the nanosheet interfaces. The temperature-dependent optical properties of the nanosheets indicate 2D excitons are bound with a binding energy of 61 meV.

Chapter 7

7. Conclusions and Future Work

7.1. Conclusions

In this thesis, ZnO and MgZnO nanostructures and heterostructures were thoroughly investigated. The current status and future perspectives of ZnO 2D nanostructures and MgZnO/ZnO heterostructures and their possible applications were reviewed. Three mini projects were conducted on MgZnO/ZnO MQWs, N-doped MgZnO epitaxial films and ZnO 2D nanosheets. Characterisation of these material systems were carried out via microscopic, optical and electrical techniques.

In the first project, the luminescence enhancement of MgZnO/ZnO MQWs was achieved using a rapid remote plasma annealing method. The optical properties of MQWs were strongly modified by the incorporation of H, while the crystal structure integrity was almost unaffected. The CL results show that H doping rapidly enhances optical emission by more than 10 times compared with the pristine MQWs, while defect-related emissions were eliminated. The CL analysis revealed that this remarkable increase in MQW optical emission was due to the passivation of both basal stacking faults and point defects.

The second mini project is concerned with the optical signatures of N acceptors in MgZnO epilayers. To this end, the PL properties of the MgZnO epilayers, which were grown using the low-temperature PLD in three different environments (O_2, N_2 and vacuum), were investigated. All these MgZnO epilayers displayed similar NBE emissions at around 3.61 eV. For the epilayer grown in nitrogen, a new 3.45 eV PL peak was

observed and attributed to nitrogen acceptors. This 3.45 eV peak was completely absent in the MgZnO epilayers grown in O_2 and vacuum, although their optical bandgaps and morphological properties were very similar. The chemical state of nitrogen acceptors in MgZnO was further examined by NEXAFS, revealing that nitrogen exists in four states (N_O, $(N_2)_{Zn}$, NO_2, and N_2O). From these results, it was suggested that the DAP emission was due to radiative recombination between a deep $(N_2)_{Zn}$ acceptor and a shallow donor. A relatively high concentration of nitrogen acceptors acts to effectively compensate n-type conductivity in the MgZnO epilayers, allowing a new route to control the electrical properties of MgZnO by nitrogen doping.

In the last project, ZnO 2D nanosheets were fabricated by the soft-chemical liquid exfoliation method and studied using high-resolution microscopic and optical techniques. Suspensions of ZnO nanosheets with different thicknesses were separated by centrifugation. The ZnO 2D nanosheets was investigated by AFM, SEM and TEM, revealing that nanosheets with thickness down to 3 monolayers could be obtained by this exfoliation method. XRD and Raman analysis revealed that the nanosheets retained their wurtzite crystal structure with preferential orientation of c-plane after the exfoliation. The PL results showed that the ZnO nanosheets had a lower defect-related emission compared with the parent microparticles. The strong free excitonic emission in few-layers 2D nanosheets demonstrated their high optical quality and a lower defect density compared with their parent microparticles. CL analysis of single-nanosheets revealed a quantum confinement effect with a shift in excitonic emission consistent with the planar quantum confinement of excitons by the nanosheet interfaces.

7.2. Future Work

ZnO-based heterostructures and nanostructures have potential applications in optoelectronics and nanoelectronics. The most controversial issue in ZnO applications is the lack of stable p-type ZnO, which is necessary for bipolar junction devices. As the solubility of nitrogen in ternary alloy MgZnO is higher than binary ZnO, which is required to produce a high concentration of acceptors. In this way, the properties of nitrogen acceptors in MgZnO alloy have been investigated. A new luminescence peak was observed, which is assigned to donor-acceptor-pair transition in MgZnO. Apart from optical emission related to nitrogen, the MgZnO is still n-type. Different approaches can be employed to prepare p-type MgZnO by nitrogen doping, such as Mg alloying in ZnO and nitrogen dopant concentration, growth parameters, substrate selection, purity of the materials and post-treatment process. The development of p-type N-doped MgZnO can be achieved with the alloying of higher MgO contents into ZnO and low growth temperature that leads to enhancement of nitrogen concentration in MgZnO. Therefore, further study will be needed to explore the nitrogen deep acceptors, which may lead to the successful fabrication of p-type MgZnO.

Another important aspect of ZnO-based systems is the multilayer MgZnO/ZnO heterostructures. Different types of undesirable defects limit the optical emission of MgZnO/ZnO multiple quantum wells. A new approach was developed to passivate the defects and enhance the MQWs optical emission. The RRPA approach for the hydrogen incorporation in MgZnO/ZnO MQWs has been used. MgZnO/ZnO MQWs were thermally treated for a range of hydrogen plasma irradiation times and compared with the pristine MQWs sample. The introduction of hydrogen in MgZnO/ZnO MQWs using the RRPA technique results in significant enhancement of the MQW optical emission and

eliminates the defect-related emissions. Other interesting bilayer (MgZnO/ZnO) structures grown on single crystal ZnO substrates are still under investigation. These samples exhibit 2DEG behaviours. The optical study of these MgZnO/ZnO bilayer heterostructures on three different planes oriented (a, m, and c-plane) ZnO single crystals are being investigated. The CL results are depicted in figure 7.1 for the three MgZnO/ZnO heterostructures along with three single crystals (a, b, c) -plane. A new luminescence peak at ~3.1 eV was observed in the a- and m-plane, while it is absent in c-plane bilayer heterostructures. The origin of this new luminescence peak is unknown at present. Further characterisations are needed to determine the exact nature of this new optical emission peak.

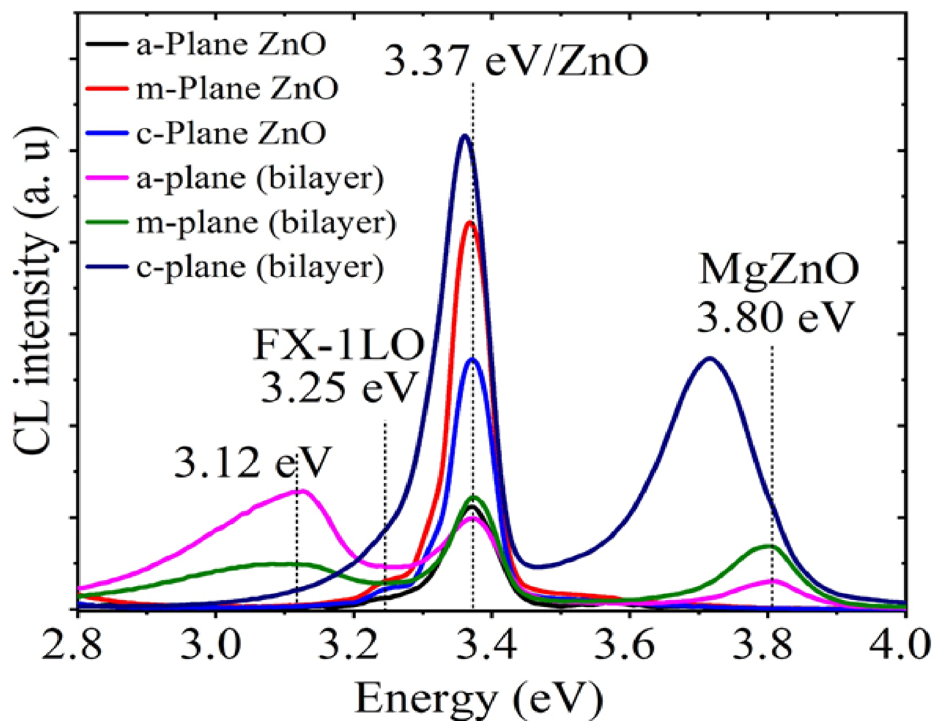

Fig. 7.1: CL spectra of three different homoepitaxial MgZnO/ZnO bilayers heterostructures grown on a, m, and c-plane ZnO single crystals. The bilayers on the a- and m-plane crystals show 2DEG related emission at 3.12 eV.

References

1. Özgür, Ü., et al., A comprehensive review of ZnO materials and devices. Journal of applied physics, 2005. 98(4): p. 11.
2. Fan, J.C., et al., p-Type ZnO materials: theory, growth, properties and devices. Progress in Materials Science, 2013. 58(6): p. 874-985.
3. Liu, J.-S., et al., MgZnO p–n heterostructure light-emitting devices. Optics letters, 2013. 38(12): p. 2113-2115.
4. Gai, Y., et al., Effect on nitrogen acceptor as Mg is alloyed into ZnO. Applied physics letters, 2008. 92(6): p. 062110.
5. Wei, Z., et al., Photoluminescence and acceptor level state of p-type nitrogen-doped MgZnO films. Journal of Materials Research, 2007. 22(10): p. 2791-2795.
6. Park, W.I., G.-C. Yi, and H. Jang, Metalorganic vapor-phase epitaxial growth and photoluminescent properties of Zn 1− x Mg x O (0⩽ x⩽ 0.49) thin films. Applied Physics Letters, 2001. 79(13): p. 2022-2024.
7. Fujihara, S., Y. Ogawa, and A. Kasai, Tunable visible photoluminescence from ZnO thin films through Mg-doping and annealing. Chemistry of materials, 2004. 16(15): p. 2965-2968.
8. Hwang, H.Y., et al., Emergent phenomena at oxide interfaces. Nature materials, 2012. 11(2): p. 103.
9. Janotti, A., et al., Controlling the density of the two-dimensional electron gas at the SrTiO 3/LaAlO 3 interface. Physical Review B, 2012. 86(24): p. 241108.
10. Zubko, P., et al., Interface physics in complex oxide heterostructures. Annu. Rev. Condens. Matter Phys., 2011. 2(1): p. 141-165.

11. Mannhart, J., et al., Two-dimensional electron gases at oxide interfaces. MRS bulletin, 2008. 33(11): p. 1027-1034.
12. Zakria, M., et al., Highly Luminescent MgZnO/ZnO Multiple Quantum Wells for Photonics Devices. ACS Applied Nano Materials, 2019. 2(4): p. 2574-2579.
13. Tsukazaki, A., et al., Quantum Hall effect in polar oxide heterostructures. Science, 2007. 315(5817): p. 1388-1391.
14. Georgiou, T., et al., Vertical field-effect transistor based on graphene–WS 2 heterostructures for flexible and transparent electronics. Nature nanotechnology, 2013. 8(2): p. 100.
15. Tongay, S., et al., Thermally driven crossover from indirect toward direct bandgap in 2D semiconductors: MoSe2 versus MoS2. Nano letters, 2012. 12(11): p. 5576-5580.
16. Dean, C.R., et al., Boron nitride substrates for high-quality graphene electronics. Nature nanotechnology, 2010. 5(10): p. 722.
17. Tongay, S., et al., Defects activated photoluminescence in two-dimensional semiconductors: interplay between bound, charged, and free excitons. Scientific reports, 2013. 3: p. 2657.
18. Chernikov, A., et al., Exciton binding energy and nonhydrogenic Rydberg series in monolayer WS 2. Physical review letters, 2014. 113(7): p. 076802.
19. Stoller, M.D., et al., Graphene-based ultracapacitors. Nano letters, 2008. 8(10): p. 3498-3502.
20. Ozgur, U., D. Hofstetter, and H. Morkoc, ZnO devices and applications: a review of current status and future prospects. Proceedings of the IEEE, 2010. 98(7): p. 1255-1268.

21. Wang, Z.L., Zinc oxide nanostructures: growth, properties and applications. Journal of physics: condensed matter, 2004. 16(25): p. R829.
22. Janotti, A. and C.G. Van de Walle, Fundamentals of zinc oxide as a semiconductor. Reports on progress in physics, 2009. 72(12): p. 126501.
23. Norton, D.P., et al., ZnO: growth, doping & processing. Materials today, 2004. 7(6): p. 34-40.
24. Wang, Z.L. and J. Song, Piezoelectric nanogenerators based on zinc oxide nanowire arrays. Science, 2006. 312(5771): p. 242-246.
25. Pandya, H., S. Chandra, and A. Vyas, Integration of ZnO nanostructures with MEMS for ethanol sensor. Sensors and Actuators B: Chemical, 2012. 161(1): p. 923-928.
26. Reynolds, D., et al., Valence-band ordering in ZnO. Physical Review B, 1999. 60(4): p. 2340.
27. Chen, Y., et al., Plasma assisted molecular beam epitaxy of ZnO on c-plane sapphire: Growth and characterization. Journal of Applied Physics, 1998. 84(7): p. 3912-3918.
28. Kozuka, Y., A. Tsukazaki, and M. Kawasaki, Challenges and opportunities of ZnO-related single crystalline heterostructures. Applied Physics Reviews, 2014. 1(1): p. 011303.
29. Nobis, T., et al., Spatially inhomogeneous impurity distribution in ZnO micropillars. Nano Letters, 2004. 4(5): p. 797-800.
30. Ischenko, V., et al., Zinc oxide nanoparticles with defects. Advanced functional materials, 2005. 15(12): p. 1945-1954.
31. Meulenkamp, E.A., Synthesis and growth of ZnO nanoparticles. The Journal of Physical Chemistry B, 1998. 102(29): p. 5566-5572.

32. Nasiri, N., et al., Ultraporous Electron-Depleted ZnO Nanoparticle Networks for Highly Sensitive Portable Visible-Blind UV Photodetectors. Advanced Materials, 2015. 27(29): p. 4336-4343.

33. Kisi, E.H. and M.M. Elcombe, u parameters for the wurtzite structure of ZnS and ZnO using powder neutron diffraction. Acta Crystallographica Section C: Crystal Structure Communications, 1989. 45(12): p. 1867-1870.

34. McCluskey, M.D. and S. Jokela, Defects in zno. Journal of Applied Physics, 2009. 106(7): p. 10.

35. Meyer, B., et al., Bound exciton and donor–acceptor pair recombinations in ZnO. physica status solidi (b), 2004. 241(2): p. 231-260.

36. Hussain, S., Investigation of structural and optical properties of nanocrystalline ZnO. 2008, Institutionen för fysik, kemi och biologi.

37. Pelant, I. and J. Valenta, Luminescence spectroscopy of semiconductors. 2012: Oxford University Press.

38. Cremades, A., et al., Structural and optical properties of Si-doped GaN. Physical Review B, 2000. 61(4): p. 2812.

39. Meyer, B., et al., Ionized and neutral donor-bound excitons in ZnO. Physical Review B, 2007. 76(18): p. 184120.

40. Schmidt-Mende, L. and J.L. MacManus-Driscoll, ZnO–nanostructures, defects, and devices. Materials today, 2007. 10(5): p. 40-48.

41. Kroger, F., The Chemistry of Imperfect Crystals, 2-nd revised edition, 2. 1974, North-Holland Publishing Company.

42. Maestre, D., A. Cremades, and J. Piqueras, Cathodoluminescence of defects in sintered tin oxide. Journal of applied physics, 2004. 95(6): p. 3027-3030.

43. Parihar, V., M. Raja, and R. Paulose, A brief review of structural, electrical and electrochemical properties of zinc oxide nanoparticles. Reviews on Advanced Materials Science, 2018. 53(2): p. 119-130.

44. Selim, F., et al., Nature of native defects in ZnO. Physical review letters, 2007. 99(8): p. 085502.

45. Look, D.C., et al., Evidence for native-defect donors in n-type ZnO. Physical review letters, 2005. 95(22): p. 225502.

46. Fiedler, S., Enhancement of the UV emission in metal nanoparticle-coated ZnO. 2018.

47. Janotti, A. and C.G. Van de Walle, Native point defects in ZnO. Physical Review B, 2007. 76(16): p. 165202.

48. Han, J., P. Mantas, and A. Senos, Defect chemistry and electrical characteristics of undoped and Mn-doped ZnO. Journal of the European Ceramic Society, 2002. 22(1): p. 49-59.

49. Hagemark, K., Defect structure of Zn-doped ZnO. Journal of Solid State Chemistry, 1976. 16(3-4): p. 293-299.

50. Lin, B., Z. Fu, and Y. Jia, Green luminescent center in undoped zinc oxide films deposited on silicon substrates. Applied Physics Letters, 2001. 79(7): p. 943-945.

51. Van de Walle, C.G. and J. Neugebauer, Universal alignment of hydrogen levels in semiconductors, insulators and solutions. Nature, 2003. 423(6940): p. 626.

52. Nahm, H.-H., C. Park, and Y.-S. Kim, Bistability of hydrogen in ZnO: Origin of doping limit and persistent photoconductivity. Scientific reports, 2014. 4: p. 4124.

53. Wardle, M., J. Goss, and P. Briddon, First-principles study of the diffusion of hydrogen in ZnO. Physical review letters, 2006. 96(20): p. 205504.

54. Van de Walle, C.G., Hydrogen as a cause of doping in zinc oxide. Physical review letters, 2000. 85(5): p. 1012.

55. Ohashi, N., et al., Passivation of active recombination centers in ZnO by hydrogen doping. Journal of applied physics, 2003. 93(10): p. 6386-6392.

56. Ohashi, N., et al., Effect of hydrogen doping on ultraviolet emission spectra of various types of ZnO. Applied physics letters, 2002. 80(16): p. 2869-2871.

57. Ip, K., et al., Hydrogen incorporation and diffusivity in plasma-exposed bulk ZnO. Applied physics letters, 2003. 82(3): p. 385-387.

58. Rodrigues, J., et al., Effect of N 2 and H 2 plasma treatments on band edge emission of ZnO microrods. Scientific reports, 2015. 5: p. 10783.

59. Jokela, S.J., Stability and structure of hydrogen defects in zinc oxide. Vol. 68. 2006.

60. Jokela, S. and M. McCluskey, Structure and stability of O− H donors in ZnO from high-pressure and infrared spectroscopy. Physical Review B, 2005. 72(11): p. 113201.

61. Tsukazaki, A., et al., Repeated temperature modulation epitaxy for p-type doping and light-emitting diode based on ZnO. Nature materials, 2005. 4(1): p. 42.

62. Oh, M.-S., et al., Type conversion of intentionally undoped ZnO layers grown by pulsed laser deposition. Superlattices and microstructures, 2006. 39(1-4): p. 130-137.

63. Guziewicz, E., et al., Abundant acceptor emission from nitrogen-doped ZnO films prepared by atomic layer deposition under oxygen-rich conditions. ACS applied materials & interfaces, 2017. 9(31): p. 26143-26150.

64. Fons, P., et al., Direct observation of nitrogen location in molecular beam epitaxy grown nitrogen-doped ZnO. Physical Review Letters, 2006. 96(4): p. 045504.

65. Xiong, G., et al., Donor-acceptor pair luminescence of nitrogen-implanted ZnO single crystal. Journal of Applied Physics, 2005. 97(4): p. 043528.
66. Ton-That, C., et al., Molecular nitrogen acceptors in ZnO nanowires induced by nitrogen plasma annealing. Physical Review B, 2015. 92(2): p. 024103.
67. Wei, S.-H. and J. Li, Design of Shallow P-type Dopants in ZnO (Presentation). 2008, National Renewable Energy Lab.(NREL), Golden, CO (United States).
68. Wei, S.-H., Overcoming the doping bottleneck in semiconductors. Computational Materials Science, 2004. 30(3-4): p. 337-348.
69. Park, C., S. Zhang, and S.-H. Wei, Origin of p-type doping difficulty in ZnO: The impurity perspective. Physical Review B, 2002. 66(7): p. 073202.
70. Yan, Y., S. Zhang, and S. Pantelides, Control of doping by impurity chemical potentials: Predictions for p-type ZnO. Physical Review Letters, 2001. 86(25): p. 5723.
71. Morkoç, H. and Ü. Özgür, Zinc oxide: fundamentals, materials and device technology. 2008: John Wiley & Sons.
72. Janotti, A. and C.G. Van de Walle, Absolute deformation potentials and band alignment of wurtzite ZnO, MgO, and CdO. Physical Review B, 2007. 75(12): p. 121201.
73. Lorenz, M., et al., The 2016 oxide electronic materials and oxide interfaces roadmap. Journal of Physics D: Applied Physics, 2016. 49(43): p. 433001.
74. Thapa, D., et al., UV-luminescent MgZnO semiconductor alloys: nanostructure and optical properties. Journal of Materials Science: Materials in Electronics, 2017. 28(3): p. 2511-2520.
75. Ohtomo, A., et al., Mg x Zn 1− x O as a II–VI widegap semiconductor alloy. Applied Physics Letters, 1998. 72(19): p. 2466-2468.

76. Bowen, W.E., Thin Film Electronics Based on ZnO and ZnO/MgZnO Heterojunctions. 2010.

77. Sarver, J., F.L. Katnack, and F. Hummel, Phase Equilibria and Manganese-Activated Fluorescence in the System Zn3 (PO 4) 2-Mg3 (PO 4) 2. Journal of The Electrochemical Society, 1959. 106(11): p. 960-963.

78. Takeuchi, I., et al., Monolithic multichannel ultraviolet detector arrays and continuous phase evolution in Mg x Zn 1− x O composition spreads. Journal of Applied Physics, 2003. 94(11): p. 7336-7340.

79. Alferov, Z.I., Nobel Lecture: The double heterostructure concept and its applications in physics, electronics, and technology. Reviews of modern physics, 2001. 73(3): p. 767.

80. Fu, L., et al., Disordering of quantum structures for optoelectronic device integration, in Comprehensive Semiconductor Science and Technology. 2011, Academic Press. p. 584-625.

81. Falson, J. and M. Kawasaki, A review of the quantum Hall effects in MgZnO/ZnO heterostructures. Reports on Progress in Physics, 2018. 81(5): p. 056501.

82. Nakahara, K., et al., Nitrogen doped Mg x Zn 1− x O/ZnO single heterostructure ultraviolet light-emitting diodes on ZnO substrates. Applied Physics Letters, 2010. 97(1): p. 013501.

83. Koike, K., et al., Piezoelectric carrier confinement by lattice mismatch at ZnO/Zn0. 6Mg0. 4O heterointerface. Japanese journal of applied physics, 2004. 43(10B): p. L1372.

84. Choi, S., et al., Radiative recombination of confined electrons at the MgZnO/ZnO heterojunction interface. Scientific reports, 2017. 7(1): p. 7457.

85. Wang, B.-S., Y.-S. Li, and I.-C. Cheng, Mobility enhancement in RF-sputtered MgZnO/ZnO heterostructure thin-film transistors. IEEE Transactions on Electron Devices, 2016. 63(4): p. 1545-1549.

86. Frensley, W.R., VLSI Electronics: Microstructure Science.(Academic Press, San Diego) Publication date: March 25, 1994. 1998.

87. 汤琨, et al., High-quality ZnO growth, doping, and polarization effect. 半导体学报: 英文版, 2016(3): p. 1-13.

88. Falson, J., et al., MgZnO/ZnO heterostructures with electron mobility exceeding 1× 10 6 cm 2/Vs. Scientific reports, 2016. 6: p. 26598.

89. Maryenko, D., et al., Observation of anomalous Hall effect in a non-magnetic two-dimensional electron system. Nature communications, 2017. 8: p. 14777.

90. Betancourt, J., et al., Polarization discontinuity induced two-dimensional electron gas at ZnO/Zn (Mg) O interfaces: A first-principles study. Physical Review B, 2013. 88(8): p. 085418.

91. Hao, Y., J.F. Zhang, and J.C. Zhang, Nitride Wide Bandgap Semiconductor Material and Electronic Devices. 2016: CRC Press.

92. Meyer, B. and D. Marx, Density-functional study of the structure and stability of ZnO surfaces. Physical Review B, 2003. 67(3): p. 035403.

93. Tan, C., et al., Recent advances in ultrathin two-dimensional nanomaterials. Chemical reviews, 2017. 117(9): p. 6225-6331.

94. Dral, A.P. and E. Johan, 2D metal oxide nanoflakes for sensing applications: Review and perspective. Sensors and Actuators B: Chemical, 2018. 272: p. 369-392.

95. Geim, A.K. and K.S. Novoselov, The rise of graphene, in Nanoscience and Technology: A Collection of Reviews from Nature Journals. 2010, World Scientific. p. 11-19.

96. Zhang, H., Ultrathin two-dimensional nanomaterials. ACS nano, 2015. 9(10): p. 9451-9469.

97. Novoselov, K.S., et al., Electric field effect in atomically thin carbon films. science, 2004. 306(5696): p. 666-669.

98. Li, L.H. and Y. Chen, Atomically thin boron nitride: unique properties and applications. Advanced Functional Materials, 2016. 26(16): p. 2594-2608.

99. Lv, R., et al., Transition metal dichalcogenides and beyond: synthesis, properties, and applications of single-and few-layer nanosheets. Accounts of chemical research, 2014. 48(1): p. 56-64.

100. Jian, D., et al., Electron hopping transport in 2D zinc oxide nanoflakes. 2D Materials, 2017. 4(2): p. 025028.

101. Kolmakov, A. and M. Moskovits, Chemical sensing and catalysis by one-dimensional metal-oxide nanostructures. Annu. Rev. Mater. Res., 2004. 34: p. 151-180.

102. Zhai, T., et al., A comprehensive review of one-dimensional metal-oxide nanostructure photodetectors. Sensors, 2009. 9(8): p. 6504-6529.

103. Feng, Z.C., Handbook of zinc oxide and related materials: volume two, devices and nano-engineering. Vol. 2. 2012: CRC press.

104. Sturm, C., et al., Dielectric tensor of monoclinic Ga2O3 single crystals in the spectral range 0.5–8.5 eV. APL Materials, 2015. 3(10): p. 106106.

105. Kranert, C., et al., Lattice parameters and Raman-active phonon modes of β-(Al x Ga1− x) 2O3. Journal of Applied Physics, 2015. 117(12): p. 125703.

106. Djurišić, A., A.M.C. Ng, and X. Chen, ZnO nanostructures for optoelectronics: Material properties and device applications. Progress in quantum electronics, 2010. 34(4): p. 191-259.

107. Park, J.-H., et al., Ultrawide ZnO nanosheets. Journal of Materials Chemistry, 2004. 14(1): p. 35-36.

108. Wang, Z.L., Nanostructures of zinc oxide. Materials today, 2004. 7(6): p. 26-33.

109. Freeman, C.L., et al., Graphitic nanofilms as precursors to wurtzite films: theory. Physical review letters, 2006. 96(6): p. 066102.

110. Si, H., et al., Theoretical prediction of hydrogen storage on ZnO sheet. The Journal of Physical Chemistry C, 2011. 115(18): p. 9053-9058.

111. Rao, G., et al., Adsorption mechanism of graphene-like ZnO monolayer towards CO2 molecules: enhanced CO2 capture. Nanotechnology, 2015. 27(1): p. 015502.

112. Chen, K., et al., Selective patterned growth of ZnO nanowires/nanosheets and their photoluminescence properties. Optical Materials Express, 2015. 5(2): p. 353-360.

113. Tom, K.B., et al., Solution-Based, Template-Assisted Realization of Large-Scale Graphitic ZnO. ACS nano, 2018. 12(8): p. 7554-7561.

114. Li, Y.-L., Z. Fan, and J.-C. Zheng, Enhanced thermoelectric performance in graphitic ZnO (0001) nanofilms. Journal of Applied Physics, 2013. 113(8): p. 083705.

115. Ren, J., H. Zhang, and X. Cheng, Electronic and magnetic properties of all 3d transition-metal-doped ZnO monolayers. International Journal of Quantum Chemistry, 2013. 113(19): p. 2243-2250.

116. Ma, D., et al., CO catalytic oxidation on Al-doped graphene-like ZnO monolayer sheets: a first-principles study. Journal of Materials Chemistry C, 2015. 3(38): p. 9964-9972.

117. Mai, W. Fundamental theory of atomic force microscopy. 2010; Available from: http://www.nanoscience.gatech.edu/zlwang/research/afm.html.

118. Microscopemaster. The atomic force microscope (AFM). 2019; Available from: https://www.microscopemaster.com/atomic-force-microscope.html.

119. Hieulle, J., Structures and Electronic Properties of Organic Self-Assembled Monolayers Characterized by STM and XPS. 2014.

120. Zhu, L., Doping and characterisation of ZnO nanowires and crystals. 2015.

121. Glasgow, U.o. Scanning Electron Microscopy (SEM). Available from: https://www.gla.ac.uk/schools/ges/research/researchfacilities/isaac/services/scanningelectronmicroscopy/.

122. B.G. Yacobi, D.B.H., Cathodoluminescence microscopy of inorganic solids. 2013: Springer Science & Business Media.

123. Kramida, A., Y. Ralchenko, and J. Reader, NIST atomic spectra database (ver. 5.3). 2015.

124. Drouin, D., et al., CASINO V2. 42—a fast and easy-to-use modeling tool for scanning electron microscopy and microanalysis users. Scanning: The Journal of Scanning Microscopies, 2007. 29(3): p. 92-101.

125. Grün, A., Lumineszenz-photometrische messungen der energieabsorption im strahlungsfeld von elektronenquellen eindimensionaler fall in luft. Zeitschrift für Naturforschung A, 1957. 12(2): p. 89-95.

126. Phillips, M.R., et al., Cathodoluminescence efficiency dependence on excitation density in n-type gallium nitride. Microscopy and Microanalysis, 2003. 9(2): p. 144-151.

127. Rogers, D.J., et al., Investigations of ZnO thin films grown on c-Al2O3 by pulsed laser deposition in N2+ O2 ambient. physica status solidi c, 2008. 5(9): p. 3084-3087.

128. Rogers, D.J., et al. ZnO thin film templates for GaN-based devices. in Quantum Sensing and Nanophotonic Devices II. 2005. International Society for Optics and Photonics.

129. Kang, J.-W., et al., Radial multi-quantum well ZnO nanorod arrays for nanoscale ultraviolet light-emitting diodes. Nanoscale, 2018. 10(31): p. 14812-14818.

130. Sidiropoulos, T.P., et al., Ultrafast plasmonic nanowire lasers near the surface plasmon frequency. Nature Physics, 2014. 10(11): p. 870.

131. Sun, Z., et al., Graphene activating room-temperature ferromagnetic exchange in cobalt-doped ZnO dilute magnetic semiconductor quantum dots. ACS nano, 2014. 8(10): p. 10589-10596.

132. Morhain, C., et al., Internal electric field in wurtzite Zn O∕ Zn 0.78 Mg 0.22 O quantum wells. Physical Review B, 2005. 72(24): p. 241305.

133. Chauveau, J.-M., et al., Benefits of homoepitaxy on the properties of nonpolar (Zn, Mg) O/ZnO quantum wells on a-plane ZnO substrates. Applied Physics Letters, 2010. 97(8): p. 081903.

134. Wu, X., et al., Structural origin of V-defects and correlation with localized excitonic centers in InGaN/GaN multiple quantum wells. Applied Physics Letters, 1998. 72(6): p. 692-694.

135. Lord, S., et al., Hydrogen passivation of nonradiative defects in InGaAs/Al x Ga1− x As quantum wells. Journal of applied physics, 1993. 73(2): p. 740-748.

136. Chang, M.-H., et al., Light emitting diodes reliability review. Microelectronics Reliability, 2012. 52(5): p. 762-782.

137. Cremades, A., et al., Inhomogeneous incorporation of In and Al in molecular beam epitaxial AlInGaN films. Journal of Applied Physics, 2001. 90(9): p. 4868-4870.

138. Thompson, A., et al., Thermal stability of Cd Zn O∕ Zn O multi-quantum-wells. Applied Physics Letters, 2007. 91(20): p. 201921.

139. Buyanova, I., et al., Effects of hydrogen on the optical properties of Zn Cd O∕ Zn O quantum wells grown by molecular beam epitaxy. Applied Physics Letters, 2008. 92(26): p. 261912.

140. Ton-That, C., L. Weston, and M. Phillips, Characteristics of point defects in the green luminescence from Zn-and O-rich ZnO. Physical Review B, 2012. 86(11): p. 115205.

141. Ren, P., et al., A novel usage of hydrogen treatment to improve the indium incorporation and internal quantum efficiency of green InGaN/GaN multiple quantum wells simultaneously. Journal of Physics D: Applied Physics, 2016. 49(17): p. 175101.

142. Lin, C.-C., et al., Enhanced luminescent and electrical properties of hydrogen-plasma ZnO nanorods grown on wafer-scale flexible substrates. Applied Physics Letters, 2005. 86(18): p. 183103.

143. Dev, A., et al., Stable enhancement of near-band-edge emission of ZnO nanowires by hydrogen incorporation. Nanotechnology, 2010. 21(6): p. 065709.

144. Lem, L.L., C. Ton-That, and M.R. Phillips, Distribution of visible luminescence centers in hydrogen-doped ZnO. Journal of Materials Research, 2011. 26(23): p. 2912-2915.

145. Lavrov, E., et al., Hydrogen-related defects in ZnO studied by infrared absorption spectroscopy. Physical Review B, 2002. 66(16): p. 165205.

146. Ashrafi, A., Exciton localization in inhomogeneously broadened ZnO/Mg x Zn 1− x O quantum wells. Journal of Applied Physics, 2010. 107(12): p. 123527.

147. Chen, H., et al., Optical properties of one-and two-dimensional excitons in m-plane ZnO/MgZnO multiple quantum wells. Journal of Physics D: Applied Physics, 2016. 49(9): p. 095105.

148. Makino, T., et al., Room-temperature luminescence of excitons in ZnO/(Mg, Zn) O multiple quantum wells on lattice-matched substrates. Applied Physics Letters, 2000. 77(7): p. 975-977.

149. Urgessa, Z., et al., Low temperature near band edge recombination dynamics in ZnO nanorods. Journal of Applied Physics, 2014. 116(12): p. 123506.

150. Jacob, A., et al., Hydrogen passivation of self assembled InAs quantum dots. Journal of applied physics, 2002. 92(11): p. 6794-6798.

151. Ton-That, C. and M. Phillips, Cathodoluminescence microanalysis of ZnO nanowires, in Semiconductor Nanowires. 2015, Elsevier. p. 393-407.

152. Rudin, S., T. Reinecke, and B. Segall, Temperature-dependent exciton linewidths in semiconductors. Physical Review B, 1990. 42(17): p. 11218.

153. Makino, T., et al., Optical properties of excitons in ZnO-based quantum well heterostructures. Semiconductor science and technology, 2005. 20(4): p. S78.

154. Sun, H., et al., Temperature dependence of excitonic absorption spectra in ZnO/Zn 0.88 Mg 0.12 O multiquantum wells grown on lattice-matched substrates. Applied Physics Letters, 2001. 78(17): p. 2464-2466.

155. Davis, J.A. and C. Jagadish, Ultrafast spectroscopy of ZnO/ZnMgO quantum wells. Laser & Photonics Reviews, 2009. 3(1-2): p. 85-96.

156. Drouin, D., P. Hovington, and R. Gauvin, CASINO: A new monte carlo code in C language for electron beam interactions—part II: Tabulated values of the mott cross section. Scanning, 1997. 19(1): p. 20-28.

157. Moon, Y.-T., et al., Effects of thermal and hydrogen treatment on indium segregation in InGaN/GaN multiple quantum wells. Journal of Applied Physics, 2001. 89(11): p. 6514-6518.

158. Lorenz, M., et al., The 2016 oxide electronic materials and oxide interfaces roadmap. J. Phys. D Appl. Phys., 2016. 49(43).

159. Wang, R.C., Y.X. Lin, and J.J. Wu, Intrinsic n- and p-Type MgZnO Nanorods for Deep-UV Detection and Room-Temperature Gas Sensing. Journal of Physical Chemistry C, 2015. 119(52): p. 29186-29192.

160. Heo, Y.W., et al., p-type behavior in phosphorus-doped (Zn,Mg)O device structures. Applied Physics Letters, 2004. 84(18): p. 3474-3476.

161. Wei, Z., et al., Formation of p-type MgZnO by nitrogen doping. Applied Physics Letters, 2006. 89(10): p. 102104.

162. Li, J., et al., Design of shallow acceptors in ZnO: First-principles band-structure calculations. Physical Review B, 2006. 74(8): p. 081201.

163. Gao, L.L., et al., Effects of Mg concentration on solubility and chemical state of N in N-doped MgZnO alloy. Journal of Chemical Physics, 2010. 133(20).

164. Kurtz, A., et al., Acceptor levels in ZnMgO:N probed by deep level optical spectroscopy. Applied Physics Letters, 2014. 104(8).

165. Shan, C.X., et al., p-type doping of MgZnO films and their applications in optoelectronic devices. Optics Letters, 2015. 40(13): p. 3041-3044.

166. Trunk, M., et al., Deep level related photoluminescence in ZnMgO. Applied Physics Letters, 2010. 97(21).

167. Li, Y.F., et al., Realization of p-type conduction in undoped MgxZn1-xO thin films by controlling Mg content. Applied Physics Letters, 2007. 91(23).

168. Wight, G.R. and C.E. Brion, K-shell excitations in NO and O2 by 2.5 keV electron impact. Journal of Electron Spectroscopy and Related Phenomena, 1974. 4(4): p. 313-325.

169. Ruck, B.J., et al., Quantitative study of molecular N_2 trapped in disordered GaN:O films. Physical Review B, 2004. 70(23): p. 235202.

170. Bozanic, A., et al., Characterization of molecular nitrogen in III-V compound semiconductors by near-edge x-ray absorption fine structure and photoemission spectroscopies. Journal of Vacuum Science & Technology A, 2008. 26(4): p. 592-596.

171. Zou, C., et al., Study of a nitrogen-doped ZnO film with synchrotron radiation. Applied Physics Letters, 2009. 94(17): p. 171903.

172. Chen, J.G., NEXAFS investigations of transition metal oxides, nitrides, carbides, sulfides and other interstitial compounds. Surface Science Reports, 1997. 30(1-3): p. 1-152.

173. You, Z. and G. Hua, Electrical, optical and microstructural properties of transparent conducting GZO thin films deposited by magnetron sputtering. Journal of Alloys and Compounds, 2012. 530: p. 11-17.

174. Wagner, M.R., et al., Bound excitons in ZnO: Structural defect complexes versus shallow impurity centers. Physical Review B, 2011. 84(3).

175. Ursaki, V., et al., Multiphonon resonant Raman scattering in ZnO crystals and nanostructured layers. Physical Review B, 2004. 70(15): p. 155204.

176. Ye, J., et al., Effects of alloying and localized electronic states on the resonant Raman spectra of Zn 1− x Mg x O nanocrystals. Applied Physics Letters, 2007. 91(9): p. 091901.

177. Saha, S., et al., Effect of annealing temperature on optical and electrical properties of nitrogen implanted p-type ZnMgO thin films. Journal of Materials Science: Materials in Electronics, 2015. 26(12): p. 9759-9765.

178. Lautenschlaeger, S., et al., Optical signatures of nitrogen acceptors in ZnO. Physical Review B, 2012. 85(23): p. 235204.

179. Ohtomo, A., et al., Structure and optical properties of ZnO/Mg0.2Zn0.8O superlattices. Applied Physics Letters, 1999. 75(7): p. 980-982.

180. Han, B., M.P. Ulmer, and B.W. Wessels, Investigation of deep-level luminescence in In0.07Ga0.93N : Mg. Physica B-Condensed Matter, 2003. 340: p. 470-474.

181. Reshchikov, M.A. and H. Morkoc, Luminescence properties of defects in GaN. Journal of Applied Physics, 2005. 97(6).

182. Ton-That, C., L. Weston, and M.R. Phillips, Characteristics of point defects in the green luminescence from Zn- and O-rich ZnO. Physical Review B, 2012. 86(11).

183. Lyons, J.L., A. Janotti, and C.G. Van de Walle, Why nitrogen cannot lead to p-type conductivity in ZnO. Applied Physics Letters, 2009. 95(25).

184. Liu, L., et al., p-Type Conductivity in N-Doped ZnO: The Role of the N-Zn-V-O Complex. Physical review letters, 2012. 108(21): p. 215501.

185. Lambrecht, W.R.L. and A. Boonchun, Identification of a N-related shallow acceptor and electron paramagnetic resonance center in ZnO: N_2^+ on the Zn site. Physical Review B, 2013. 87(19): p. 195207.

186. Chernikov, A., et al., Exciton Binding Energy and Nonhydrogenic Rydberg Series in Monolayer WS2. Physical Review Letters, 2014. 113(7).

187. Georgiou, T., et al., Vertical field-effect transistor based on graphene-WS2 heterostructures for flexible and transparent electronics. Nature Nanotechnology, 2013. 8(2): p. 100-103.

188. Dean, C.R., et al., Boron nitride substrates for high-quality graphene electronics. Nature Nanotechnology, 2010. 5(10): p. 722-726.

189. Tongay, S., et al., Defects activated photoluminescence in two-dimensional semiconductors: interplay between bound, charged, and free excitons. Scientific Reports, 2013. 3.

190. Ma, R.Z. and T. Sasaki, Nanosheets of Oxides and Hydroxides: Ultimate 2D Charge-Bearing Functional Crystallites. Advanced Materials, 2010. 22(45): p. 5082-5104.

191. Tongay, S., et al., Thermally Driven Crossover from Indirect toward Direct Bandgap in 2D Semiconductors: MoSe2 versus MoS2. Nano Letters, 2012. 12(11): p. 5576-5580.

192. Benson, O., Assembly of hybrid photonic architectures from nanophotonic constituents. Nature, 2011. 480(7376): p. 193-199.

193. Chichibu, S.F., et al., Exciton-polariton spectra and limiting factors for the room-temperature photoluminescence efficiency in ZnO. Semiconductor Science and Technology, 2005. 20(4): p. S67-S77.

194. Cusco, R., et al., Temperature dependence of raman scattering in ZnO. Physical Review B, 2007. 75(16).

195. Zhang, D.F., L.D. Sun, and C.H. Yan, Optical properties of ZnO nanoplatelets and rectangular cross-sectioned nanowires. Chemical Physics Letters, 2006. 422(1-3): p. 46-50.

196. Singh, M., et al., Soft exfoliation of 2D SnO with size-dependent optical properties. 2d Materials, 2017. 4(2): p. 025110.

197. Backes, C., et al., Edge and confinement effects allow in situ measurement of size and thickness of liquid-exfoliated nanosheets. Nature communications, 2014. 5(1): p. 1-10.

198. Yadgarov, L., et al., Dependence of the absorption and optical surface plasmon scattering of MoS2 nanoparticles on aspect ratio, size, and media. ACS nano, 2014. 8(4): p. 3575-3583.

199. Harvey, A., et al., Non-resonant light scattering in dispersions of 2D nanosheets. Nature communications, 2018. 9(1): p. 1-11.

200. Ton-That, C., L. Weston, and M.R. Phillips, Characteristics of point defects in the green luminescence from Zn- and O-rich ZnO. Phys. Rev. B, 2012. 86: p. 115205.

201. Sun, X.W., et al., A ZnO nanorod inorganic/organic heterostructure light-emitting diode emitting at 342 nm. Nano Lett., 2008. 8: p. 1219.

202. Lambrecht, W.R.L., et al., Valence-band ordering and magneto-optic exciton fine structure in ZnO. Physical Review B, 2002. 65(7): p. 12.

203. Wang, L. and N. Giles, Temperature dependence of the free-exciton transition energy in zinc oxide by photoluminescence excitation spectroscopy. Journal of Applied Physics, 2003. 94(2): p. 973-978.

204. Wang, L.J. and N.C. Giles, Determination of the ionization energy of nitrogen acceptors in zinc oxide using photoluminescence spectroscopy. Applied Physics Letters, 2004. 84(16): p. 3049-3051.

205. Cho, Y.H., et al., Depth-resolved optical studies of excitonic and phonon-assisted transitions in ZnO epilayers. Applied Physics Letters, 2006. 89(20): p. 3.

206. Yan, B., et al., Localized suppression of longitudinal-optical-phonon-exciton coupling in bent ZnO nanowires. Nanotechnology, 2010. 21(44): p. 6.

207. Wang, L.J. and N.C. Giles, Temperature dependence of the free-exciton transition energy in zinc oxide by photoluminescence excitation spectroscopy. Journal of Applied Physics, 2003. 94(2): p. 973-978.

208. Zhu, L.C., et al., Indirect excitons in hydrogen-doped ZnO. Journal of Physics D-Applied Physics, 2017. 50(11): p. 6.

209. Giles, N.C., et al., Effects of phonon coupling and free carriers on band-edge emission at room temperature in n-type ZnO crystals. Applied Physics Letters, 2006. 89(25): p. 3.

210. Meyer, B., et al., Bound exciton and donor–acceptor pair recombinations in ZnO. Phys. Status Solidi (b), 2004. 241: p. 231.